

The GLUEX Beamline and Detector

2 S. Adhikari^w, A. Ali^{j,1}, M. Amaryan^w, E.G. Anassontzis^b, A. Austregesilo^c,
 3 F. Barbosaⁿ, J. Barlow^g, A. Barnes^c, E. Barriga^g, R. Barsotti^k, T.D. Beattie^x,
 4 V.V. Berdnikov^{d,r}, G. Biallasⁿ, T. Black^u, W. Boeglin^f, P. Brindza^{n,w},
 5 W.J. Briscoe^h, T. Brittonⁿ, J. Brockⁿ, W.K. Brooks^y, B.E. Cannon^g,
 6 C. Carlinⁿ, D.S. Carmanⁿ, T. Carstens^{n,2}, N. Cao^l, O. Chernyshov^m,
 7 E. Chudakovⁿ, S. Cole^a, O. Cortes^h, W.D. Crahenⁿ, V. Crede^g, M.M. Daltonⁿ,
 8 T. Daniels^u, A. Deurⁿ, C. Dickoverⁿ, S. Dobbs^g, A. Dolgolenko^m, R. Dotel^f,
 9 M. Dugger^a, R. Dzhygadlo^j, A. Dzierba^k, H. Egiyanⁿ, T. Erboraf^f, A. Ernst^g,
 10 P. Eugenio^g, C. Fanelli^q, S. Fegan^{h,3}, A.M. Foda^x, J. Foote^k, J. Frye^k,
 11 S. Furlotovⁿ, L. Gan^u, A. Gasparian^t, A. Gerasimov^m, N. Gevorgyan^{ab},
 12 C. Gleason^k, K. Goetzen^j, A. Goncalves^g, V.S. Goryachev^m, L. Guo^f,
 13 H. Hakobyan^y, A. Hamdi^{j,1}, J. Hardin^q, C.L. Henschel^{x,4}, G.M. Huber^x,
 14 C. Huttonⁿ, A. Hurley^{ac}, D.G. Irelandⁱ, M.M. Itoⁿ, N.S. Jarvis^c, R.T. Jones^e,
 15 V. Kakoyan^{ab}, S. Katsaganis^{x,5}, G. Kalicy^d, M. Kamel^f, C.D. Keithⁿ,
 16 F.J. Klein^{d,6}, R. Kliemt^j, D. Kolybaba^x, C. Kourkoumelis^b, S.T. Krueger^{x,7},
 17 S. Kuleshov^y, I. Larin^{p,m}, D. Lawrenceⁿ, J.P. Leckey^k, D.I. Lersch^g,
 18 B.D. Leverington^{x,8}, W.I. Levine^c, W. Li^{ac}, B. Liu^l, K. Livingstonⁱ,
 19 G.J. Lolos^x, V. Lyubovitskij^{z,aa}, D. Mackⁿ, H. Marukyan^{ab}, P.T. Mattione^{n,9},
 20 V. Matveev^m, M. McCaughanⁿ, M. McCracken^c, W. McGinley^c, J. McIntyre^e,

*Corresponding author: Tel.: +1 757 269 7625.

Email address: elton@jlab.org (E.S. Smith)

¹Also at Goethe University Frankfurt, 60323 Frankfurt am Main, Germany.

²Current address: 103 Riverside Dr, Yorktown, VA 23692.

³Current address: University of York, York YO10 5DD, United Kingdom.

⁴Current address: Department of Physics and Astronomy, University of Calgary, Calgary, AB, T2N 1N4, Canada.

⁵Current address: Department of Physics, University of Regina, Regina, SK, S4S 0A2, Canada.

⁶Current address: Office of Academic Computing Services, University of Maryland, College Park, MD 20742.

⁷Current address: iQMetrix, 311 Portage Avenue, Winnipeg, MB, R3B 2B9, Canada.

⁸Current address: Heidelberg Universitaet, Physikalisches Institut 3.406, 69120 Heidelberg, Germany.

⁹Current address: Deep Silver Volition, 1 E Main St., Champaign, IL 61820.

¹⁰Current address: Oak Ridge National Laboratory, Oak Ridge, TN 37831.

¹¹Current address: Toshiba Medical Research Institute USA, Inc., 706 N Deerpath Dr, Vernon Hills, IL 60061.

¹²Current address: 660 E Raven way, Gilbert, AZ 85297.

¹³Current address: Brookhaven National Laboratory, Upton, New York 11973.

¹⁴Current address: Tykans Group Inc., 3412 25 St. NE, Calgary, AB, T1Y 6C1.

¹⁵Current address: Argonne National Laboratory, Argonne, Illinois 60439.

¹⁶Current address: Commonwealth Scientific and Industrial Research Organisation, Lucas Heights, NSW 2234, Australia.

¹⁷Current address: AbbVie Deutschland GmbH, Knollstrasse 67061, Ludwigshafen, Germany.

¹⁸Current address: University of York, York YO10 5DD, United Kingdom.

¹⁹Current address: 2808 Linden Ln, Williamsburg, VA 23185.

21 D. Meekinsⁿ, R. Mendez^y, C.A. Meyer^c, R. Miskimen^p, R.E. Mitchell^k,
 22 F. Mokaya^e, K. Moriya^a, F. Nerling^{j,1}, L. Ng^g, H. Ni^h, A.I. Ostrovidov^g,
 23 Z. Papandreou^x, M. Patsyuk^q, C. Paudel^f, P. Pauliⁱ, R. Pedroni^t,
 24 L. Pentchevⁿ, K.J. Peters^{j,1}, W. Phelps^h, J. Pierce^{n,10}, E. Pooserⁿ, B. Pratt^e,
 25 Y. Qiang^{n,11}, N. Qin^v, V. Razmyslovich^{n,12}, J. Reinhold^f, B.G. Ritchie^a,
 26 J. Ritman^o, L. Robison^v, D. Romanov^r, C. Romero^y, C. Salgado^s,
 27 N. Sandovalⁿ, A.M. Schertz^{ac}, S. Schadmand^o, R.A. Schumacher^c,
 28 C. Schwarz^j, J. Schwiening^j, A.Yu. Semenov^x, I.A. Semenova^x, K.K. Seth^v,
 29 X. Shen^l, M.R. Shepherd^k, E.S. Smith^{n,*}, D.I. Sober^d, A. Somovⁿ, S. Somov^r,
 30 O. Soto^y, N. Sparks^a, M.J. Staib^c, C. Stanislavⁿ, J.R. Stevens^{ac},
 31 J. Stewart^{n,13}, I.I. Strakovsky^h, B.C.L. Summner^a, K. Suresh^x, V.V. Tarasov^m,
 32 S. Taylorⁿ, L.A. Teigrob^{x,14}, A. Teymurazyan^x, A. Thiel^l, I. Tolstukhin^{r,15},
 33 A. Tomaradze^v, A. Toro^y, A. Tsaris^g, Y. Van Haarlem^{c,16}, G. Vasileiadis^b,
 34 I. Vega^y, G. Visser^k, G. Voulgaris^b, N.K. Walford^{d,17}, D. Werthmüller^{i,18},
 35 T. Whitlatchⁿ, N. Wickramaarachchi^w, M. Williams^q, E. Wolin^{n,19}, T. Xiao^v,
 36 Y. Yang^q, J. Zarling^x, Z. Zhang^{ad}, Q. Zhou^l, X. Zhou^{ad}, B. Zihlmannⁿ

37 ^aArizona State University, Tempe, Arizona 85287, USA

38 ^bNational and Kapodistrian University of Athens, 15771 Athens, Greece

39 ^cCarnegie Mellon University, Pittsburgh, Pennsylvania 15213, USA

40 ^dCatholic University of America, Washington, D.C. 20064, USA

41 ^eUniversity of Connecticut, Storrs, Connecticut 06269, USA

42 ^fFlorida International University, Miami, Florida 33199, USA

43 ^gFlorida State University, Tallahassee, Florida 32306, USA

44 ^hThe George Washington University, Washington, D.C. 20052, USA

45 ⁱUniversity of Glasgow, Glasgow G12 8QQ, United Kingdom

46 ^jGSI Helmholtzzentrum für Schwerionenforschung GmbH, D-64291 Darmstadt, Germany

47 ^kIndiana University, Bloomington, Indiana 47405, USA

48 ^lInstitute of High Energy Physics, Beijing 100049, People's Republic of China

49 ^mAlikhanov Institute for Theoretical and Experimental Physics NRC (Kurchatov Institute),
 50 Moscow, 117218, Russia

51 ⁿThomas Jefferson National Accelerator Facility, Newport News, Virginia 23606, USA

52 ^oForschungszentrum Juelich

53 ^pUniversity of Massachusetts, Amherst, Massachusetts 01003, USA

54 ^qMassachusetts Institute of Technology, Cambridge, Massachusetts 02139, USA

55 ^rNational Research Nuclear University Moscow Engineering Physics Institute, Moscow
 56 115409, Russia

57 ^sNorfolk State University, Norfolk, Virginia 23504, USA

58 ^tNorth Carolina A&T State University, Greensboro, North Carolina 27411, USA

59 ^uUniversity of North Carolina at Wilmington, Wilmington, North Carolina 28403, USA

60 ^vNorthwestern University, Evanston, Illinois 60208, USA

61 ^wOld Dominion University, Norfolk, Virginia 23529, USA

62 ^xUniversity of Regina, Regina, Saskatchewan, Canada S4S 0A2

63 ^yUniversidad Técnica Federico Santa María, Casilla 110-V Valparaíso, Chile

64 ^zTomsk State University, 634050 Tomsk, Russia

65 ^{aa}Tomsk Polytechnic University, 634050 Tomsk, Russia

66 ^{ab}A. I. Alikhanian National Science Laboratory (Yerevan Physics Institute), 0036 Yerevan,
 67 Armenia

68 ^{ac}College of William and Mary, Williamsburg, Virginia 23185, USA

69 ^{ad}Wuhan University, Wuhan, Hubei 430072, People's Republic of China

70 **Abstract**

The GLUEX experiment at Jefferson Lab has been designed to study photo-production reactions with a 9-GeV linearly polarized photon beam. The energy and arrival time of beam photons are tagged using a scintillator hodoscope and a scintillating fiber array. The photon flux is determined using a pair spectrometer, while the linear polarization of the photon beam is determined using a polarimeter based on triplet photoproduction. Charged-particle tracks from interactions in the central target are analyzed in a solenoidal field using a central straw-tube drift chamber and six packages of planar chambers with cathode strips and drift wires. Electromagnetic showers are reconstructed in a cylindrical scintillating fiber calorimeter inside the magnet and a lead-glass array downstream. Charged particle identification is achieved by measuring energy loss in the wire chambers and using the flight time of particles between the target and detectors outside the magnet. The signals from all detectors are recorded with flash ADCs and/or pipeline TDCs into memories allowing trigger decisions with a latency of $3.3\ \mu\text{s}$. The detector operates routinely at trigger rates of 40 kHz and data rates of 600 megabytes per second. We describe the photon beam, the GLUEX detector components, electronics, data-acquisition and monitoring systems, and the performance of the experiment during the first three years of operation.

71 **Contents**

72	1 The GlueX experiment	5
73	1.1 The Hall-D complex	6
74	1.2 Experimental requirements	9
75	1.3 Data requirements	10
76	1.4 Coordinate system	10
77	2 The coherent photon source and beamline	10
78	2.1 CEBAF electron beam	10
79	2.2 Hall-D photon beam	11
80	2.3 Goniometer and radiators	14
81	2.3.1 Diamond selection and quality control	15
82	2.4 Photon tagging system	17
83	2.4.1 Tagger magnet	18
84	2.4.2 Tagger Microscope	19
85	2.4.3 Broadband tagging hodoscope	21
86	2.5 Tungsten keV filter	23
87	2.6 Beam profiler	23
88	2.7 Active collimator	24
89	2.8 Collimator	25
90	2.9 Triplet Polarimeter	25

91	2.9.1	Determination of photon polarization	25
92	2.10	Pair Spectrometer	26
93	2.10.1	Determination of photon flux	27
94	2.11	Total Absorption Counter	28
95	3	Solenoid Magnet	28
96	3.1	Overview	28
97	3.2	Conductor and Coils	29
98	3.3	Cooling System	31
99	3.4	Measurements and Controls	31
100	3.5	Field calculation and measurement	32
101	4	Target	32
102	5	Tracking detectors	36
103	5.1	Central drift chamber	36
104	5.2	Forward Drift Chamber	38
105	5.3	Electronics	39
106	5.4	Gas system	40
107	5.5	Calibration, performance and monitoring	41
108	6	Performance of the charged-particle-tracking system	43
109	6.1	Track reconstruction	43
110	6.2	Momentum and vertex resolution	43
111	7	Electromagnetic calorimeters	45
112	7.1	Barrel Calorimeter	45
113	7.2	Forward Calorimeter	47
114	7.3	Electronics	48
115	7.4	Calibration and monitoring	49
116	7.5	Performance	49
117	8	Scintillation detectors	50
118	8.1	Start Counter	51
119	8.2	Time-of-Flight counters	52
120	8.3	Electronics	53
121	8.4	Calibration and monitoring	53
122	8.5	Performance	54
123	9	Trigger	57
124	9.1	Architecture	57
125	9.2	Trigger types	58
126	9.3	Performance	59
127	10	Data Acquisition	59

128	11 Slow controls	63
129	11.1 Architecture	63
130	11.2 Remote Units	63
131	11.3 Supervisory Control and Data Acquisition layer	64
132	11.4 Experiment Control System	64
133	12 Online computing system	65
134	12.1 Monitoring	65
135	12.2 Data transport and storage	66
136	13 Event reconstruction	68
137	13.1 Calibration	69
138	13.2 Monitoring	70
139	13.3 Reconstruction	70
140	13.4 Offsite reconstruction	71
141	13.5 Analysis	72
142	14 Monte Carlo	73
143	14.1 Geometry specification	73
144	14.2 Event generators	74
145	14.3 HDGEANT	75
146	14.4 Detector response	75
147	14.5 Job submission	75
148	15 Detector performance	76
149	15.1 Charged-particle reconstruction efficiency	76
150	15.2 Photon efficiency	77
151	15.3 Kinematic fitting	78
152	15.4 Invariant-mass resolution	80
153	15.5 Particle identification	82
154	16 Summary and outlook	85
155	17 Acknowledgments	86

156 **1. The GlueX experiment**

157 The search for Quantum ChromoDynamics (QCD) exotics uses data from
158 a wide range of experiments and production mechanisms. Historically, the
159 searches have looked for the gluonic excitations of mesons, searching for states
160 of pure glue, glueballs, and hybrid mesons where the gluonic field binding the
161 quark-anti-quark pair has been excited. Most experiments searching for glue-
162 balls looked for scalar mesons [1], where the searches relied on over-population
163 of nonets, as well as unusual meson decay patterns. In the search for hybrid
164 mesons [2, 3], efforts have focused on particles with exotic quantum numbers,
165 i.e. systems beyond simple quark-anti-quark configurations. Good evidence

166 exists for an isospin 1 state, the $\pi_1(1600)$. Looking collectively at past stud-
 167 ies, data from high-statistics photoproduction experiments in the energy range
 168 above 6 GeV are lacking.

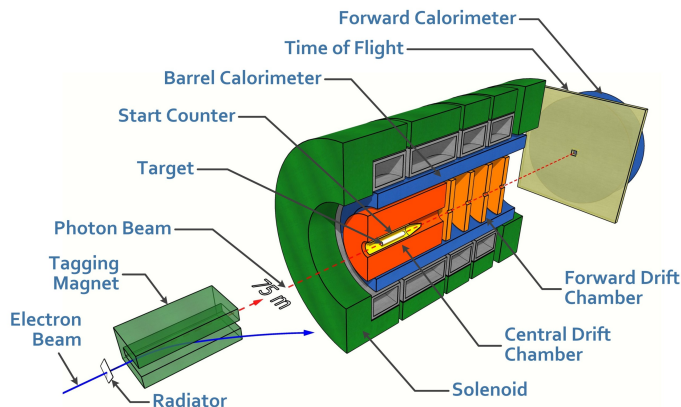


Figure 1: (Color online) A cut-away drawing of the GLUEX detector in Hall D, not to scale.

169 The *Gluonic Excitation* (GLUEX) experiment at the US Department of En-
 170 ergy’s Thomas Jefferson National Accelerator Facility (JLab)²⁰ has been built
 171 to search for and map out the spectrum of exotic hybrid mesons using a 9-GeV
 172 linearly-polarized photon beam incident on a proton target[4]. The GLUEX
 173 detector and beamline are shown schematically in Figure 1. The detector is
 174 nearly hermetic for both charged particles and photons arising from reactions
 175 in the cryogenic target at the center of the detector, allowing for reconstruction
 176 of exclusive final states. A 2-T solenoidal magnet surrounds the drift chambers
 177 used for charged-particle tracking. Two electromagnetic calorimeters cover the
 178 central and forward regions, and a scintillation detector downstream provides
 179 particle-identification capability through time-of-flight measurements.

180 1.1. The Hall-D complex

181 The GLUEX experiment is housed in the Hall-D complex at JLab (see Fig.2).
 182 This new facility starts with an extracted electron beam at the north end of the
 183 Continuous Electron Beam Accelerator Facility (CEBAF) [5, 6]. The electron
 184 beam is delivered to the Tagger Hall, where the maximum energy is 12 GeV,
 185 due to one more pass through the north linac than the other experimental halls
 186 (A, B and C). Here, linearly-polarized photons are produced through coherent
 187 bremsstrahlung off a $50\ \mu\text{m}$ thick diamond crystal radiator. The scattered elec-
 188 trons pass through a tagger magnet and are bent into tagging detectors. A
 189 high-resolution scintillating-fiber tagging array covers the 8 to 9 GeV energy

²⁰Thomas Jefferson National Accelerator Facility, 12000 Jefferson Ave., Newport News, VA 23606, <https://www.jlab.org>.

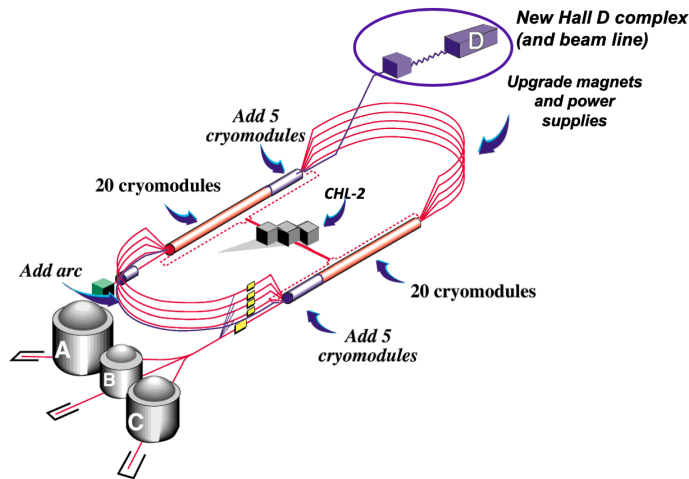


Figure 2: (Color online) Schematic of the CEBAF accelerator showing the additions made during the 12-GeV project. The Hall-D complex is located at the north-east end.

190 range, and a tagger hodoscope covers photon energies both from 9 GeV to the
 191 endpoint, and from 8 GeV to 3 GeV. Electrons not interacting in the diamond
 192 are directed into a 60 kW electron beam dump. The tagged photons travel to
 193 the Hall-D experimental hall. The distance from the radiator to the primary
 194 collimator is 75 m. The collimator of 5 mm diameter removes off-axis incoherent
 195 photons. The front face of the collimator is instrumented with an active colli-
 196 mator to aid in beam tuning. The beamline and tagging system are described
 197 below in Section 2.

198 Downstream of the primary collimator is a thin beryllium radiator used
 199 by both the Triplet Polarimeter, which measures the linear polarization of the
 200 photons, and a Pair Spectrometer, which is used to measure the flux of the
 201 photons. More information on the production, tagging and monitoring of the
 202 photon beam can be found in Section 2. The photon beam continues through
 203 to a liquid hydrogen target at the heart of the GLUEX detector, and then to
 204 the end of the experimental hall where it enters the photon beam dump.

205 The layout of the GLUEX detector is shown in Fig. 3. The spectrometer is
 206 based on a 4-m-long solenoidal magnet that is operated at a maximum field of
 207 2 T, see Section 3. The liquid-hydrogen target is located inside the upstream
 208 bore of the magnet. The target consists of a 2-cm-diameter, 30-cm-long vol-
 209 ume of hydrogen, as described in Section 4. Surrounding the target is the Start
 210 Counter, which consists of 30 thin scintillator paddles that bend to a nose on
 211 the down-stream end of the hydrogen target. The Start Counter is the primary
 212 detector that registers the time coincidence of the radio-frequency (RF) bunch
 213 containing the incident electron and the tagged photon producing the interaction.
 214 More information on this scintillator detector can be found in Section 8.

215 The Central Drift Chamber, a cylindrical straw-tube detector, starts at a

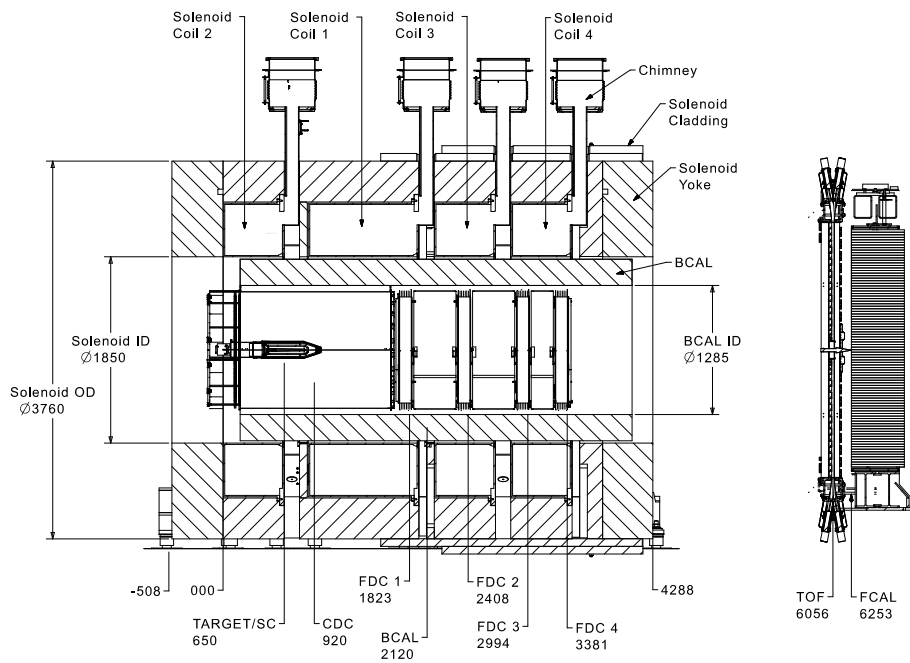


Figure 3: GlueX spectrometer layout. Dimensions are given in mm. The numbers show the Z-coordinates of the detectors' centers, or of the front face of the FCAL modules. Glossary: SC - Start Counter (Section 8.1), CDC - Central Drift Chamber (Section 5.1), FDC - Forward Drift Chamber (Section 5.2), BCAL - Barrel Calorimeter (Section 7.1), TOF - Time-of-Flight hodoscope (Section 8.2), FCAL - Forward Calorimeter (Section 7.2).

216 radius of 10 cm from the beam line. The active volume of the chamber extends
217 from 48 cm upstream to 102 cm downstream of the target center, and from
218 10 cm to 56 cm in radius. The Central Drift Chamber consists of 28 layers of
219 straw tubes in axial and two stereo orientations. Downstream of the central
220 tracker is the Forward Drift Chamber, which consists of four packages, each
221 containing 6 planar layers in alternating u - y - v orientations. Both cathodes and
222 anodes in the Forward Drift Chamber are read out, providing three-dimensional
223 space point measurements. More details on the tracking system are provided in
224 Sections 5 and 6.

225 Downstream of the magnet is the Time-of-Flight wall. This system consists
226 of two layers of scintillator paddles in a crossed pattern, and, in conjunction with
227 the Start Counter, is used to measure the flight time of charged particles. More
228 information on the time-of-flight system is provided in Section 8. Photons arising
229 from interactions within the GLUEX target are detected by two calorimeter
230 systems. The Barrel Calorimeter, located inside the solenoid, consists of layers
231 of scintillating fibers alternating with lead sheets. The Forward Calorimeter is
232 downstream of the Time-of-Flight wall, and consists of 2800 lead-glass blocks.
233 More information on the the calorimeters can be found in Section 7.

234 1.2. Experimental requirements

235 The physics goals of the GlueX experiment require the reconstruction of exclu-
236 sive final states. Thus, the GLUEX detector must be able to reconstruct both
237 charged particles (π^\pm , K^\pm and p/\bar{p}) and particles decaying into photons (π^0 , η ,
238 ω and η'). For this capability, the charged particles and photons must be re-
239 constructed with good momentum and energy resolution. The experiment must
240 also be able to reconstruct the energy of the incident photon (8 to 9 GeV) with
241 high accuracy (0.1%) and have knowledge of the linear polarization (maximum
242 $\sim 40\%$) of the photon beam to an absolute precision of 1%. Finally, many inter-
243 esting final states involve more than five particles. Thus, the GLUEX detector
244 must also be nearly hermetic for both charged particles and photons, with an
245 acceptance that is reasonably uniform, well understood, and accurately modeled
246 in simulation.

247 In practice, the typical momentum resolution for charged particles is 1–3%,
248 while the resolution is 8–9% for very-forward high-momentum particles. For
249 most charged particles, the tracking system has nearly hermetic acceptance for
250 polar angles from $1^\circ - 2^\circ$ to 150° . However, protons with momenta below about
251 250 MeV/c are absorbed in the hydrogen target and not detected. A further
252 challenge is the reconstruction of tracks from charged pions with momenta under
253 200 MeV/c due to spiraling trajectories in the magnetic field. The measurement
254 of energy loss (dE/dx) in the Central Drift Chamber enables the separation of
255 pions and protons up to about 800 MeV/c, while time-of-flight determination
256 allows separation of forward-going pions and kaons up to about 2 GeV/c.

257 For photons produced from the decays of reaction products, the typical en-
258 ergy resolution is 5 to 6%/ $\sqrt{E_\gamma}$. Photons above 60 MeV can be detected in
259 the Barrel Calorimeter, with some variation depending on the incident angle.
260 The interaction point along the beam direction is determined by comparing the

261 information from the readouts on the upstream and downstream ends of the de-
262 tector. In the Forward Calorimeter, photons with energies larger than 100 MeV
263 can be detected with uniform resolution across the face of the detector. There
264 is a gap between the calorimeters at around 11° , where energy can be lost due
265 to shower leakage. Both photon detection efficiency and energy resolution are
266 degraded in this region.

267 *1.3. Data requirements*

268 The physics analyses need to be carried out in small bins of energy and
269 momentum transfer, necessitating not only the ability to reconstruct exclusive
270 final states but also to collect sufficient statistics. While exact cross sections are
271 not known, the cross sections of interest will be in the 10 nb to $1 \mu\text{b}$ range.

272 This paper describes the operation of GLUEX Phase I. During this initial
273 phase, the GLUEX experiment has run with a data acquisition system capable of
274 collecting data using photon beams of a few $10^7 \gamma/\text{s}$ in the coherent peak (8.4-9
275 GeV), with an expectation to run with 2.5 times higher rates in the future. The
276 data acquisition system ran routinely at 40 kHz with raw event sizes of 15-20
277 kilobytes, collecting about 600 megabytes of data per second. With firmware
278 improvements, future running is expected at 90 kHz and 1 gigabyte per second.
279 Details of the trigger and data acquisition are presented in Sections 9 and 10.

280 *1.4. Coordinate system*

281 For reference, we introduce here the overall experiment coordinate system,
282 which is used in this document and throughout the analysis. The z-axis is
283 defined along the nominal beamline increasing downstream. The coordinate
284 system is right-handed with the y-axis pointing vertically up and the x-axis
285 pointing approximately north. The origin is located 50.8 cm (20 inches) down-
286 stream of the upstream side of the upstream endplate of the solenoid, placing
287 the nominal center of the target at (0,0,65 cm).

288 **2. The coherent photon source and beamline**

289 *2.1. CEBAF electron beam*

290 CEBAF has a race track configuration with two parallel linear accelerators
291 based on superconducting radio frequency (RF) technology [5]. The machine
292 operates at 1.497 GHz and delivers beam to Hall D at 249.5 MHz.²¹ Precise
293 timing signals for the accelerator beam bunches are available to the experiment
294 and are used to determine the time that individual photon bunches pass through
295 the target. The nominal properties for the CEBAF electron beam to the Tagger
296 Hall are listed in Table 1.

²¹Hall D beam at 499 MHz is possible, but not the norm.

Table 1: Electron beam parameters. The emittance, energy spread and related parameters are estimates based on a model of the transport line from the accelerator to the Hall D radiator. The dimensions of the beam spot at the position of the radiator are directly measured, and vary around the stated values by $\pm 30\%$ depending on beam conditions. Values for image size at collimator, obtained by projection of the electron beam spot convergence forward to the position of the primary photon collimator, have relative uncertainties of 50%.

parameter	design results
energy	12 GeV
energy spread, RMS	2.2 MeV
transverse x emittance	2.7 mm $\cdot\mu$ rad
transverse y emittance	1.0 mm $\cdot\mu$ rad
x spot size at radiator, RMS	1.1 mm
y spot size at radiator, RMS	0.7 mm
x image size at collimator, RMS	0.5 mm
y image size at collimator, RMS	0.5 mm
image offset from collimator axis, RMS	0.2 mm
distance radiator to collimator	75.3 m

297 *2.2. Hall-D photon beam*

298 The Hall-D complex, described in Section 1.1 and shown schematically in
 299 Fig. 4, includes a dedicated Tagger Hall, an associated collimator cave, and
 300 Experimental Hall D itself. A linearly-polarized photon beam is created using
 301 the process of coherent bremsstrahlung [7, 8] when the electron beam passes
 302 through an oriented diamond radiator at the upstream end of the Tagger Hall.
 303 The electron beam position at the radiator is monitored and controlled using
 304 beam position monitors (5C11 and 5C11B) which are located at the end of the
 305 accelerator tunnel just upstream of the Tagger Hall (see Fig. 4.) The CEBAF
 306 electron beam is tuned to converge as it passes through the radiator, ideally
 307 so that the electron beam forms a virtual focus at the collimator located 75 m
 308 downstream of the radiator. At the collimator, the virtual spot size of 0.5 mm
 309 is small compared to the cm-scale size of the photon beam on the front face of
 310 the collimator, such that a cut on photon position at the collimator is effectively
 311 a cut on photon emission angle at the radiator. The convergence properties of
 312 the electron beam are measured by scanning the beam profile with vertical and
 313 horizontal wires. The wire scanners are referred to as "harps." Examples of the
 314 horizontal and vertical convergence of the electron beam envelope (undeflected
 315 by the tagger magnet) measured using harp scans and projected downstream
 316 along the beamline are shown in Fig. 5.

317 The photon beam position on the collimator is monitored using an active
 318 collimator positioned just upstream of the primary photon beam collimator
 319 (described below in section 2.7). The position stability of the photon beam
 320 is maintained during normal operation by a feedback system that locks the position
 321 of the electron beam at the 5C11B beam position monitor and, consequently,
 322 the photon beam at the active collimator. The stability of the electron beam

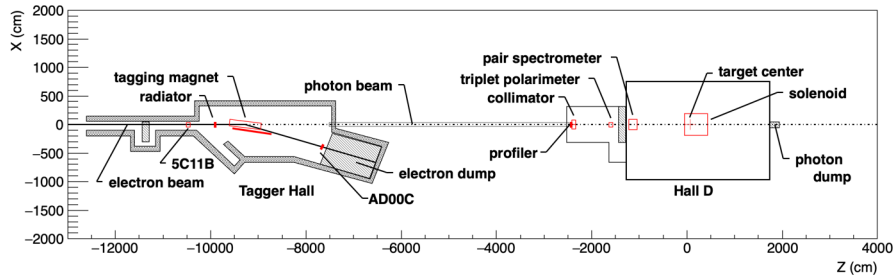


Figure 4: Schematic layout of the Hall-D complex, showing the Tagger Hall, Hall D, and several of the key beamline devices. Also indicated are the locations of the 5C11B and AD00C beam monitors.

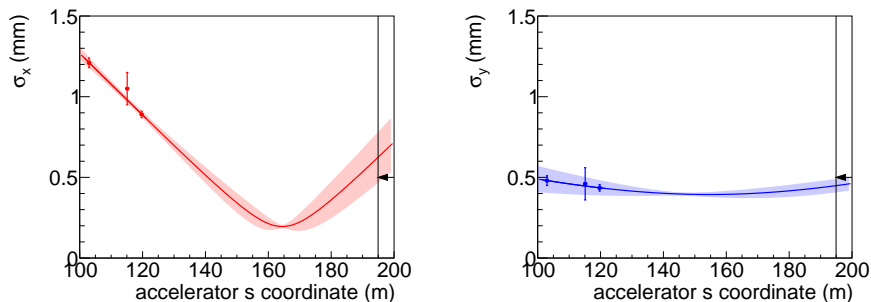


Figure 5: (Color online) Measurements of the root-mean-square width of the electron beam in horizontal (left) and vertical (right) projections as a function of position along the beamline, based on harp scans (data points) of the electron beam. The radiator position is just upstream of the third data point. The primary collimator position is marked by the vertical line indicated by the arrow. The curve downstream of the radiator is an extrapolation from the measured data points, with extrapolation uncertainty indicated by the shaded regions.

323 current and position is monitored using an independent beam monitor (AD00C
 324 in Fig. 4) located immediately upstream of the electron dump.

325 The linearly-polarized photon beam is produced via a radiator placed in the
 326 electron beam just upstream of the Tagger (section 2.4). A properly aligned
 327 20–60 μm thick diamond crystal radiator produces linearly polarized photons
 328 via coherent bremsstrahlung in enhancements [7, 8], that appear as peaks at
 329 certain energies in the collimated bremsstrahlung intensity spectrum (Fig. 6),
 330 superimposed upon the ordinary continuum bremsstrahlung spectrum from an
 331 aluminum radiator. The energies of the coherent photon peaks and the degree
 332 of polarization in each of those peaks depend on the crystal orientation with
 333 respect to the incident electron beam. Adjustment of the orientation of the
 334 diamond crystal with respect to the incoming electron beam permits production
 335 of essentially any coherent photon peak energy up to that of the energy of the

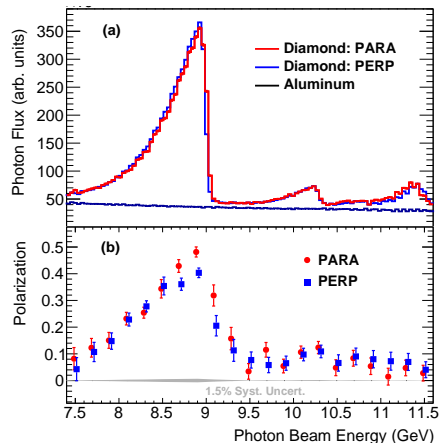


Figure 6: (color online) (a) Collimated photon beam intensity versus energy as measured by the Pair Spectrometer. (b) Collimated photon beam polarization as a function of beam energy, as measured by the Triplet Polarimeter, with data points offset horizontally by ± 0.015 GeV for clarity. The labels PARA and PERP refer to orientations of the diamond radiator that result in polarization planes that are parallel and perpendicular to the horizontal, respectively.

336 incident electron beam, as well as the degree or direction of linear polarization.
 337 A choice of 9 GeV for the primary peak energy, corresponding to 40% peak
 338 linear polarization, was found to be optimum for the GLUEX experiment with
 339 a 12-GeV incident electron beam.

340 The degree of polarization for a coherent bremsstrahlung beam is great-
 341 est for photons emitted at small angles with respect to the incident electron
 342 direction. Collimation of the photon beam to a fraction of the characteristic
 343 bremsstrahlung angle exploits this correlation to significantly enhance the average
 344 polarization of the beam. In the nominal GLUEX beamline configuration,
 345 a 5.0-mm-diameter collimator²² positioned 75 m downstream of the radiator is
 346 used, corresponding to a cut at approximately $1/2 m/E$ in characteristic angle,
 347 where m is the electron rest mass and E is the energy of the incident elec-
 348 tron. The photon beam energy spectrum and photon flux after collimation are
 349 measured by the Pair Spectrometer (section 2.10), located downstream of the
 350 collimator in Hall D.

351 An example of the measured photon spectrum and degree of polarization
 352 with a 12-GeV electron beam is shown in Fig. 6. The spectrum labeled “Alu-
 353 minium” in Fig. 6(a) shows the spectrum of ordinary (incoherent) bremsstrah-
 354 lung, normalized to the approximate thickness of the diamond radiator in terms
 355 of radiation lengths. The expected degree of linear polarization in the energy
 356 range of 8.4–9.0 GeV is $\sim 40\%$ after collimation. The photon beam polariza-

²²A 3.4 mm collimator is also available, and has been used for some physics production runs with the thinnest (20 μm) diamond.

Table 2: Typical parameters for the GLUEX photon beam, consistent with the electron beam properties listed in Table 1, a diamond radiator of thickness $50\ \mu\text{m}$, and the standard primary collimator of diameter $5.0\ \text{mm}$ located at the nominal position. The electron beam current incident on the radiator is taken to be $150\ \text{nA}$. The hadronic rates are calculated for the GLUEX $30\ \text{cm}$ liquid hydrogen target.

E upper edge of the coherent peak	9 GeV
Coherent peak effective range	8.4 - 9.0 GeV
Net tagger rate in the coherent peak range	45 MHz
N_γ in the peak range after collimator	24 MHz
Maximum polarization in the peak, after collimator	40%
Mean polarization in the peak range, after collimator	35%
Power absorbed on collimator	0.60 W
Power incident on target	0.23 W
Total hadronic rate	70 kHz
Hadronic rate in the peak range	3.7 kHz

tion is directly measured by the triplet polarimeter (section 2.9) located just upstream of the pair spectrometer. The stability of the beam polarization is independently monitored via the observed azimuthal asymmetry in various photoproduction reactions, particularly that for ρ photoproduction [9].

Typical values for parameters and properties of the photon beam are given in Table 2. In the sections that follow, we describe in more detail how the linearly-polarized photon beam is produced, how the photon energy is determined using the tagging spectrometer, how the photon beam polarization spectrum and flux are measured with the Pair Spectrometer and Triplet Polarimeter, and how the photon flux is calibrated using the Total Absorption Counter.

2.3. Goniometer and radiators

For the linearly-polarized photon beam normally used in GLUEX production running, diamond radiators are used to produce a coherent bremsstrahlung beam. This requires precise alignment of the diamond radiator, in order to produce a single dominant coherent peak²³ with the desired energy and polarization by scattering the beam electrons from the crystal planes associated with a particular reciprocal lattice vector. A multi-axis goniometer, manufactured by Newport Corporation, precisely adjusts the relative orientation of the diamond radiator with respect to the incident electron beam horizontally, vertically and rotationally about the X , Y and Z axes, respectively. The Hall-D goniometer holds several radiators, any of which may be moved into the beam for use at any time according to the requirements of the experiment.

In addition to the diamond radiators, several aluminum radiators of thicknesses ranging from 1.5 to $40\ \mu\text{m}$ are used to normalize the rate spectra measured

²³Defined as $0.6\ \text{GeV}$ below the coherent edge (nominally $9\ \text{GeV}$). The position of the edge scales approximately with the primary incident electron beam energy.

381 in the Pair Spectrometer, correcting for its acceptance. A separate rail for these
382 amorphous radiators is positioned 615 mm downstream of the goniometer.

383 *2.3.1. Diamond selection and quality control*

384 The properties of diamond are uniquely suited for coherent bremsstrahlung
385 radiators. The small lattice constant and high Debye temperature of diamond
386 result in an exceptionally high probability for coherent scattering in the brems-
387 strahlung process [10]. Also, the high coherent scattering probability is a conse-
388 quence of the small atomic number of carbon ($Z = 6$). At the dominant crystal
389 momentum (9.8 keV) corresponding to the leading (2,2,0) reciprocal lattice vec-
390 tor, the small atomic number results in minimal screening of the nuclear charge
391 by inner shell electrons. Diamond is the best known material in terms of its
392 coherent radiation fraction, and its unparalleled thermal conductivity and ra-
393 diation hardness make it well-suited for use in a high-intensity electron beam
394 environment.

395 The position of the coherent edge in the photon beam intensity spectrum is
396 a simple monotonic function of the angle between the incident electron beam
397 direction and the normal to the (2,2,0) crystal plane. The 12-GeV-electron
398 beam entering the radiator has a divergence less than $10 \mu\text{rad}$, corresponding
399 to a broadening of the coherent edge in Fig. 6 by just 7 MeV. However, if the
400 incident electron beam had to travel through $100 \mu\text{m}$ of diamond material prior
401 to radiating, the resulting electron beam emittance would increase by a factor
402 of 10 due to multiple Coulomb scattering, resulting in a proportional increase in
403 the width of the coherent edge. Such broadening of the coherent peak diminishes
404 both the degree of polarization in the coherent peak as well as the collimation
405 efficiency in the forward direction. Hence, diamond radiators for GLUEX must
406 be significantly thinner than 100 microns.

407 The cross-sectional area of a diamond target must also be large enough to
408 completely contain the electron beam so that the beam does not overlap with
409 the material of the target holder. Translated to the beam spot dimensions from
410 Table 1, GLUEX requires a target with transverse size 5 mm or greater. Uniform
411 single-crystal diamonds of this size are now available as slices cut from natural
412 gems, HPHT (high-pressure, high-temperature) synthetics, and CVD (chemical
413 vapor deposition) single crystals. Natural gems are ruled out due to cost. HPHT
414 crystals had been thought to be far superior to CVD single crystals in terms
415 of their diffraction widths, but our experience did not bear this out. GLUEX
416 measurements of the x-ray rocking curves of CVD crystals obtained from the
417 commercial vendor Element Six²⁴ routinely showed widths that were within a
418 factor 2 of the theoretical Darwin width, similar to the results we found for the
419 best HPHT diamonds that were available to us [11, 12].

420 Fig. 7 shows a rocking curve topograph of a diamond radiator taken with
421 15 keV x-rays at the Cornell High Energy Synchrotron Source (CHESS). The
422 instrumental resolution of this measurement is of the same order as the Darwin

²⁴Element Six, <https://www.e6.com/en>.

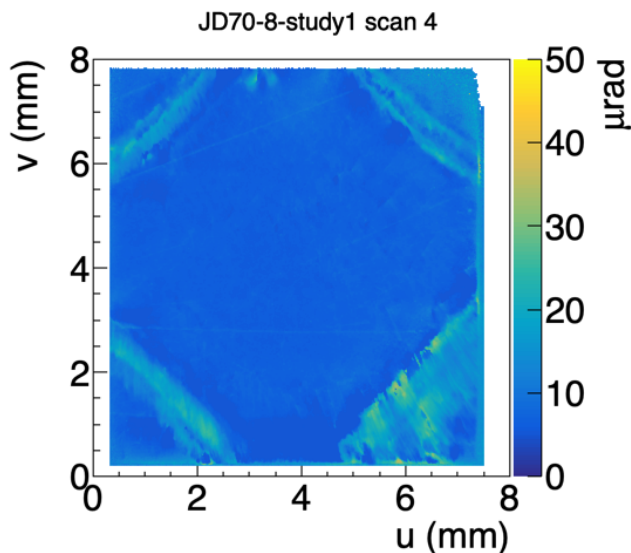


Figure 7: (color online) Rocking curve RMS width topograph taken of the (2,2,0) reflection from a CVD diamond crystal using 15 keV X-rays at the C-line at CHESS. The bright diagonal lines in the corners indicate regions of increased local strain, coinciding with growth boundaries radiating outward from the seed crystal used in the CVD growth process.

423 width for this diffraction peak, approximately $5 \mu\text{rad}$. During operation, the
 424 electron beam spot would be confined to the relatively uniform central region.
 425 Any region in this figure with a rocking curve root-mean-square width of $20 \mu\text{rad}$
 426 or less is indistinguishable from a perfect crystal for the purposes of GLUEX.
 427 Regardless of whether or not better HPHT diamonds exist, these Element Six
 428 CVD diamonds have sufficiently narrow diffraction widths for our application.
 429 This, coupled with their lower cost relative to HPHT material, made them the
 430 obvious choice for the Hall-D photon source.

431 The diamond radiator fabrication procedure began with procurement of the
 432 raw material in the form of $7 \times 7 \times 1.2 \text{ mm}^3$ CVD single-crystal plates from
 433 the vendor. After x-ray rocking curve scans of the raw material were taken
 434 to verify crystal quality, the acceptable diamonds were shipped to a second
 435 vendor, Delaware Diamond Knives (DDK). At DDK, the 1.2-mm-thick samples
 436 were sliced into three samples of $250 \mu\text{m}$ thickness each, then each one was
 437 polished on both sides down to a final thickness close to $50 \mu\text{m}$. The samples,
 438 now of dimensions $7 \times 7 \times 0.05 \text{ mm}^3$ were fixed to a small aluminum mounting
 439 tab using a tiny dot of conductive epoxy placed in one corner. These crystals
 440 were then returned to the synchrotron light source for final x-ray rocking curve
 441 measurements prior to final approval for use in the GLUEX photon source.

442 The useful lifetime of a diamond radiator in the GLUEX beamline is limited
 443 by the degradation in the sharpness of the coherent edge due to accumulation

444 of radiation damage. Experience during the early phase of GLUEX running
445 showed that after exposure to about 0.5 C of integrated electron beam charge,
446 the width of the coherent edge increased enough that the entire coherent peak
447 was no longer contained within the energy window of the tagger microscope.
448 When a crystal reached this degree of degradation, the radiator was regarded
449 as no longer usable, and a new crystal was installed.

450 During Phase 1 of GLUEX, radiator crystals were replaced three times due
451 to degradation, twice with 50 μm radiators and once with a 20 μm radiator. The
452 20- μm diamond was introduced to test whether the reduced multiple Coulomb
453 scattering might result in an observable increase in peak polarization. This
454 turned out not to be the case, for two reasons. The first is that to take full
455 advantage of the reduced multiple scattering in the radiator for increased peak
456 polarization, the collimator size must be reduced proportionally. A 3.4-mm-
457 diameter collimator was available for this purpose, but variability observed in
458 the convergence properties of the electron beam at the radiator overruled run-
459 ning with any collimator smaller than 5 mm, even when a thinner radiator was
460 in use.

461 The second reason is that any improvements from reduced multiple scat-
462 tering that came with the smaller radiator thickness were more than offset by
463 strong indications of radiation damage that appeared not long after the 20 μm
464 crystal was put into production. The rapid appearance of radiation damage was
465 partly due to the larger beam current (factor 2.5) that was needed to produce
466 the same photon flux as with a 50 μm crystal, but that factor alone did not
467 fully explain what was seen. Subsequent x-ray measurements showed that a
468 large buckling of the 20 μm crystal had occurred in the region of the incident
469 electron beam spot, evidently due to local differential expansion of the diamond
470 lattice arising from radiation damage. Once the crystal buckled, the energy
471 of the coherent peak varied significantly across the electron beam spot, effec-
472 tively broadening the peak. Fortunately, the greater stiffness of a 50 μm crystal
473 appears to suppress this local buckling under similar conditions of radiation
474 damage.

475 Based on these observations, 50 μm was selected as the optimum thickness
476 for GLUEX diamond radiators: thin enough to limit the effects of multiple
477 scattering and thick enough to suppress buckling from internal stress induced by
478 radiation damage. The effective useful lifetime of a 50 μm radiator in the photon
479 source is about 0.5 C integrated incident electron charge. This lifetime might
480 be extended somewhat by the use of thermal annealing to partially remove the
481 effects of radiation damage. This possibility will be explored when the pace of
482 diamond replacement increases with the start of full-intensity running (GLUEX
483 Phase 2) and the number of spent radiators starts to accumulate.

484 *2.4. Photon tagging system*

485 After passing through the radiator, the combined photon and electron beams
486 enter the photon tagging spectrometer (Tagger). The full-energy electrons are
487 swept out of the beamline by a dipole magnet and redirected into a shielded
488 beam dump. The subset of beam electrons that radiated a significant fraction

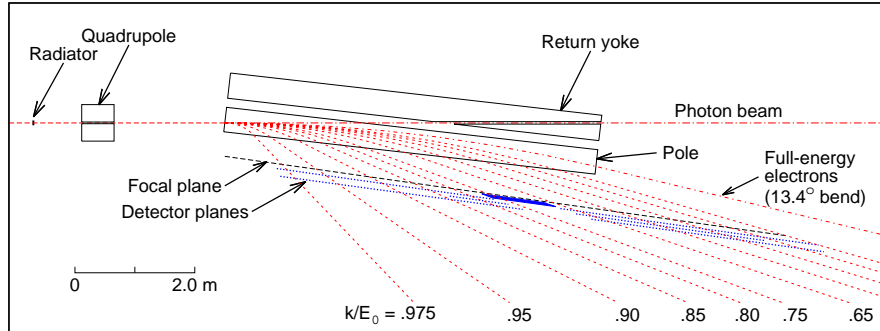


Figure 8: Schematic diagram of the tagging spectrometer, showing the paths of the electron and photon beams. Dotted lines indicate post-radiation electron trajectories identified by the energy the electron gave up to an associated radiated photon, as a fraction of the beam energy E_0 . The Tagger focal plane detector arrays TAGH and TAGM are described in the text.

489 of their energy in the radiator are deflected to larger angles by the dipole field.
 490 These post-bremsstrahlung electrons exit through a thin window along the side
 491 of the magnet, and are detected in a highly segmented array of scintillators
 492 called the Tagger Hodoscope, as shown in Fig. 8. The TAGH counters span
 493 the full range in energy from 25% to 97% of the full electron beam energy. A
 494 high-energy-resolution device known as the Tagger Microscope (TAGM) covers
 495 the energy range corresponding to the primary coherent peak, indicated by the
 496 denser portion of the focal plane in Fig. 8. The quadrupole magnet upstream of
 497 the Tagger dipole provides a weak vertical focus, optimizing the efficiency of the
 498 Tagger Microscope for tagging collimated photons. A 0.8 Tm permanent dipole
 499 magnet is installed downstream of the Tagger magnet on the photon beam line,
 500 in order to prevent the electron beam from reaching Hall D should the Tagger
 501 magnet trip.

502 Both the TAGM and TAGH devices are used to determine the energy of
 503 individual photons in the photon beam via coincidence, using the relation $E_\gamma =$
 504 $E_0 - E_e$, where E_0 is the primary electron beam energy before interaction with
 505 the radiator, and E_e is the energy of the post-bremsstrahlung electron deter-
 506 mined by its detected position at the focal plane. Multiple radiative interactions
 507 in a $50 \mu\text{m}$ diamond radiator (3×10^{-4} radiation lengths) produce uncertainties
 508 in E_γ of the same order as the intrinsic energy spread of the incident electron
 509 beam.

510 2.4.1. Tagger magnet

511 The Hall-D Tagger magnet deflects electrons in the horizontal plane, allow-
 512 ing the bremsstrahlung-produced photons to continue to the experimental hall
 513 while bending the electrons that produced them into the focal plane detectors.
 514 Electrons that lose little or no energy in the radiator are deflected by 13.4° into
 515 the electron beam dump.

516 The Hall-D Tagger magnet is an Elbek-type room temperature dipole mag-
 517 net, similar to the JLab Hall-B tagger magnet [13, 14]. The magnet is 1.13 m
 518 wide, 1.41 m high and 6.3 m long, weighing 80 metric tons, with a normal op-

519 erating field of 1.5 T for a 12-GeV incident electron beam, a maximum field of
520 1.75 T, and a pole gap of 30 mm. The magnet design was optimized using the
521 detailed magnetic field calculation provided by the TOSCA simulation package
522 and ray tracing of electron beam trajectories [15, 16].

523 The GLUEX experiment requirements mandate that the scattered electron
524 beam be measured with an accuracy of 12 MeV (0.1% of the incident electron
525 energy). This requires that the magnetic field integrals along all useful electron
526 trajectories be known to 0.1%. The magnetic field was mapped at Jefferson Lab
527 and the detailed field maps were augmented by detailed TOSCA calculations,
528 which have allowed us to meet these goals. Details of the magnet mapping and
529 uniformity are found in Ref. [17].

530 *2.4.2. Tagger Microscope*

531 The Tagger Microscope (TAGM) is a high-resolution hodoscope that counts
532 post-bremsstrahlung electrons corresponding to the primary coherent peak. Nor-
533 mally the TAGM is positioned to cover between 8.2 and 9.2 GeV in photon en-
534 ergy, but the TAGM is designed to be movable should a different peak energy be
535 desired. The microscope is segmented along the horizontal axis into 102 energy
536 bins (columns) of approximately equal width. Each column is segmented in five
537 sections (rows) along the vertical axis. The vertical segmentation allows the
538 possibility of scattered electron collimation, which gives a significant increase
539 in photon polarization when used in combination with photon collimation. The
540 purpose of the quadrupole magnet upstream of the dipole is to provide the
541 vertical focus needed to make the double-collimation scheme work efficiently.
542 Summed signals are also available for each column for use in normal operation
543 when electron collimation is not desired.

544 The Tagger Microscope consists of a two-dimensional array of square scin-
545 tillating fibers packed in a dense array of dimensions 102×5 . The fibers are
546 multi-clad BCF-20 with a 2×2 mm² square transverse profile, manufactured
547 by Saint-Gobain²⁵. The cladding varies in thickness from 100 microns near
548 the corners to 70 microns in the middle of the sides, with an active area of
549 1.8×1.8 mm² per fiber. Variations at the level of 5% in the transverse size of
550 the fibers impose a practical lower bound of 2.05 mm on the pitch of the array.
551 The detection efficiency of the TAGM averages 75% across its full energy range,
552 in good agreement with the geometric factor of 77%.

553 Each scintillating fiber is 10 mm long, fused at its downstream end to a
554 clear light guide of matching dimensions (Saint-Gobain BCF-98) that transmits
555 the scintillation light from the focal plane to a shielded box where a silicon
556 photomultiplier (SiPM) converts light pulses into electronic signals. The scin-
557 tillators are oriented so that the electron trajectories are parallel to the fiber
558 axis, providing large signals for electrons from the radiator, in contrast to the
559 omni-directional electromagnetic background in the tagger hall.

560 Because the electron trajectories do not cross the focal plane at right angles,

²⁵Saint-Gobain, <https://www.saint-gobain.com/en>

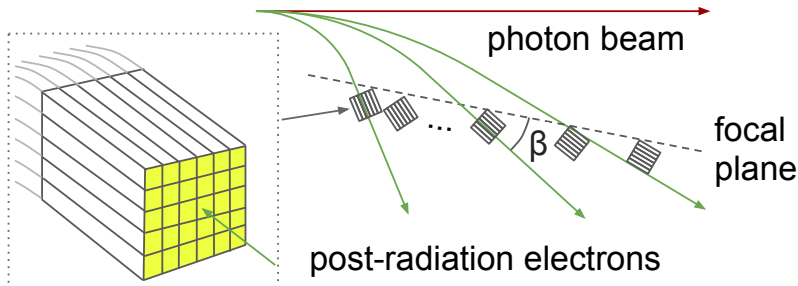


Figure 9: Conceptual overview of the tagger microscope design, showing the fiber bundles and light guides (left), and the orientation of these bundles aligned with the incoming electron beam direction in the tagger focal plane (right). The variation of the crossing angle β is exaggerated for the sake of illustration.

561 the fiber array must be staggered along the dispersion direction. A staggering
 562 step occurs every 6 columns, as illustrated in Fig. 9. The slight variation of
 563 the crossing angle β is taken into account by a carefully adjusted fan-out that
 564 is implemented by small evenly-distributed gaps at the rear ends of adjacent
 565 6-column groups (bundles). A total of 17 such bundles comprise the full Tagger
 566 Microscope.

567 The far ends of the scintillation light guides are coupled to Hamamatsu
 568 S10931-050P SiPMs. The SiPMs are mounted on a custom-built two-stage
 569 preamplifier board, with 15 SiPMs per board. In addition to the 15 individual
 570 signals generated by each preamplifier, the boards also produce three analog
 571 sum outputs, each the sum of five adjacent SiPMs corresponding to the five
 572 fibers in a single column. All 510 SiPMs are individually biased by custom bias
 573 control boards, one for every two preamplifier boards. The control boards con-
 574 nect to the preamplifiers over a custom backplane, and communicate with the
 575 experimental slow controls system over ethernet. Each control board has the
 576 capability to electronically select between two gain modes for the preamplifiers
 577 on that board: a low gain mode used during regular tagging operation, and a
 578 high gain mode used for triggering on single-pixel pulses during bias calibration.
 579 Each bias control board manages the control and biasing for two preamplifiers.
 580 The control board also measures live values for environmental parameters (volt-
 581 age levels and temperatures) in the TAGM electronics, so that alarms can be
 582 generated by the experimental control system whenever any of these parameters
 583 stray outside predefined limits.

584 Pulse height and timing information for 122 channels from the TAGM is
 585 provided by analog-to-digital converters (ADCs) and time-to-digital converters
 586 (TDCs). These 122 signals include the 102 column sums plus the individual
 587 fiber signals from columns 7, 27, 81, and 97. Here, each channel goes through
 588 a 1:1 passive splitter, with one output going to an ADC and the other through

589 discriminators to a TDC. The ADCs are 250-MHz flash ADCs with 12-bit res-
590 olution and a full-scale pulse amplitude of 1 V. The TDCs are based on the F1
591 TDC chip [18], with a least-count of 62 ps. Pulse thresholds in both the ADC
592 and discriminator modules are programmable over the range 1-1000 mV on an
593 individual channel basis, covering the full dynamic range of the TAGM front
594 end. The TAGM preamplifier outputs (before splitting) saturate at around 2 V
595 pulse amplitude.

596 The mean pulse charge in units of SiPM pixels corresponding to a single
597 high-energy electron varies from 150 to 300 pC, depending on the fiber, with
598 an average of 220 pC and standard deviation of 25 pC. During calibration, this
599 yield is measured individually for each fiber by selectively biasing the SiPMs on
600 each row of fibers, one row at a time, and reading out the column sums. Once
601 all 510 individual fiber yields have been measured, the bias voltages within each
602 column are adjusted to compensate for yield variations, so that the mean pulse
603 height in a given column is the same regardless of which fiber in the column
604 detected the electron. The ADC readout and discriminator thresholds are set
605 individually for each column, for optimum efficiency and noise rejection.

606 The ADC firmware provides an approximate time for each pulse, in addition
607 to the pulse amplitude. During offline reconstruction, this time information
608 is used to associate ADC and TDC pulse information from the same channel,
609 so that a time-walk correction can be applied to the TDC time. Once this
610 correction has been applied, a time resolution of 230 ps is achieved for the
611 TAGM. This resolution is based on data collected at rates on the order of 1 MHz
612 per column, while the typical rate in the tagger microscope is about 0.5 MHz.
613 The readout was designed to operate at rates up to 4 MHz per column. A brief
614 test above 2 MHz per column allowed visual inspection of the pulse waveforms
615 from the TAGM, without change in the pulse shape or amplitude.

616 *2.4.3. Broadband tagging hodoscope*

617 The Tagger Hodoscope (TAGH) consists of 222 scintillator counters dis-
618 tributed over a length of 9.25 m and mounted just behind the focal plane of
619 the tagger magnet. The function of this hodoscope is to tag the full range of
620 photon energy from 25% to 97% of the incident electron energy. A gap in the
621 middle of that range is left open for the registration of the primary coherent
622 peak by the Tagger Microscope. The geometry of the counters in the vicinity
623 of the microscope is shown in Fig. 10. This broad coverage aids in alignment of
624 the diamond radiator and expands the GLUEX physics program reach to photon
625 energies outside the range of the coherent peak. The coverage of the hodoscope
626 counters in the region below 60% drops to half, with substantial gaps in energy
627 between the counters. This was done because the events of primary interest to
628 GLUEX come from interactions of photons within and above the coherent peak;
629 within and above the coherent peak the coverage is 100% up to the 97% E_0
630 cutoff.

631 Each counter in the hodoscope is a sheet of EJ-228 scintillator, 6 mm thick
632 and 40 mm high. The counter widths vary along the focal plane, from 21 mm

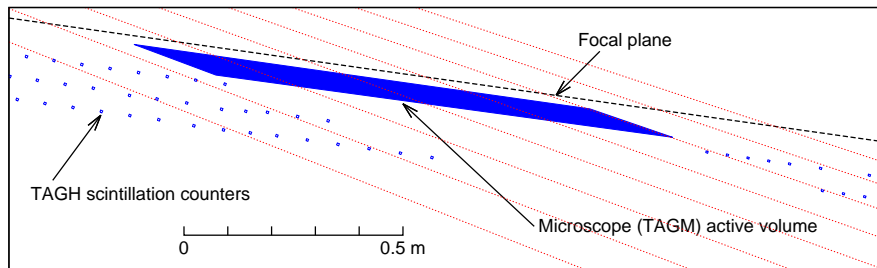


Figure 10: Schematic of electron trajectories in the region of the microscope. Shown are the three layers of hodoscope counters on either side of the microscope and the region covered by the microscope.

633 near the end-point region down to 3 mm at the downstream end. The scintil-
 634 lators are coupled to a Hamamatsu R9800 photomultiplier tube (PMT) via a
 635 cylindrical acrylic (UVT-PMMA) light guide 22.2 mm in diameter and 120 mm
 636 long. Each PMT is wrapped in μ -metal to shield the tube from the fringe field
 637 of the tagger magnet.

638 Each PMT is instrumented with a custom designed active base [19], consist-
 639 ing of a high-voltage divider and an amplifier powered by current flowing
 640 through the divider. The base provides two signal outputs, one going to a flash
 641 ADC and the other through a discriminator to a TDC. Operating the amplifier
 642 with a gain factor of 8.5 allows the PMT to operate at a lower voltage of 900 V
 643 and reduce the PMT anode current, therefore improving the rate capability.
 644 The energy bite of each counter ranges between 8.5 and 30 MeV for a 12 GeV
 645 incident electron beam. Typical rates during production running are 1 MHz
 646 above the coherent peak and 2 MHz per counter below the coherent peak. The
 647 maximum sustainable rate per counter is about 4 MHz.

648 The counters are mounted with their faces normal to the path of the scattered
 649 electrons in two or three rows slightly downstream of the focal plane, as shown
 650 in Fig. 10. This allows the counters to be positioned without horizontal gaps in
 651 the dispersion direction, enabling complete coverage of the entire tagged photon
 652 energy range.

653 The mounting frame of the hodoscope is suspended from the ceiling of the
 654 Tagger Hall to provide full flexibility for positioning TAGH. The frame is con-
 655 structed to also support the addition of counters to fill in the energy range
 656 currently occupied by the microscope when the TAGM location is changed.

657 A similar procedure to that described in Section 2.4.2 for the TAGM is used
 658 to apply a time-walk correction to the TDC times from the TAGH counters.
 659 Once this time-walk correction is applied, the time resolution of the TAGH is
 660 200 ps. No significant degradation of this resolution is expected at the operating
 661 rates planned for Phase 2 running, which are on the order of 2 MHz per counter
 662 above the coherent peak. Under these conditions, the rates in the TAGH coun-
 663 ters below the coherent peak would average around 4 Mhz, which is at the top
 664 of their allowed range. These counters will be turned off when running at full

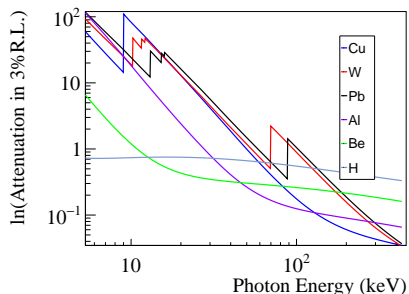


Figure 11: Attenuation of low-energy photons in foils with a thickness of 3% of a radiation length for different materials as a function of photon energy. The W foil was selected to reduce the random background hits in the detector drift chambers. The attenuation coefficients are taken from Ref. [20].

665 intensity.

666 2.5. Tungsten keV filter

667 To reduce the photon flux in the 10 – 100 keV range, a 100 μm tungsten
 668 foil (3% of a radiation length) was installed in the beam line at the entrance of
 669 the collimator cave. We have studied the effect of different foil materials on the
 670 anode currents and random hits in the drift chambers (see Section 5), as these
 671 factors limit the high-intensity operation of the experiment. By comparing the
 672 effect of different materials (Al, Cu, W) with fixed radiation lengths (see Fig.11)
 673 we learned that the drift chambers are mostly affected by photons in the 70-90
 674 keV range. The analysis of the pulse shape of the random hits in the CDC
 675 confirmed that these photons directly produce hits in the inner layers of the
 676 chamber. The insertion of the tungsten foil reduced the number of random hits
 677 in the inner CDC layers by a factor of up to 8 and the anode current by 55%.
 678 The reduction of the current in the FDC was more moderate, about 25%. Note
 679 that the FDC sense wires are as close as 3 cm to the beam, while in the CDC
 680 the closest wires are at 10 cm.

681 2.6. Beam profiler

682 The beam profiler is located immediately upstream of the collimator (see
 683 Fig. 4) and is used to measure the photon beam intensity in a plane normal to
 684 the incident photon beam. The profiler consists of two planes of scintillating
 685 fibers, giving information on the photon beam profile in the X and Y projections.
 686 Each plane consists of 64 square fibers, 2 mm in width, read out by four 16-
 687 channel multi-anode PMTs. The beam profiler is only used during beam setup
 688 until the photon beam is centered on the active collimator.

689 *2.7. Active collimator*

690 The active collimator monitors the photon beam position and provides feed-
691 back to micro-steering magnets in the electron beamline, for the purpose of
692 suppressing drifts in photon beam position. The design of the active collimator
693 for GLUEX is based on a device developed at SLAC for monitoring the coherent
694 bremsstrahlung beam there [21]. The GLUEX active collimator is located on
695 the upstream face of the primary collimator, and consists of a dense array of
696 tungsten pins attached to tungsten base plates. The tungsten plate intercepts
697 off-axis beam photons before they enter the collimator, creating an electromag-
698 netic shower that cascades through the array of pins. High-energy delta rays
699 created by the shower in the pins (known as “knock-ons”) are emitted forward
700 into the primary collimator. The resulting net current between the tungsten
701 plates and the collimator is proportional to the intensity of the photon beam on
702 the plate. The tungsten plates are mounted on an insulating support, and the
703 plate currents are monitored by a preamplifier with pA sensitivity.

704 The tungsten plate is segmented radially into two rings, and each ring is
705 segmented azimuthally into four quadrants. The asymmetry of the induced
706 currents on the plates in opposite quadrants indicates the degree of displace-
707 ment of the photon beam from the intended center position. Typical currents
708 on the tungsten sectors are at the level of 1.4 nA (inner ring) and 0.85 nA
709 (outer ring) when running with a 50 μm diamond crystal and a 200-nA incident
710 electron beam current. The current-sensitive preamplifiers used with the ac-
711 tive collimator are PMT-5R devices manufactured by ARI Corporation²⁶. The
712 PMT-5R has six remotely selectable gain settings ranging from 10^{12} V/A to
713 10^6 V/A, selectable by powers of 10. This provides an excellent dynamic range
714 for operation of the beam over a wide range of intensities, from 1 nA up to sev-
715 eral μA . The preamplifier input stage exhibits a fixed gain-bandwidth product
716 of about 2 Hz-V/pA which limits its bandwidth at the higher gain settings, for
717 example 2 Hz at 10^{12} V/A, 20 Hz at 10^{11} V/A.

718 In-situ electronic noise on the individual wedge currents is measured to be
719 $1.5 \text{ pA}/\sqrt{\text{Hz}}$ on the inner ring, and $15 \text{ pA}/\sqrt{\text{Hz}}$ on the outer ring. The sensi-
720 tivity of the current asymmetry to position is 0.160/mm for the inner ring and
721 0.089/mm for the outer. With a 50 micron diamond and 200 nA beam current,
722 operating the active collimator at a bandwidth of 1 kHz yields a measurement
723 error in the position of the beam centroid of 150 μm for the inner ring and
724 450 μm for the outer ring. The purpose of the outer ring is to help locate the
725 beam when the beam location has shifted more than 2 mm from the collimator
726 axis, where the response of the inner ring sectors becomes nonlinear.

727 The maximum deviation allowed for the Hall D photon beam position rela-
728 tive to the collimator axis is 200 μm . The active collimator readout was designed
729 with kHz bandwidth so that use in a fast feedback loop would suppress motion
730 of the beam at 60 Hz and harmonics that might exceed this limit. Experience
731 with the Hall-D beam has shown that the electron beam feedback system already

²⁶Advanced Research Instruments Corporation, <http://aricorp.com>.

732 suppresses this motion to less than 100 μm amplitude, so that fast feedback us-
733 ing the active collimator is not required during normal operation. Instead, the
734 active collimator is used in a slow feedback loop which locks the photon beam
735 position at the collimator with a correction time constant of a few seconds. This
736 slow feedback system is essential for preventing long-term drifts in the photon
737 beam position that would otherwise occur on the time scale of hours or days.
738 The active collimator can achieve 200 μm position resolution down to beam
739 currents as low as 2 nA when operated in this mode with noise averaging over
740 a 5 s interval.

741 *2.8. Collimator*

742 The photon beam produced at the diamond radiator contains both inco-
743 herent and coherent bremsstrahlung components. In the region of the coherent
744 peak, where photon polarization is at its maximum, the angular spread of coher-
745 ent bremsstrahlung photons is less than that of incoherent bremsstrahlung. The
746 characteristic emission angle for incoherent bremsstrahlung is $m/E = 43 \mu\text{rad}$
747 at 12 GeV, whereas the coherent flux within the primary peak is concentrated
748 below 15 μrad with respect to the beam direction. Collimation increases the
749 degree of linear polarization in the photon beam by suppressing the incoherent
750 component relative to the coherent part.

751 The Hall-D primary collimator provides apertures of 3.4 mm and 5.0 mm in a
752 tungsten block mounted on an X-Y table. The 5.0 mm collimator is used under
753 normal GLUEX running conditions. The tungsten collimator is surrounded by
754 lead shielding. The collimator may also be positioned to block the beam to
755 prevent high-intensity beam from entering the experimental hall during tuning
756 of the electron beam. Downstream of the primary collimator, a sweeping magnet
757 and shield wall, followed by a secondary collimator with its sweeping magnet
758 and shield wall, suppress charged particles and photon background around the
759 photon beam that are generated in the primary collimator. The photon beam
760 exiting the collimation system then passes through a thin pair conversion target.
761 The resulting e^+e^- pairs are used to continuously monitor the photon beam flux
762 and polarization.

763 *2.9. Triplet Polarimeter*

764 The Triplet Polarimeter (TPOL) is used to measure the degree of polariza-
765 tion of the linearly-polarized photon beam [22]. The polarimeter uses the process
766 of e^+e^- pair production on atomic electrons in a beryllium target foil, with the
767 scattered atomic electrons measured using a silicon strip detector. Information
768 on the degree of polarization of the photon beam is obtained by analyzing the
769 azimuthal distribution of the scattered atomic electrons.

770 *2.9.1. Determination of photon polarization*

771 Triplet photoproduction occurs when the polarized photon beam interacts
772 with the electric field of an atomic electron within a target material and pro-
773 duces a high energy e^+e^- pair. When coupled with trajectory and energy

774 information of the e^+e^- pair, the azimuthal angular distribution of the recoil
775 electron provides a measure of the photon beam polarization. The cross sec-
776 tion for triplet photoproduction can be written as $\sigma_t = \sigma_0[1 - P\Sigma \cos(2\varphi)]$ for
777 a polarized photon beam, where σ_0 is the unpolarized triplet cross section, P
778 the photon beam polarization, Σ the beam asymmetry for the process, and φ
779 the azimuthal angle of the recoil electron trajectory with respect to the plane
780 of polarization for the incident photon beam. To determine the photon beam
781 polarization, the azimuthal distribution of the recoil electrons is recorded and
782 fit to the function $A[1 - B \cos(2\varphi)]$ where the variables A and B are parameters
783 of the fit, with $B = P\Sigma$. The value of Σ depends on the beam photon energy,
784 the thickness of the converter target, and the geometry of the setup. The value
785 of Σ was determined to be 0.1990 ± 0.0008 at 9 GeV for the GLUEX beamline
786 and a 75 micron Be converter [22].

787 The TPOL detects the recoil electron arising from triplet photoproduction.
788 This system consists of a converter tray and positioning assembly, which holds
789 and positions a beryllium foil converter where the triplet photoproduction takes
790 place. A silicon strip detector (SSD) detects the recoil electron from triplet
791 photoproduction, providing energy and azimuthal angle information for that
792 particle. A vacuum housing, containing the pair production target and SSD,
793 supplies a vacuum environment minimizing multiple Coulomb scattering be-
794 tween target and SSD. Preamplifier and signal filtering electronics are placed
795 within a Faraday-cage housing.

796 The preamplifier enclosure is lined with a layer of copper foil to reduce
797 exterior electromagnetic signal interference. Signals from the downstream (az-
798 imuthal sector) side of the SSD are fed to a charge-sensitive preamplifier located
799 outside the vacuum. In operation, the TPOL vacuum box is coupled directly to
800 the evacuated beamline through which the polarized photon beam passes.

801 Upon entering TPOL, the photon beam passes into the beryllium converter,
802 triplet photoproduction takes place, an e^+e^- pair is emitted from the target
803 in the forward direction, and a recoil electron ejected from the target at large
804 angles with respect to the beam is detected by the SSD within the TPOL vacuum
805 chamber. The recoil electron is ejected at large angles and detected by the SSD.
806 The e^+e^- pair, together with any beam photons that did not interact with the
807 converter material, pass through the downstream port of the TPOL vacuum
808 box into the evacuated beamline, which in turn passes through a shielding wall
809 into the Hall-D experimental area. The e^+e^- pair then enters the vacuum box
810 and magnetic field of the GLUEX Pair Spectrometer, while photons continue
811 through an evacuated beamline to the target region of the GLUEX detector.
812 Accounting for all sources of uncertainty from this setup, the total estimated
813 systematic error in the TPOL asymmetry Σ is 1.5% [22].

814 *2.10. Pair Spectrometer*

815 The main purpose of the Pair Spectrometer (PS) [23] is to measure the
816 spectrum of the collimated photon beam and determine the fraction of linearly
817 polarized photons in the coherent peak energy region. The TPOL relies on the
818 PS to trigger on pairs in coincidence with hits in the recoil detector. The PS

819 is also used to monitor the photon beam flux, and for energy calibration of the
820 tagging hodoscope and microscope detectors.

821 The PS, located at the entrance to Hall D, reconstructs the energy of a
822 beam photon by detecting the e^+e^- pair produced by the photon in a thin
823 converter. The converter used is typically the beryllium target housed within
824 TPOL; otherwise the PS has additional converters that may be inserted into the
825 beam with thicknesses ranging between 0.03% and 0.5% of a radiation length.
826 The produced e^+e^- leptons are deflected in a modified 18D36 dipole magnet
827 with an effective field length of about 0.94 m and detected in two layers of
828 scintillator detectors: a high-granularity hodoscope and a set of coarse counters,
829 referred to as PS and PSC counters, respectively. The detectors are partitioned
830 into two identical arms positioned symmetrically on opposite sides of the photon
831 beam line. The PSC consists of sixteen scintillator counters, eight in each
832 detector arm. Each PSC counter is 4.4 cm wide and 2 cm thick in the direction
833 along the lepton trajectory and 6 cm high. Light from the PSC counters is
834 detected using Hamamatsu R6427-01 PMTs. The PS hodoscope consists of 145
835 rectangular tiles (1 mm and 2 mm wide) stacked together. Hamamatsu SiPMs
836 were chosen for readout of the PS counters [24, 25, 26].

837 Each detector arm covers an e^\pm momentum range between 3.0 GeV/c and
838 6.2 GeV/c, corresponding to reconstructed photon energies between 6 GeV and
839 12.4 GeV. The relatively large acceptance of the hodoscope enables energy de-
840 termination for photons with energies from below the coherent peak to the beam
841 endpoint energy near 12 GeV.

842 The pair energy resolution of the PS hodoscope is about 25 MeV. The time
843 resolution of the PSC counters is 120 ps, which allows coincidence measurements
844 between the tagging detectors and the PS within an electron beam bunch. Sig-
845 nals from the PS detector are delivered to the trigger system, as described in
846 Section 9. The typical rate of PS double-arm coincidences is a few kHz. Details
847 about the performance of the spectrometer are given in [27, 28].

848 *2.10.1. Determination of photon flux*

849 The intensity of beam photons incident on the GLUEX target is important for
850 the extraction of cross sections. The photon flux is determined by converting a
851 known fraction of the photon beam to e^\pm pairs and counting them in the PS as a
852 function of energy. Data from the PS are collected using a PS trigger, which runs
853 in parallel to the main GLUEX physics trigger, as described in Section 9. The
854 number of beam photons integrated over the run period is obtained individually
855 for each tagger counter (TAGH and TAGM), i.e., for each photon beam energy
856 bin.

857 The PS calibration parameter used in the flux determination, a product
858 of the converter thickness, acceptance, and the detection efficiency for lep-
859 tons, is determined using calibration runs with the Total Absorption Counter
860 (TAC) [29]. The TAC is a small calorimeter (see Section 2.11) inserted directly
861 into the photon beam immediately upstream of the photon beam dump to count
862 the number of beam photons as a function of energy. These absolute-flux cal-
863 ibration runs are performed at reduced beam intensities in order to limit the

864 rate of accidental tagging coincidences. Data are acquired simultaneously from
865 the PS and TAC. These data enable an absolute flux calibration for the PS
866 by measuring the number of reconstructed e^+e^- pairs for a given number of
867 photons of the same energy seen by the TAC. Uncertainties on the photon flux
868 determinations are currently being investigated. The expected precision of the
869 flux determination is on the level of 1%.

870 *2.11. Total Absorption Counter*

871 The TAC is a high-efficiency lead-glass calorimeter, used at low beam cur-
872 rents ($< 5\text{nA}$) to determine the overall normalization of the flux from the GLUEX
873 coherent bremsstrahlung facility. This device is intended to count all beam pho-
874 tons above a certain energy threshold, which have a matching hit in the tagger
875 system. There would be a very large number of overlapping pulses in the TAC
876 if it is used with the production photon flux, resulting in low detection effi-
877 ciency and therefore large systematic uncertainties. Therefore, the TAC is only
878 inserted into the beam during dedicated runs at very low intensities when the
879 detector can run with near 100% efficiency. The TAC was originally developed
880 for and deployed in Hall B, for photon beam operations with CLAS [30, 31, 32].

881 Only a certain fraction of the photons produced at the radiator reach the
882 target and causes an interaction that is seen in the GLUEX detector. The
883 count of tagged photons reaching the GLUEX target is determined as a function
884 of energy from individual TAC coincidence measurements with each tagging
885 counter. Simultaneous with these counts, the coincidences between each of the
886 tagging counters and converted pairs detected in the pair spectrometer are also
887 recorded. The ratio between the count of tagged pairs and tagged TAC events
888 thus determined for each tagging counter are used to convert the tagged rate
889 in the pair spectrometer that is observed during normal operation into a total
890 count of tagged photons for each tagging counter that were incident on the
891 GLUEX target.

892 **3. Solenoid magnet**

893 *3.1. Overview*

894 The core of the GLUEX spectrometer is a superconducting solenoid with a
895 bore diameter and overall yoke length of approximately 2 m and 4.8 m, respec-
896 tively. The photon beam passes along the axis of the solenoid. At the nominal
897 current of 1350 A, the magnet provides a magnetic field along the axis of about
898 2 T.

899 The magnet was designed and built at SLAC in the early 1970's [33] for the
900 LASS spectrometer [34]. The solenoid employs a cryostatically stable design
901 with cryostats designed to be opened and serviced with hand tools. The magnet
902 was refurbished and modified²⁷ for the GLUEX experiment [35, 36].

²⁷ The front plate of the flux return yoke was modified, leading to a swap of the two front

903 The magnet is constructed of four separate superconducting coils and cryo-
 904 stats. The flux return yoke is made of several iron rings. The coils are connected
 905 in series. A common liquid helium tank is located on top of the magnet, pro-
 906 viding a gravity feed of the liquid to the coils. The layout of the coil cryostats
 907 and the flux return iron yoke is shown in Fig. 3. Table 3 summarizes the salient
 908 parameters of the magnet.

Inside diameter of coils	2032 mm
Clear bore diameter	1854 mm
Overall length along iron	4795 mm
Inside iron diameter	2946 mm
Outside iron diameter	3759 mm
Original yoke, cast and annealed - steel	AISI 1010
Added filler plates - steel	ASTM A36
Full weight	284 t
Full number of turns	4608
Number of separate coils	4
Turns per coil 2	928
Turns per coil 1	1428
Turns per coil 3	776
Turns per coil 4	1476
Total conductor weight	13.15 t
Coil resistance at ~ 300 K	15.3 Ω
Coil resistance at ~ 10 K	~ 0.15 Ω
Design operational current	1500 A
Nominal current (actual)	1350 A
Maximal central field at 1350 A	2.08 T
Inductance at 1350 A	26.4 H
Stored energy at 1350 A	24.1 MJ
Protection circuit resistor	0.061 Ω
Coil cooling scheme	helium bath
Total liquid helium volume	3200 ℓ
Operating temperature (actual)	4.5 K
Refrigerator liquefaction rate at 0 A	1.7 g/s
Refrigerator liquefaction rate at 1350 A	2.7 g/s

Table 3: Key parameters of the GLUEx solenoid. The coils are listed in order along the beam direction.

909 3.2. Conductor and Coils

910 The superconductor composite is made of niobium–titanium filaments in a
 911 copper substrate, twisted and shaped into a $\sim 7.62 \times 1$ mm² rectangular band.

coils and modifications of the return flux yoke in order to keep the magnetic forces on the front coil under the design limit. The original gaps between the yoke’s rings were filled with iron. The Cryogenic Distribution Box was designed and built for GLUEx.

912 The laminated conductor is made by soldering the superconductor compos-
913 ite band between two copper strips to form a rectangular cross section of
914 $7.62 \times 5.33 \text{ mm}^2$. The measured residual resistivity ratio of the conductor at
915 $\sim 300\text{K}$ and $\sim 15\text{K}$ is ≈ 100 .

916 As the coil was wound, a 0.64 mm-thick stainless steel support band and
917 two 0.2 mm-thick Mylar insulating strips were wound together with it for pre-
918 tensioning and insulation. The liquid helium is in contact with the shorter
919 (5.33 mm) sides of the cable.

920 Each of the coils consists of a number of subcoils. Each subcoil contains
921 a number of “double pancakes” with the same number of turns. Each double
922 pancake is made from a single piece of conductor. The voltage across the subcoils
923 is monitored using special wires. These pass through vertical cryostats, called
924 chimneys, along with the helium supply pipes and the main conductor.

925 The cold helium vessel containing the coil is supported within the warm
926 cryostat vacuum vessel by a set of columns designed to provide sufficient thermal
927 insulation. The columns are equipped with strain gauges for monitoring the
928 stresses on the columns. The helium vessel is surrounded by a nitrogen-cooled
929 thermal shield made of copper and stainless-steel panels. Super-insulation is
930 placed between the vacuum vessel and the nitrogen shield. The vacuum vessels
931 are attached to the matching iron rings of the yoke.

932 The power supply²⁸ provides up to 10 V DC for establishing the operating
933 current while ramping. The supply also includes a protection circuit, which
934 can be engaged by a quench detector as well as by other signals. During trips,
935 a small dump resistor of 0.061Ω limits the maximum voltage on the magnet
936 to 100 V. The dumping time constant of $L/R \approx 7 \text{ min}$ is relatively long, but
937 safe according to the original design of the magnet. A large copper mass and
938 the helium bath are able to absorb a large amount of energy during a quench
939 without overheating the solder joints. This permits the use of an “intelligent”
940 quench detector with low noise sensitivity and a relatively slow decision time
941 of 0.5 s. The quench detector compares the measured voltages on different
942 subcoils in order to detect a resistive component. While ramping the current,
943 such a voltage is proportional to the subcoil inductance. Relative values of
944 inductance of various subcoils depend on the value of the current because of
945 saturation effects in the iron yoke. Transient effects are also present at changes
946 of the slew rate caused by Foucault currents in the yoke. The system includes
947 two redundant detectors: one uses analog signals and a simplified logic, another
948 is part of the PLC control system (see Section 3.4) which uses digitized signals.
949 The PLC digital programmable device is more sensitive since this monitoring
950 system takes into account the dependence of the coils’ inductance on the current
951 and provides better noise filtering. The ramping slew rate is limited by the
952 transient imbalance of the voltages on subcoils that may trigger the quench
953 detector. Additionally, unexplained voltage spikes of 1 ms duration have been
954 observed in coil 2 at high slew rates, which can trigger the quench detector.

²⁸Danfysik System 8000 Type 854.

955 Powering up the magnet to 1350 A takes about 8 h.

956 For diagnostic purposes two 40-turn pickup coils are installed on the bore
957 surface of the vacuum vessel of each of the coils.

958 *3.3. Cooling System*

959 The cooling system is described in detail in Ref. [37]. A stand-alone helium
960 refrigerator located in a building adjacent to Hall D provides liquid helium and
961 nitrogen via a transfer line to the Cryogenic Distribution Box above the magnet.
962 The transfer line delivers helium at 2.6 atm, and 6 K to a Joule-Thomson (JT)
963 valve providing liquid to a cylindrical common helium tank in the Distribution
964 Box. The level of liquid helium in the tank is measured with a superconducting
965 wire probe;²⁹ the liquid level is kept at about half of the tank diameter. The
966 cold helium gas from the tank is returned to the refrigerator, which keeps the
967 pressure at the top of the tank at 1.2 atm corresponding to about 4.35 K at
968 the surface of the liquid.³⁰ Each coil is connected to the common helium tank
969 by two vertical 2-inch pipes. One pipe is open at the bottom of the tank while
970 the other one is taller than the typical level of helium inside the tank. The
971 main conductor and the wires for voltage monitoring pass through the former
972 pipe. Additionally, two ~ 6 m long, 3/8 inch ID pipes go outside the coil's
973 helium vessel, from the Distribution Box to the bottom of the coil. One of those
974 pipes, connected to a JT valve in the box, is used to fill the coil initially, but is
975 not used during operation. The other pipe reaches the bottom of the common
976 helium tank in order to provide a thermo-syphon effect essential for the proper
977 circulation of helium in the coil. The main current is delivered into the helium
978 tank via vapor-cooled leads, and is distributed to the coils by a superconducting
979 cable. After cooling the leads, the helium gas is warmed and returned to the
980 refrigeration system. The gas flow through the leads is regulated based on the
981 current in the magnet; at 1350 A, the flow is about 0.25 g/s. The coils and the
982 Distribution Box are equipped with various sensors for temperature, pressure,
983 voltage, and flow rates.

984 *3.4. Measurements and Controls*

985 The control system for the superconducting solenoid, power supply, and
986 cryogenic system, is based on Programmable Logic Controllers (PLC)³¹. The
987 PLC system digitizes the signals from various sensors, communicates with other
988 devices, reads out the data into a programmable unit for analysis, and sends
989 commands to various devices. Additionally, the PLC is connected to EPICS³²
990 in order to display and archive the data (see Section 11). The practical sampling
991 limit for the readout of the sensor is a few Hz, which is too low for detection of

²⁹ American Magnetics Model 1700 with HS-1/4-RGD-19"/46"-4LDCP-LL6-S sensor

³⁰ The original implementation at SLAC did not recycle the helium and operated at atmospheric pressure.

³¹ Allen-Bradley Programmable Logic Controllers <http://ab.rockwellautomation.com/Programmable-Controllers>.

³² Experimental Physics and Industrial Control System, <https://epics.anl.gov>.

992 fast voltage spikes on the coils due to motion, shorts, or other effects. Therefore,
993 the voltage taps from the coils and the pickup coils are read out by a PXI
994 system³³, which provides a sampling rate of about 100 kHz. The PXI system
995 also reads out several accelerometers attached to the coils' chimneys, which can
996 detect motion inside the coils. The PXI CPU performs initial integration and
997 arranges the data in time-wise rows with a sampling rate of 10 kHz. The PLC
998 system reads out the data from the PXI system. Additionally, the PXI data are
999 read out by an EPICS server at the full 10 kHz sampling rate and are recorded
1000 for further analysis.

1001 3.5. Field calculation and measurement

1002 The momentum resolution of the GLUEX spectrometer is larger than 1%
1003 and is dominated by multiple scattering and the spatial resolution of the coordi-
1004 nate detectors. Thus, a fraction of a percent is sufficient accuracy for the field
1005 determination. The coils are axially symmetric, while the flux return yoke is
1006 nearly axially symmetric, apart from the holes for the chimneys. The field was
1007 calculated using a 2-dimensional field calculator *Poisson/Superfish*³⁴, assuming
1008 axial symmetry. The model of the magnet included the fine structure of the
1009 subcoils and the geometry of the yoke iron. Different assumptions about the
1010 magnetic properties of the yoke iron have been used: the *Poisson* default AISI
1011 1010 steel, the measurements of the original yoke iron made at SLAC, and the
1012 1018 steel used for the filler plates. Since the results of the field calculations
1013 differ by less than 0.1%, the default *Poisson* AISI 1010 steel properties were
1014 used for the whole yoke iron in the final field map calculations.

1015 The three projections of the magnetic field have been measured along lines
1016 parallel to the axis, at four values of the radius and at up to six values of
1017 the azimuthal angle. The calculated field and the measured deviations are
1018 shown in Fig. 12. The tracking detectors occupy the volume of $R < 56$ cm
1019 and $45 < Z < 340$ cm. In this volume the field deviation at $R = 0$ does not
1020 exceed 0.2%. The largest deviation of 1.5% is observed at the downstream edge
1021 of the fiducial volume and at the largest radius. Such a field uncertainty in
1022 that region does not noticeably affect the momentum resolution. In most of the
1023 fiducial volume the measured field is axially symmetric to $\approx 0.1\%$ and deviates
1024 from this symmetry by $\approx 2\%$ at the downstream edge and the largest radius.

1025 The calculated field map is used for track reconstruction and physics analy-
1026 ses.

1027 4. Target

1028 A schematic diagram of the GLUEX liquid hydrogen cryotarget is shown in
1029 Fig. 13. The major components of the system are a pulse tube cryocooler,³⁵

³³ National Instruments, PXI Platform, <http://www.ni.com/pxi/>.

³⁴ Poisson/Superfish developed at LANL, https://laacg.lanl.gov/laacg/services/serv_codes.phtml#ps.

³⁵ Cryomech model PT415.

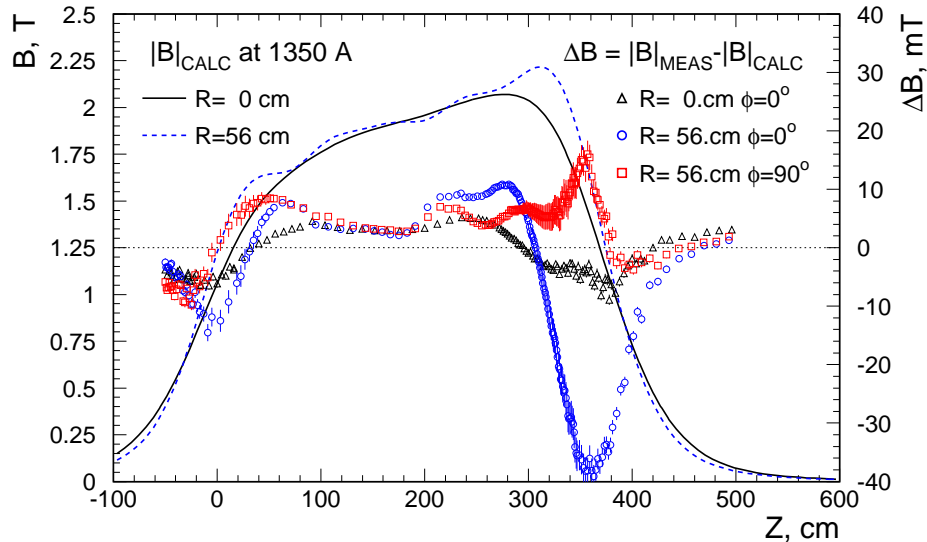


Figure 12: The full field at 1350 A calculated with *Poisson* (left scale) on the axis and at the edge of the tracking fiducial volume ($R=56$ cm). The deviations of the measurements from the calculations are shown (right scale) on the axis, and at $R=56$ cm. The measurements were made at 6 azimuthal angles. We show the angles (0° and 90°) with the largest deviations from the calculations.

1030 a condenser, and a target cell. These items are contained within an aluminum
 1031 and stainless steel ‘L’-shaped vacuum chamber with an extension of closed-cell
 1032 foam³⁶ surrounding the target cell. In turn, the GLUEX Start Counter (Sec. 8.1)
 1033 surrounds the foam chamber and is supported by the horizontal portion of the
 1034 vacuum chamber. Polyimide foils, 100 μm thick, are used at the upstream and
 1035 downstream ends of the chamber as beam entrance and exit windows. The
 1036 entire system, including the control electronics, vacuum pumps, gas-handling
 1037 system, and tanks for hydrogen storage, is mounted on a small cart that is
 1038 attached to a set of rails for insertion into the GLUEX solenoid. To satisfy
 1039 flammable gas safety requirements, the system is connected at multiple points
 1040 to a nitrogen-purged ventilation pipe that extends outside Hall D.

1041 Hydrogen gas is stored inside two 200 l tanks and is cooled and condensed
 1042 into a small copper and stainless steel container, the condenser, that is thermally
 1043 anchored to the second cooling stage of the cryocooler. The first stage of the
 1044 cryocooler is used to cool the H_2 gas to about 50 K before it enters the condenser.
 1045 The first stage also cools a copper thermal shield that surrounds all lower-
 1046 temperature components of the system except for the target cell itself, which is
 1047 wrapped in a few layers of aluminized-mylar/cerex insulation.

³⁶Rohacell 110XT, Evonik Industries AG.

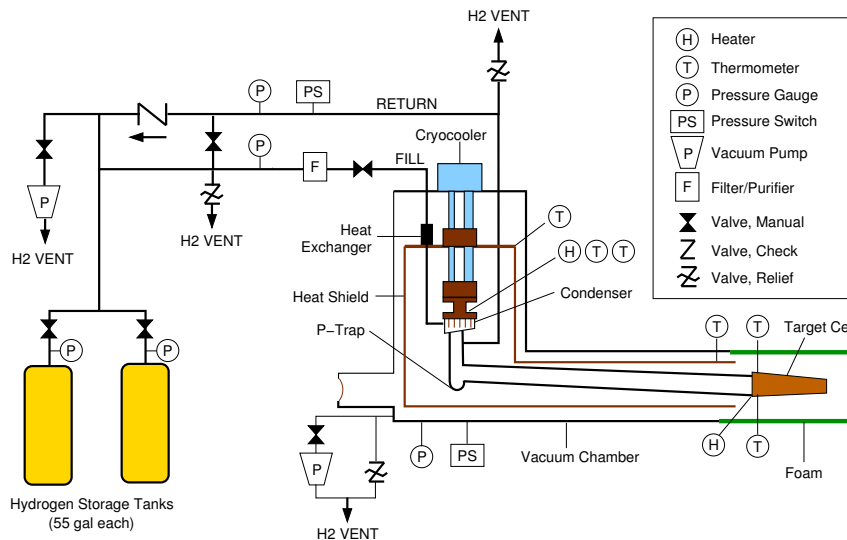


Figure 13: Simplified process and instrumentation diagram for the GlueX liquid hydrogen target (not to scale). In the real system, the P-trap is above the level of the target cell and is used to promote convective cooling of the target cell from room temperature.

1048 The condenser is comprised of a copper C101 base sealed to a stainless steel
 1049 can with an indium O-ring. Numerous vertical fins are cut into the copper base,
 1050 giving a large surface area for condensing hydrogen gas. A heater and a pair of
 1051 calibrated Cernox thermometers³⁷ are attached outside the condenser, and are
 1052 used to regulate the heater temperature when the system is filled with liquid
 1053 hydrogen.

1054 The target cell, shown in Fig. 14, is similar to designs used in Hall B at
 1055 JLab [38]. The cell walls are made from 100- μm -thick aluminized polyimide
 1056 sheet wrapped in a conical shape and glued along the edge, overlapping into
 1057 a 2 mm wide scarf joint. The conical shape prevents bubbles from collecting
 1058 inside the cell, while the scarf joint reduces the stress riser at the glue joint.
 1059 This conical tube is glued to an aluminum base, along with stainless steel fill
 1060 and return tubes leading to the condenser, a feed-through for two calibrated
 1061 Cernox thermometers inside the cell, and a polyamide-imide support for the
 1062 reentrant upstream beam window. Both the upstream and downstream beam
 1063 windows are made of non-aluminized, 100 μm thick polyimide films that have
 1064 been extruded into the shapes indicated in Fig. 14. These windows are clearly
 1065 visible in Fig. 21 where reconstructed vertex positions are shown. All items are
 1066 glued together using a two-part epoxy³⁸ that has been in reliable use at cryogenic

³⁷Cernox, Lake Shore Cryotronics.

³⁸3M Scotch-Weld epoxy adhesive DP190 Gray.

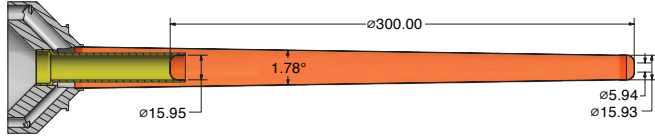


Figure 14: Target cell for the liquid hydrogen target. Dimensions are in mm.

1067 temperatures for long periods. A second heater, attached to the aluminum base,
 1068 is used to empty the cell for background measurements. The base is attached
 1069 to a kinematic mount, which is in turn supported inside the vacuum chamber
 1070 using a system of carbon fiber rods. The mount is used to correct the pitch
 1071 and yaw of the cell, while X , Y , and Z adjustments are accomplished using
 1072 positioning screws on the target cart.

1073 During normal operation, a sufficient amount of hydrogen gas is condensed
 1074 from the storage tanks until the target cell, condenser, and interconnecting
 1075 piping are filled with liquid hydrogen and an equilibrium pressure of about
 1076 19 psia is achieved. The condenser temperature is regulated at 18 K, while
 1077 the liquid in the cell cools to about 20.1 K. The latter temperature is 1 K
 1078 below the saturation temperature of H_2 , which eliminates boiling within the
 1079 cell and permits a more accurate determination of the fluid density, $71.2 \pm$
 1080 0.3 mg/cm^3 . The system can be cooled from room temperature and filled with
 1081 liquid hydrogen in approximately six hours. Prior to measurements using an
 1082 empty target cell, the liquid hydrogen is boiled back into the storage tanks in
 1083 about five minutes. H_2 gas continues to condense and drain towards the target
 1084 cell, but the condensed hydrogen is immediately evaporated by the cell heater.
 1085 In this way, the cell does not warm above 40 K and can be re-filled with liquid
 1086 hydrogen in about twenty minutes.

1087 Operation of the cryotarget is highly automated, requires minimal user inter-
 1088 vention, and has operated in a very reliable and predictable manner throughout
 1089 the experiment. The target controls³⁹ are handled by a LabVIEW program,
 1090 while a standard EPICS softIOC running in Linux provides a bridge between
 1091 the controller and JLab's EPICS environment (see Section 11). Temperature
 1092 readback and control of the condenser and target cell thermometers are man-
 1093 aged by a four-input temperature controller⁴⁰ with PID control loops of 50 and
 1094 100 W. Strain gauge pressure sensors measure the fill and return pressures with
 1095 0.25% accuracy. When filled with subcooled liquid, the long-term tempera-
 1096 ture ($\pm 0.2 \text{ K}$) and pressure ($\pm 0.1 \text{ psi}$) stability of the liquid hydrogen enable a
 1097 determination of the density to better than 0.5%.

³⁹The control logic uses National Instruments CompactRIO 9030.

⁴⁰Lake Shore Model 336.

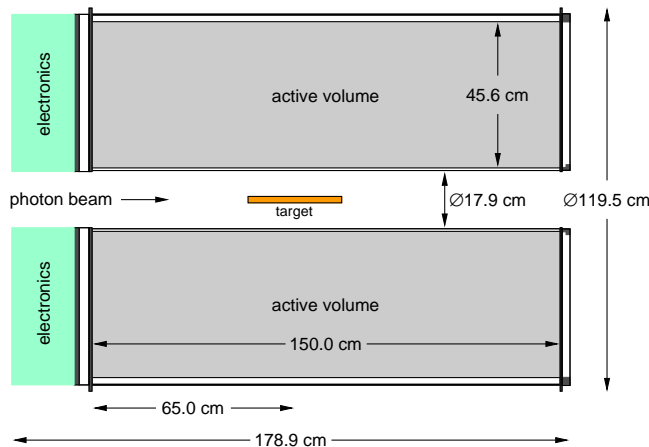


Figure 15: Cross-section through the cylindrically symmetric Central Drift Chamber, along the beamline.

1098 5. Tracking detectors

1099 5.1. Central drift chamber

1100 The Central Drift Chamber (CDC) is a cylindrical straw-tube drift chamber
 1101 which is used to track charged particles by providing position, timing and energy
 1102 loss measurements [39, 40]. The CDC is situated inside the Barrel Calorimeter,
 1103 surrounding the target and Start Counter. The active volume of the CDC
 1104 is traversed by particles coming from the hydrogen target with polar angles
 1105 between 6° and 168° , with optimum coverage for polar angles between 29°
 1106 and 132° . The CDC contains 3522 anode wires of $20\ \mu\text{m}$ diameter gold-plated
 1107 tungsten inside Mylar⁴¹ straw tubes of diameter 1.6 cm in 28 layers, located in
 1108 a cylindrical volume which is 1.5 m long, with an inner radius of 10 cm and
 1109 outer radius of 56 cm, as measured from the beamline. Readout is from the
 1110 upstream end. Fig. 15 shows a schematic diagram of the detector.

1111 The straw tubes are arranged in 28 layers; 12 layers are axial, and 16 layers
 1112 are at stereo angles of $\pm 6^\circ$ to provide position information along the beam
 1113 direction. The stereo angle was chosen to balance the extra tracking information
 1114 provided by the unique combination of stereo and axial straws along a trajectory
 1115 against the size of the unused volume inside the chamber at each transition
 1116 between stereo and axial layers. Fig. 16 shows the CDC during construction.

1117 The volume surrounding the straws is enclosed by an inner cylindrical wall
 1118 of 0.5 mm G10 fiberglass, an outer cylindrical wall of 1.6 mm aluminum, and
 1119 two circular endplates. The upstream endplate is made of aluminum, while the
 1120 downstream endplate is made of carbon fiber. The endplates are connected by 12

⁴¹www.mylar.com



Figure 16: The Central Drift Chamber during construction. A partially completed layer of stereo straw tubes is shown, surrounding a layer of straw tubes at the opposite stereo angle. Part of the carbon fiber endplate, two temporary tension rods and some of the 12 permanent support rods linking the two endplates can also be seen.

1121 aluminum support rods. Holes milled through the endplates support the ends of
1122 the straw tubes, which were glued into place using several small components per
1123 tube, described more fully in [40]. These components also support the anode
1124 wires, which were installed with 30 g tension. At the upstream end, these
1125 components are made of aluminum and were glued in place using conductive
1126 epoxy⁴². This attachment method provides a good electrical connection to the
1127 inside walls of the straw tubes, which are coated in aluminum. The components
1128 at the downstream end are made of Noryl plastic⁴³ and were glued in place using
1129 conventional non-conductive epoxy⁴⁴. The materials used for the downstream
1130 end were chosen to be as lightweight as feasible so as to minimize the energy
1131 loss of charged particles passing through them.

1132 At each end of the chamber, a cylindrical gas plenum is located outside the
1133 endplate. The gas supply runs in 12 tubes through the volume surrounding the
1134 straws into the downstream plenum. There the gas enters the straws and flows
1135 through them into the upstream plenum. From the upstream plenum the gas
1136 flows into the volume surrounding the straws, and from there the gas exhausts
1137 to the outside, bubbling through small jars of mineral oil. The gas mixture
1138 used is 50% argon and 50% carbon dioxide at atmospheric pressure. This gas
1139 mixture was chosen since its drift time characteristics provide good position

⁴²TIGA 920-H, www.loctite.com

⁴³www.sabic.com

⁴⁴3M Scotch-Weld DP460NS, www.3m.com

1140 resolution [39]. A small admixture (approximately 1%) of isopropanol is used
1141 to prevent loss of performance due to aging[41, 42]. Five thermocouples are
1142 located in each plenum and used to monitor the temperature of the gas. The
1143 downstream plenum is 2.54 cm deep, with a sidewall of ROHACELL⁴⁵ and a
1144 final outer wall of aluminized Mylar film, and the upstream plenum is 3.18 cm
1145 deep, with a polycarbonate sidewall and a polycarbonate disc outer wall.

1146 The readout cables pass through the polycarbonate disc and the upstream
1147 plenum to reach the anode wires. The cables are connected in groups of 20 to 24
1148 to transition boards mounted onto the polycarbonate disc; the disc also supports
1149 the connectors for the high-voltage boards. Preamplifiers [43] are mounted
1150 on the high-voltage boards. The aluminum endplate, outer cylindrical wall of
1151 the chamber, aluminum components connecting the straws to the aluminum
1152 endplate and the inside walls of the straws are all connected to a common
1153 electrical ground. The anode wires are held at +2.1 kV during normal operation.

1154 *5.2. Forward Drift Chamber*

1155 The Forward Drift Chamber (FDC) consists of 24 disc-shaped planar drift
1156 chambers of 1 m diameter [44]. They are grouped into four packages inside
1157 the bore of the spectrometer magnet. Forward tracking requires good multi-
1158 track separation due to the high particle density in the forward region. This is
1159 achieved via additional cathode strips on both sides of the wire plane allowing
1160 for a reconstruction of a space point on the track from each chamber. The FDC
1161 registers particles emitted into polar angles as low as 1° and up to 10° with all
1162 the chambers, while having partial coverage up to 20° .

1163 One FDC chamber consists of a wire plane with cathode planes on either
1164 sides at a distance of 5 mm from the wires (Fig. 17). The frame that holds the
1165 wires is made out of ROHACELL with a thin G10 fiberglass skin in order to
1166 minimize the material and allow low energy photons to be detected in the outer
1167 electromagnetic calorimeters.

1168 The wire plane has sense ($20\ \mu\text{m}$ diameter) and field ($80\ \mu\text{m}$) wires 5 mm
1169 apart, forming a field cell of $10 \times 10\ \text{mm}^2$. To reduce the effects of the magnetic
1170 field, a “slow” gas mixture of 40% Ar and 60% CO_2 is used. A positive high
1171 voltage of about 2.2 kV is applied to the sense wires and a negative high voltage
1172 of 0.5 kV to the field wires. The cathodes are made out of $2\text{-}\mu\text{m}$ -thin copper
1173 strips on Kapton foil with a pitch of 5 mm, and are held at ground potential.
1174 The strips on the two cathodes are arranged at 30° relative to each other and
1175 at angles of 75° and 105° angle with respect to the wires.

1176 The six chambers of a package are separated by thin aluminized Mylar. Each
1177 chamber is rotated relative to the previous one by 60° . The total material of a
1178 package in the sensitive area corresponds to 0.43% radiation lengths, with about
1179 half of that in the area along the beam line that has no copper on the cathodes.
1180 The sense wires in the inner area of 6 – 7.8 cm diameter (depending on the
1181 distance of the package to the target) are increased in thickness from $20\ \mu\text{m}$

⁴⁵www.rohacell.com

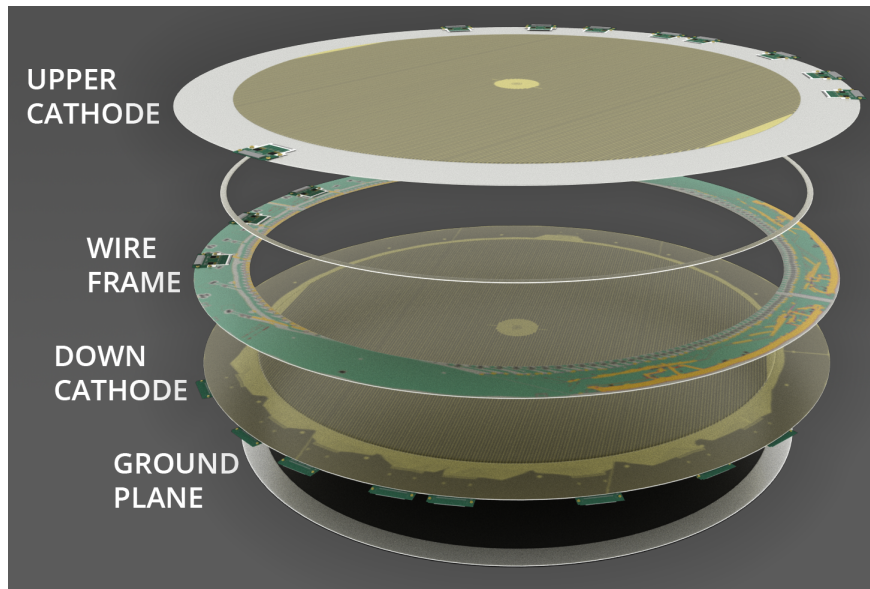


Figure 17: Artist rendering of one FDC chamber showing components. From top to bottom: upstream cathode, wire frame, downstream cathode, ground plane that separates the chambers. The diameter of the active area is 1 m.

1182 to $\sim 80 \mu\text{m}$, which makes them insensitive to the high rates along the beam.
 1183 The distance between the first and last package is 1.69 m. All chambers are
 1184 supplied with gas in parallel. In total, 2,304 wires and 10,368 strips are read
 1185 using charge preamplifiers with 10 ns peaking time, with a gain of 0.77 mV/fC
 1186 for the wires and 2.6 mV/fC for the strips.

1187 5.3. Electronics

1188 The high voltage (HV) supply units used are CAEN A1550P⁴⁶, with noise-
 1189 reducing filter modules added to each crate chassis. The low voltage (LV) sup-
 1190 plies are Wiener MPOD MPV8008⁴⁷. The preamplifiers are a custom JLab
 1191 design based on an ASIC [43] with 24 channels per board; the preamplifiers are
 1192 charge-sensitive, capacitively coupled to the wires in the CDC and FDC, and
 1193 directly coupled to strips in the FDC.

1194 Pulse information from the CDC anode wires and FDC cathode strips are
 1195 obtained and read out using 72-channel 125 MHz flash ADCs (FADCs) [45, 46].
 1196 These use Xilinx⁴⁸ Spartan-6 FPGAs (XC6SLX25) for signal digitization and
 1197 data processing with 12 bit resolution. Each FADC receives signals from three

⁴⁶www.caen.it

⁴⁷www.wiener-d.com

⁴⁸www.xilinx.com

1198 preamplifiers. The signal cables from different regions of the drift chambers are
1199 distributed between the FADCs in order to share out the processing load as
1200 evenly as possible.

1201 The FADC firmware is activated by a signal from the GLUEx trigger. The
1202 firmware then computes the following quantities for pulses observed above a
1203 given threshold within a given time window: pulse number, arrival time, pulse
1204 height, pulse integral, pedestal level preceding the pulse, and a quality factor
1205 indicating the accuracy of the computed arrival time. Signal filtering and inter-
1206 polation are used to obtain the arrival time to the nearest 0.8 ns. The firmware
1207 performs these calculations both for the CDC and FDC alike, and uses different
1208 readout modes to provide the data with the precision required by the separate
1209 detectors. For example, the CDC electronics read out only one pulse but require
1210 both pulse height and integral, while the FDC electronics read out up to four
1211 pulses and do not require a pulse integral.

1212 The FDC anode wires are read out using the JLab pipeline F1 TDC[47] with
1213 a nominal least count of 120 ps.

1214 *5.4. Gas system*

1215 Both the CDC and FDC operate with the same gases, argon and CO₂. Since
1216 the relative mixture of the two gases is slightly different for the two tracking
1217 chambers, the gas system has two separate but identical mixing stations. There
1218 is one gas supply of argon and CO₂ for both mixing stations. A limiting opening
1219 in the supply lines provides over-pressure protection to the gas system, and
1220 filters in the gas lines provide protection against potential pollution of the gas
1221 from the supply. Both gases are mixed using mass flow controllers (MFCs) that
1222 can be configured to provide the desired mixing ratio of argon and CO₂. MFCs
1223 and control electronics from BROOKS Instruments⁴⁹ are used throughout.

1224 The mixed gas is filled into storage tanks, with one tank for the CDC and
1225 another for the FDC. The pressures are regulated by controlling the operation of
1226 the MFCs with a logic circuit based on an Allen-Bradley ControlLogix system⁵⁰
1227 that keeps the pressure in the tank between 10 and 12 psi. The tank serves both
1228 as a reservoir and a buffer. A safety relief valve on each tank provides additional
1229 protection against over-pressure. While the input pressure to the MFC is at
1230 40 psi, the pressure after the MFC is designed to always be less than 14 psi
1231 above atmospheric pressure. After the mixing tank, a provision is built into the
1232 system to allow the gas to pass through an alcohol bath to add a small amount
1233 of alcohol gas to the gas mixture. This small admixture of alcohol protects the
1234 wire chambers from aging effects caused by radiation exposure from the beam.
1235 This part of the gas system is located above ground in a separate gas shed,
1236 before the gas mixture is transported to the experimental hall via polyethylene
1237 pipes.

⁴⁹BROOKS Instruments, <https://www.brooksinstrument.com/en/products/mass-flow-controllers>.

⁵⁰Allen-Bradley, <https://ab.rockwellautomation.com/>

1238 Additional MFCs in the hall allow the exact amount of gas provided to the
1239 chambers to be specified: one MFC for the CDC and another four MFCs for the
1240 individual FDC packages. The CDC is operated with a flow of 1.0 l/m, while
1241 each FDC package is operated with a flow of 0.1 l/m. To protect the chambers
1242 from over-pressure, there is a bypass line at the input to the detectors that is
1243 open to the atmosphere following a bubbler containing mineral oil. The height
1244 of the oil level determines the maximum possible gas pressure at the input to the
1245 chambers. There is a second bubbler at the output to protect against possible
1246 air back-flow into the chamber. The height of the oil above the exhaust line
1247 determines the operating pressure inside the chambers.

1248 Valves are mounted at many locations in the gas system to monitor various
1249 pressures with a single pressure sensor. The pressures of all six FDC chambers
1250 are monitored, as well as the CDC gas at the input, downstream gas plenum
1251 and the exhaust. A valve in the exhaust line can be used to divert some gas
1252 from the chamber to an oxygen sensor. Trace quantities of oxygen will reduce
1253 the gas gain and reduce tracking efficiency. The oxygen levels in the chamber
1254 are below 100 ppm.

1255 *5.5. Calibration, performance and monitoring*

1256 Time calibrations for the drift chambers are used to remove the time offset
1257 due to the electronics, so that after calibration the earliest possible arrival time
1258 of the pulse signals is at 0 ns. These offsets and the function parameters used to
1259 describe the relationship between the pulse arrival time and the closest distance
1260 between the track and the anode wire are obtained for each session of data
1261 taking.

1262 The CDC measures the energy loss, dE/dx , of tracks over a wide range of
1263 polar angles, including recoiling target protons as well as more forward-going
1264 tracks. Gain calibrations are made to ensure that dE/dx is consistent between
1265 tracking paths through different straws and stable over time. The procedure
1266 entails matching the position of the minimum ionizing peak for each of the 3522
1267 straws, and then matching the dE/dx at 1.5 GeV/c to the calculated value of
1268 2.0 keV/cm. This takes place during the early stages of data analysis. Gain
1269 calibration for the individual wires is performed each time the HV is switched
1270 on and whenever any electronics modules are replaced. Gain calibration for the
1271 chamber as a whole is performed for each session of data taking; these sessions
1272 are limited to two hours as the gain is very sensitive to the atmospheric pressure.
1273 Position calibrations were necessary to describe the small deflection of the straw
1274 tubes midway along their length; these were performed in 2016 and repeated
1275 in 2017, with no significant difference found between the two sets of results.
1276 Position resolution from the CDC is of the order of 130 μm and its detection
1277 efficiency per straw is over 98% for tracks up to 4 mm from the CDC wire. The
1278 efficiency decreases as the distance between the track and the wire increases,
1279 but the close-packing arrangement of the straw tubes and the large number of
1280 straws traversed by each track compensate for this.

1281 For the FDC system, an internal per-chamber calibration process is first
1282 performed to optimize the track position accuracy. In the FDC the avalanche

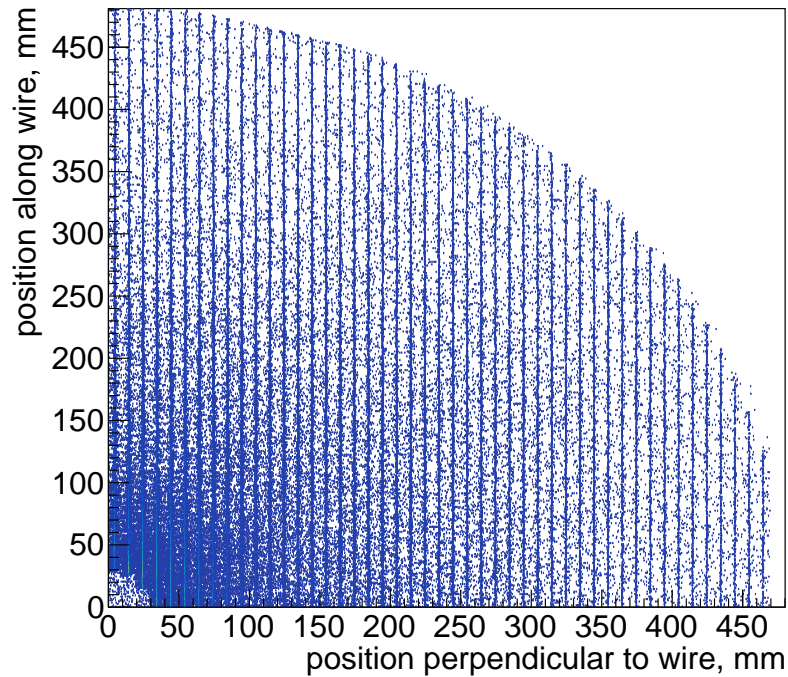


Figure 18: Wire (avalanche) positions reconstructed from the strip information on the two cathodes in one FDC chamber. Only one quarter of the chamber is shown in this figure.

1283 created around the wire is seen in three projections: on the two cathodes and on
 1284 the wires. The drift time information from the wires is used to reconstruct the
 1285 hit position perpendicular to the wire. The strip charges from the two cathodes
 1286 are used to reconstruct the avalanche position along the wire. The same strip
 1287 information can be used to reconstruct the avalanche position perpendicular to
 1288 the wire, which, due to the proximity of the avalanche to the wire, is practically
 1289 the wire position, as illustrated in Fig 18. This strip information is used to
 1290 align the strips on the two cathodes with respect to the wires. At the same
 1291 time, the residuals of the reconstructed wire positions are an estimate of the
 1292 strip resolution. The resolutions of the detector were reported earlier [44]. The
 1293 strip resolution along the wires, estimated from the wire position reconstruction,
 1294 varies between 180 and 80 μm , depending on the total charge induced on the
 1295 strips. The drift distance is reconstructed from the drift time with a resolution
 1296 between 240 and 140 μm depending on the distance of the hit to the wire in the
 1297 0.5 – 4.5 mm range.

1298 Position offsets and package rotations were determined for both drift cham-
 1299 ber systems, first independently, and then together, using the alignment software

1300 MILLEPEDE[48] in a process described in [40] and in [49].

1301 Online monitoring software enables shift-takers to check that the number of
1302 channels recording data, the distribution of signal arrival times, and the dE/dx
1303 distribution are as expected.

1304 6. Performance of the charged-particle-tracking system

1305 6.1. Track reconstruction

1306 The first stage in track reconstruction is pattern recognition. Hits in adjacent
1307 layers in the FDC in each package are formed into track segments that are linked
1308 together with other segments in other packages to form FDC track candidates
1309 using a helical model for the track parameters. Hits in adjacent rings in the axial
1310 layers of the CDC are also associated into segments that are linked together with
1311 other segments in other axial layers and fitted with circles in the projection
1312 perpendicular to the beam line. Intersections between these circles and the
1313 stereo wires are found and a linear fit is performed to find a z -position near the
1314 beamline and the tangent to the dip angle $\lambda = \pi/2 - \theta$. These parameters, in
1315 addition to the circle fit parameters, form a CDC track candidate for each set
1316 of linked axial and stereo layers. Candidates that emerge from the target, and
1317 pass through both FDC and CDC in the $5^\circ - 20^\circ$ range, are linked together.

1318 The second stage uses a Kalman filter [50, 51] to find the fitted track param-
1319 eters $\{z, D, \phi, \tan \lambda, q/p_T\}$ at the position of closest approach of the track to the
1320 beam line. The track candidate parameters are used as an initial guess, where
1321 D is the signed distance of closest approach to the beam line. The Kalman filter
1322 proceeds in steps from the hits farthest from the beam line toward the beam
1323 line. Energy loss and multiple scattering are taken into account at each step
1324 along the way, according to a map of the magnetic field within the bore of the
1325 solenoid magnet. For the initial pass of the filter, the drift time information
1326 from the wires is not used. Each particle is assumed to be a pion, except for low
1327 momentum track candidates ($p < 0.8$ GeV/ c), for which the fits are performed
1328 with a proton hypothesis.

1329 The third stage matches each fitted track from the second stage to either the
1330 Start Counter, the Time-of-Flight scintillators, the Barrel Calorimeter, or the
1331 Forward Calorimeter to determine a start time t_0 so that the drift time to each
1332 wire associated with the track could be used in the fit. Each track is refitted
1333 with the drift information, separately for each value of mass for particles in the
1334 set $\{e^\pm, \pi^\pm, K^\pm, p^\pm\}$.

1335 6.2. Momentum and vertex resolution

1336 The momentum resolution as a function of angle and magnitude for pions
1337 and protons is shown in Fig. 19. The angular resolution is shown in Fig. 20.

1338 The thin windows of the cryogenic target and the exit window of the tar-
1339 get vacuum chamber provide a means to estimate the vertex resolution of the
1340 tracking system. Pairs of tracks from empty target measurements are used to

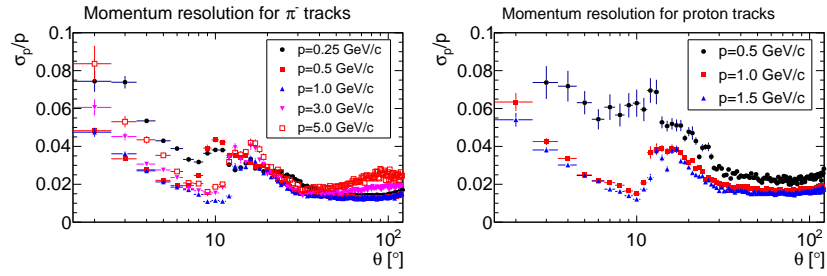


Figure 19: (Left) Momentum resolution for π^- tracks. (Right) Momentum resolution for proton tracks.

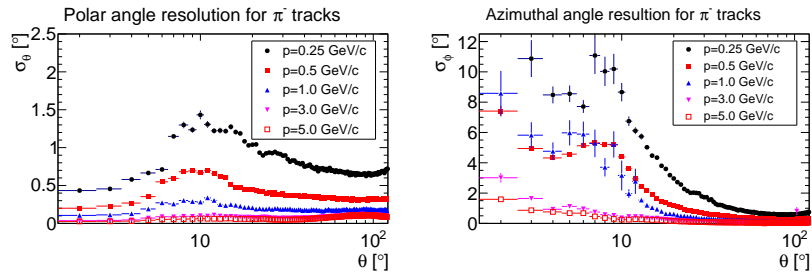


Figure 20: (Left) Polar angle resolution for π^- tracks. (Right) Azimuthal angle resolution for π^- tracks. The resolutions are plotted as a function of the polar angle, θ .

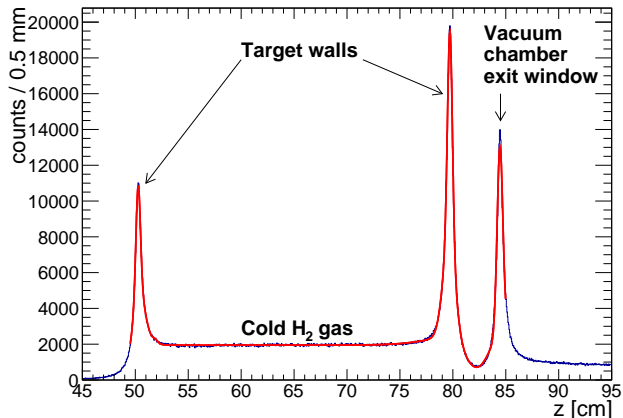


Figure 21: Reconstructed vertex positions within 1 cm radial distance with respect to the beam line for an empty target measurement. The curve shows the result of a fit to the vertex distribution used to determine the vertex resolution.

1341 reconstruct these windows as illustrated in Fig. 21. The distance of closest ap-
 1342 proach between two tracks, d , was required to be less than 1 cm. The vertex
 1343 position is at the mid-point of the line segment (of length d) defined by the
 1344 points of closest approach for each track. The estimated z -position resolution
 1345 is 3 mm.

1346 7. Electromagnetic calorimeters

1347 7.1. Barrel Calorimeter

1348 The Barrel Calorimeter (BCAL) is an electromagnetic sampling calorime-
 1349 ter in the shape of an open cylinder. Photon showers with energies between
 1350 0.05 GeV and several GeV, 11° – 126° in polar angle, and 0° – 360° in azimuthal
 1351 angle are detected. The geometry is fairly unique with the production target
 1352 located in the backward part of the cylinder, as shown in Fig. 1. The contain-
 1353 ment of showers depends on the angle of photon incidence, with a thickness of
 1354 15.3 radiation lengths for particles entering normal to the calorimeter face and
 1355 reaching up to 67 radiation lengths at 14° . Details of the design, construction
 1356 and performance of the BCAL can be found in Ref.[52].

1357 The BCAL is constructed as a lead and scintillating-fiber matrix, consisting
 1358 of 0.5 mm-thick corrugated lead sheets and 1.0 mm-diameter Kuraray SCSF-
 1359 78MJ multi-clad scintillating fibers. The fibers run parallel to the cylindrical
 1360 axis of the detector. Each module has approximately 185 layers and 15,000
 1361 fibers. The BCAL consists of 48 optically isolated modules, each with a trape-
 1362 zoidal cross section, forming a 3.9-m-long cylindrical shell having inner and
 1363 outer radii of 65 cm and 90 cm, respectively. The light generated in the fibers
 1364 is collected via small light guides at each end of the module, which transport

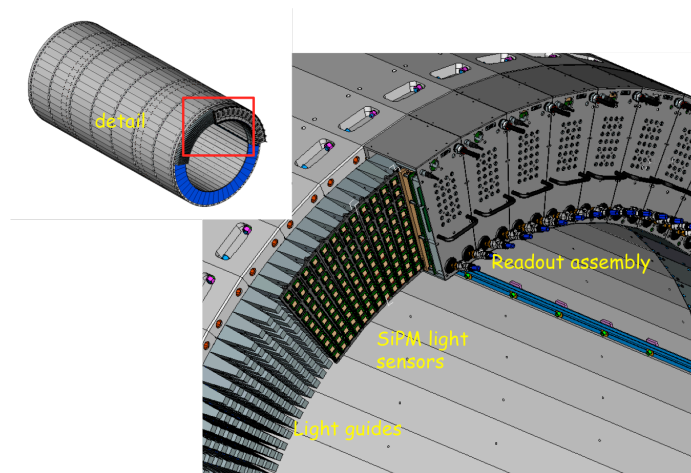


Figure 22: Three-dimensional rendition of the light guides mounted at the end of the BCAL, as well as the readout assemblies mounted over them. The readout assemblies contain the SiPMs and their electronics. (Color online)

1365 the light to silicon photomultipliers (SiPMs), which were chosen due to their
 1366 insensitivity to magnetic fields. The end of the calorimeter with light guides,
 1367 light sensors and electronics is shown in Fig. 22.

1368 The SiPM light sensors are Hamamatsu S12045(X) Multi-Pixel-Photon Counter
 1369 (MPPC) arrays ⁵¹, which are 4×4 arrays of 3×3 mm² tiles [53]. The SiPMs
 1370 were accepted following extensive testing [54, 55, 56, 57, 58, 59]. Four thousand
 1371 units were purchased and 3840 are installed in the detector. The gain of the
 1372 SiPM depends on the voltage above the breakdown voltage, about 70 V. These
 1373 are operated at 1.4 V over the breakdown voltage, selected to reduce the effect
 1374 of readout thresholds. Even at this relatively high over-bias, the noise level is
 1375 dominated by fluctuations in the electronics baseline and not by single-pixel
 1376 noise. In order to keep a constant gain, the temperature is maintained within
 1377 practical limits ($\pm 2^\circ\text{C}$) using a chilled-water system. The gain is stabilized
 1378 using a custom circuit that adjusts the bias voltage based on the measured tem-
 1379 perature. Two stages of preamplifiers and summing electronics are attached to
 1380 the sensors. In order to reduce the number of signals that are digitized, circuits

⁵¹Hamamatsu Corporation, Bridgewater, NJ 08807, USA
 (<http://sales.hamamatsu.com/en/home.php>).

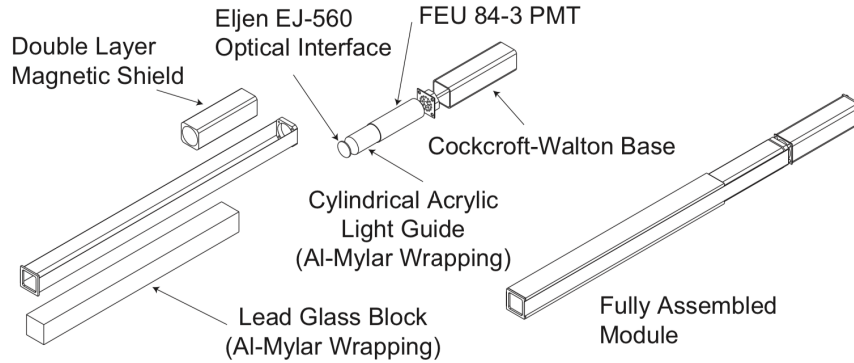


Figure 23: Expanded view of a single FCAL module.

1381 sum the outputs of the preamplifiers in groups of radial columns, with coarser
 1382 granularity away from the target. The layer closest to the target employs a
 1383 single SiPM, and the next three layers have two, three, and four SiPMs, respec-
 1384 tively. On the end of each module, forty SiPMs generate sixteen signals that are
 1385 delivered to FADCs and twelve signals that are discriminated and then recorded
 1386 with pipeline TDCs. The FADCs and TDCs are housed in VXS crates located
 1387 on the floor close to the detector (see Section 9).

1388 7.2. Forward Calorimeter

1389 The Forward Calorimeter (FCAL) detects photon showers with energies
 1390 ranging from 0.1 GeV to several GeV, and between 1° – 11° in polar angle. The
 1391 front face of the FCAL is located 5.6 m downstream from the center of the
 1392 GlueX target and consists of 2800 lead glass blocks stacked in a circular array
 1393 that has a diameter of 2.4 m. Each lead glass block has transverse dimensions
 1394 of $4 \times 4 \text{ cm}^2$ and length of 45 cm. The material of the lead-glass blocks is equiv-
 1395 alent to type F8 manufactured by the Lytkarino Optical Glass Factory.⁵² The
 1396 blocks and most of the PMTs were taken from the decommissioned experiments
 1397 E852 at Brookhaven National Laboratory [60] and the RadPhi Experiment at
 1398 JLab [61]. To remove accumulated radiation damage, the glass was annealed
 1399 by heat treatment prior to installation in GLUEX. The detector is enclosed in a
 1400 dark room.

1401 The light collection is accomplished via an Eljen EJ-560 optical interface
 1402 “cookie” and a UVT acrylic cylindrical light guide glued to the PMT. The light
 1403 guide recesses the magnetically sensitive photocathode of the PMT inside a dual
 1404 layer of soft iron and mu-metal that attenuates the stray field of the GLUEX
 1405 solenoid ($\lesssim 200 \text{ G}$). The sensors are FEU 84-3 PMTs with Cockcroft-Walton
 1406 bases, each consuming 0.2 W. The design of the PMT base is similar to that

⁵²<http://lzos.ru> .

1407 noted in Ref. [62], and eliminates the need for a 2800-channel high-voltage power
1408 system. The bases communicate with a controller using the CAN protocol [63],
1409 with 100 bases on each of 28 CAN buses. The communication allows continuous
1410 monitoring of the PMT voltages, temperatures, and current draw. A schematic
1411 of a single FCAL module is shown in Fig. 23 and more details may be found in
1412 Ref. [64]. FCAL signals are routed to FADC electronics, situated on a platform,
1413 directly behind the FCAL dark room.

1414 *7.3. Electronics*

1415 Custom readout electronics for the two calorimeters are mounted in standard
1416 VXS crates and include JLab 12-bit 250 MHz FADCs [65], discriminators [66]
1417 and F1 TDCs [47]. The maximum input scale of the FADCs (4095 counts) is set
1418 to 2 V. The FADCs sample each calorimeter channel every 4 ns and generate
1419 raw waveforms consisting of 100 samples (400 ns). The samples are available
1420 for further processing by the firmware upon a trigger signal, if the waveform
1421 exceeds a threshold voltage. The firmware computes several derived quantities
1422 of the pulse: pedestal, peak value, integral over a selected window, and time
1423 of the halfway point on the leading edge. At most one pulse is extracted from
1424 each readout window. These pulse features constitute the raw data that is
1425 nominally read out from the FADC. Optionally, the full waveforms can be read
1426 out for diagnostic purposes and to check the firmware output against the offline
1427 emulation of the parameter extraction; this is done for less than about 1% of
1428 the production runs.

1429 Pulses are identified by the first sample that exceeds a threshold, currently
1430 set to 5 (8) counts above the average pedestal for the BCAL (FCAL). These
1431 thresholds correspond to approximately 2.5 (12) MeV. The integral is deter-
1432 mined using a fixed number of samples relative to the threshold crossing, which
1433 was determined by maximizing the ratio of signal to pedestal noise. The inte-
1434 gration window begins one sample before the threshold time and extends to 26
1435 (15) samples after the threshold time for the BCAL (FCAL). Typical pedestal
1436 widths are $\sigma \sim 1.2$ - 1.3 (0.8) counts. For the BCAL, the pedestals are determined
1437 for each channel event-by-event, appropriately scaled, and then subtracted from
1438 the peak and integral to obtain signals proportional to the energy deposited in
1439 the calorimeter. For the FCAL, the average pedestal over a run period is deter-
1440 mined offline for each channel and the pedestal contribution to the pulse integral
1441 is subtracted when the data are reconstructed. The algorithm that determines
1442 the time of the pulse is pulse-height independent and, therefore, time-walk cor-
1443 rection is not required for the FADC times [67].

1444 The outputs of the three inner layers of the BCAL are also fanned out to
1445 leading-edge discriminators, which feed the JLab F1 TDCs. The discriminator
1446 thresholds are initially set to 35 mV and then adjusted channel by channel. The
1447 pulse times are recorded relative to the trigger in a 12-bit word. Multiple hits
1448 may be recorded per channel per event (up to eight), but are culled at a later
1449 time by comparison to FADC times. The nominal least count is configured to
1450 be 58 ps.

1451 *7.4. Calibration and monitoring*

1452 The relative gains of the calorimeters are monitored using a modular LED-
1453 driver system [68]. The control system is the same for both calorimeters, but
1454 the arrangement of LEDs is tailored to the respective detector geometries. In
1455 the BCAL, one LED is inserted into each light guide to monitor each individual
1456 SiPM and its partner at the far end of the module. Due to geometry, the
1457 illumination varies considerably from channel to channel. The average gain
1458 stability of the detector over a period of ten days is better than 1% and the
1459 fractional root-mean-square deviation of the mean for each SiPM during a single
1460 day from the average over the run period is typically less than 2%.

1461 For the FCAL, four acrylic panes were installed, each covering the upstream
1462 end of one quadrant of the FCAL. Each pane is illuminated by forty LEDs, ten
1463 violet, ten blue, and twenty green. In addition to monitoring the stability of
1464 the readout, the different colors are used to study the wavelength dependence of
1465 the transmission of light through the lead glass blocks. In particular, radiation
1466 damage to lead glass inhibits transmission at the blue end of the spectrum
1467 and tends to turn glass a brownish color [69]. Throughout a several-month
1468 experiment, the response to the green LEDs was unchanged. However, the PMT
1469 response to violet LEDs degraded by about 10% in the blocks closest to the beam
1470 line, characteristic of radiation damage. Such damage is only evident in the first
1471 two layers of blocks surrounding the 12 cm×12 cm beam hole. This damage is
1472 likely confined to the upstream end of the block and does not significantly affect
1473 the response to particle showers in the body of the glass.

1474 The energy of a photon or lepton is obtained from the reconstructed electro-
1475 magnetic shower. Here, a shower is reconstructed using an algorithm that finds
1476 a cluster by grouping signals close in time and space, called hits, that have been
1477 registered by individual detector elements. Details of the algorithms to obtain
1478 shower energies in the BCAL can be found in Ref. [52] and in Ref. [70] for the
1479 FCAL. The clustering in the FCAL requires that hits register within 15 ns of
1480 the primary hit, where the seed threshold is taken to be 35 MeV. Clusters with a
1481 single hit are discarded. In the event of overlapping showers, the hit energies are
1482 divided among the clusters in proportion to the partition predicted by a typical
1483 shower profile. Both detectors have sources of energy-dependent nonlinearities
1484 and empirical corrections are developed and applied to minimize the measured
1485 energy dependence of the measured π^0 mass.

1486 *7.5. Performance*

1487 The performance of the calorimeter is summarized by its ability to measure
1488 the energy, position and timing of electromagnetic showers.

1489 The energy resolution of each calorimeter was extracted from the measured
1490 π^0 and η mass distributions, yielding consistent results. To study the η mass
1491 resolution, events were selected using kinematic fits to $\gamma p \rightarrow p\pi^+\pi^-\gamma\gamma$, with
1492 $\eta \rightarrow \gamma\gamma$ and the photons having the same energies within 10%. The proton
1493 and pion tracks were used to determine the event vertex, needed to accurately
1494 reconstruct the two-photon invariant mass. This reaction provides a fairly clean

1495 sample of η 's with energy-symmetric photons recorded either both in the BCAL
 1496 or both in the FCAL. The single-photon energy resolution was determined from
 1497 Gaussian fits to the η invariant mass width, neglecting contributions from uncer-
 1498 tainty in the opening angle. Monte Carlo simulation of $\gamma p \rightarrow p\pi^+\pi^-\eta$ events,
 1499 with kinematics chosen to approximate the experimental distributions, were
 1500 used to tune the MC resolution to match the data. The single-photon resolu-
 1501 tions are shown in Fig. 24(a) for the BCAL and Fig. 24(b) for the FCAL as a
 1502 function of the mean photon energy, both for data and simulation. A fit has
 1503 been performed to the data for each calorimeter to estimate contributions to
 1504 the width from stochastic and constant processes. The parameters in the fit are
 1505 strongly correlated due to the limited range of energy available.⁵³

1506 The resolution of the position (Z) along the length of the BCAL (~ 2.5 cm)
 1507 is computed from the timing resolution of the system, which was measured to
 1508 be $\sigma = 150$ ps at 1 GeV. The transverse position resolution (σ) obtained from
 1509 simulation for 1 GeV showers in the FCAL is less than 1.1 cm.

1510 The performance of the calorimeters has been demonstrated in the recon-
 1511 struction of neutral states including π^0 , η and η' mesons for the first GLUEX
 1512 physics publications [71, 72]. In addition, although the response of the calorime-
 1513 ters at high energy is still under evaluation, it has provided important electron-
 1514 pion separation to identify the decays of $J/\psi \rightarrow e^+e^-$ [73] where electrons were
 1515 recorded up to 8 GeV.

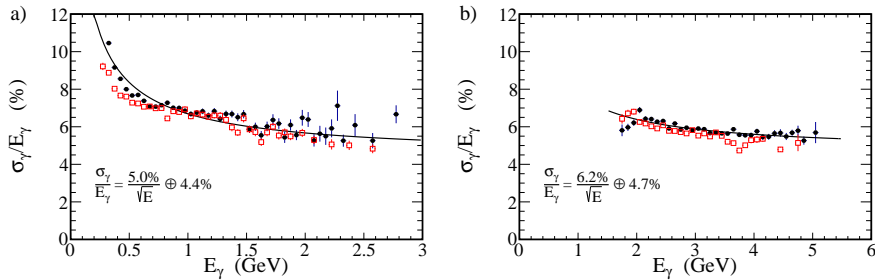


Figure 24: The energy resolution, σ_γ/E_γ , for single photons in the a) BCAL and b) FCAL calculated from the η mass distribution under the assumption that only the energy resolution contributes to its width. Solid black circles are data and open red squares are simulation. Fitted curves including the stochastic and constant terms are indicated. (Color online)

1516 8. Scintillation detectors

1517 There are two scintillator-based detectors deployed in the GLUEX spectrom-
 1518 eter: a small barrel-shaped detector surrounding the target, referred to as the

⁵³For the BCAL these data constitute an average over many angles, resulting in a relatively large effective constant term that cannot be extrapolated to higher energy. See Ref. [52] Section 11 for details.

1519 Start Counter (ST), and a two-plane hodoscope detector system in the forward
 1520 direction, referred to as the Time-of-Flight (TOF) detector. Both detectors pro-
 1521 vide timing information. Charged-particle identification is derived from energy
 1522 loss (dE/dx) in the ST and flight time from the TOF.

1523 *8.1. Start Counter*

1524 The ST, shown in Fig. 25, surrounds the target region and covers about 90%
 1525 of the solid angle for particles originating from the center of the target. The ST
 1526 is designed to operate at tagged photon beam intensities of up to 10^8 photons per
 1527 second in the coherent peak, and has a high degree of segmentation to limit the
 1528 per-paddle rates. The time resolution must be sufficient to resolve the RF beam
 1529 structure and identify the electron beam bunch from which the event originated
 1530 (see Section 2.1). The ST provides a timing signal that is relatively independent
 1531 of particle type and trajectory (because of its proximity to the target) and can
 1532 be used in the Level 1 trigger if necessary. The specific energy deposits dE/dx
 1533 in ST are used for charged-particle identification in combination with the flight-
 1534 time from the TOF. Details of the design, construction and performance of the
 1535 ST system can be found in Ref. [74].

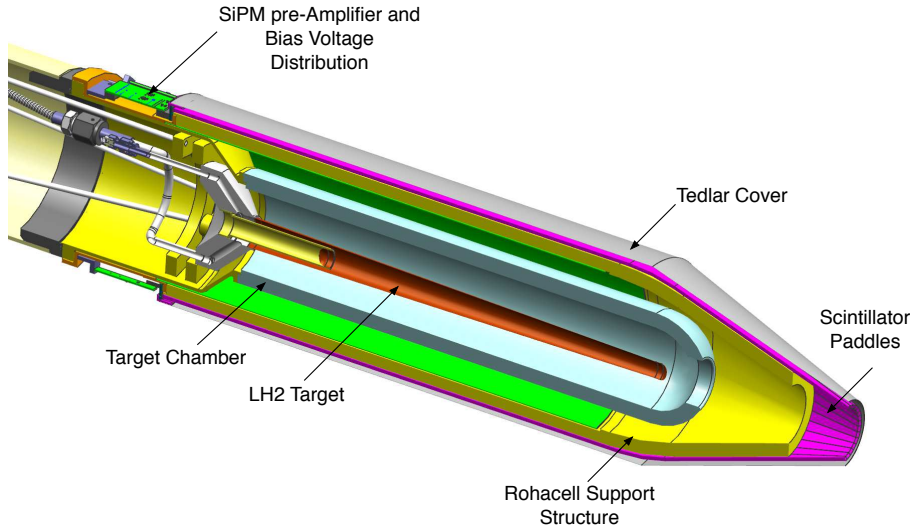


Figure 25: The GLUEX Start Counter surrounding the liquid-hydrogen target assembly. The incident beam travels from left to right down the central axis.

1536 The ST consists of 30 scintillator paddles arranged in a cylinder of radius
 1537 78 mm with a “nose” section that bends towards the beam line to a radius of

1538 20 mm at the downstream end. EJ-200 scintillator from Eljen Technology⁵⁴
1539 was selected for the ST paddles. EJ-200 has a decay time of 2.1 ns with a bulk
1540 attenuation length of 380 cm. Each scintillator paddle originated from stock
1541 3 mm thick and 600 mm in length. The paddles were bent at Eljen to create
1542 the nose section, and then machined at McNeal Enterprises Inc.⁵⁵ to their
1543 final shape, including edges beveled at 6° to minimize loss of acceptance. The
1544 scintillator paddles are supported by a Rohacell closed-cell foam structure. The
1545 Rohacell is 11 mm thick and is rigidly attached to an aluminum support hub
1546 at the upstream end. The downstream support extends partially into the nose
1547 section. The cylindrical length of the Rohacell is further reinforced with three
1548 layers of carbon fiber, each layer being 650 μm thick. The assembly is made
1549 light-tight with a Tedlar wrapping, attached to a plastic collar at the upstream
1550 end.

1551 Silicon photomultiplier detectors are used as light sensors, as these are not
1552 affected by the magnetic field produced by the solenoid. The SiPMs were placed
1553 at the upstream end of each scintillator element with a 250 μm air gap. Each
1554 paddle is read out with an array of four SiPMs (Hamamatsu S109031-050P
1555 multi-pixel photon counters) whose signals are summed. The on-board elec-
1556 tronics provides two signals per paddle, one delivered to an FADC, and the
1557 other to a 5× amplifier that is sent to a discriminator and then to a TDC.

1558 8.2. Time-of-flight counters

1559 The TOF system delivers fast timing signals from charged particles passing
1560 through the detector, thereby providing information for particle identification.
1561 The TOF detector is a wall of scintillators located about 5.5 m downstream from
1562 the target, covering a polar angular region from 0.6° to 13°. The detector has
1563 two planes of scintillator paddles stacked in the horizontal and vertical direction.
1564 Most paddles are 252 cm long and 2.54 cm thick with a width of 6 cm. The
1565 scintillator material is EJ-200 from Eljen Technology. To allow the photon
1566 beam to pass through the central region, an aperture of 12×12 cm² is kept free
1567 of any detector material by using four shorter, single-PMT paddle detectors
1568 with a length of 120 cm around the beam hole in each detector plane. These
1569 paddles also have a width of 6 cm and a thickness of 2.54 cm. In order to keep
1570 the count rate of the paddles well below 2 MHz the two innermost full-length
1571 paddles closest to the beam hole on either side have a reduced width of 3 cm.
1572 Light guides built out of UV transmitting plastic provide the coupling between
1573 the scintillator and the PMT and allow the magnetic shielding to protect the
1574 photocathode by extending about 5 cm past the PMT entrance window. All
1575 paddles are wrapped with a layer of a highly reflective material (DF2000MA
1576 from 3M) followed by a layer of strong black Tedlar film for light tightness.

1577 The scintillator paddles are read out using PMTs from Hamamatsu.⁵⁶ Full-

⁵⁴Eljen Technology, <https://eljentechnology.com/products/plastic-scintillators>.

⁵⁵McNeal Enterprises Inc., <http://www.mcnealplasticmachining.com>

⁵⁶Hamamatsu Photonics, <https://www.hamamatsu.com/us/en/index.html>.

1578 length paddles have a PMT at both ends, while the short paddles have a single
1579 PMT at the outer end of the detector. These type H10534 tubes have ten stages
1580 and are complete assemblies with high voltage base, casing and μ -metal shield-
1581 ing. Additional soft-iron external shielding protects each PMT from significant
1582 stray fields from the solenoid magnet.

1583 *8.3. Electronics*

1584 High voltage for the TOF PMTs is provided by CAEN HV modules of type
1585 A1535SN, initially controlled by a CAEN SY1527 main frame and later up-
1586 graded to a SY4527. The PMT outputs are connected to a passive splitter by
1587 a 55'-long RG-58 coaxial cables. The signal is split into two equal-amplitude
1588 signals. One signal is directly connected to a FADC [75], while the second signal
1589 passes first through a leading-edge discriminator and is then used as an input
1590 to a high resolution TDC. The digitizing modules are mounted in VXS crates
1591 as described in Section 9. The threshold of the leading-edge discriminator is
1592 controlled separately for each channel and has an intrinsic deadtime of about
1593 25 ns.

1594 The sparsification threshold for the FADC is set to 120 (160) counts for
1595 the ST (TOF), with the nominal pedestal set at 100 counts. The high voltage
1596 of each TOF PMT is adjusted to generate a signal amplitude of at least 400
1597 ADC counts above baseline from a minimum-ionizing particle. The data from
1598 the FADC are provided by the FPGA algorithm and consist of two words per
1599 channel with information about pedestal, signal amplitude, signal integral, and
1600 timing.

1601 The timing signals from the ST system are registered using the JLab F1
1602 TDCs, which have a nominal least count of 58 ps. In order to take advantage
1603 of the higher intrinsic resolution of the TOF counters, this system uses the
1604 VX1290A TDCs from CAEN⁵⁷, which are multi-hit high-resolution TDCs with
1605 a buffer of up to 8 words per channel and a nominal least count of 25 ps. Since
1606 these TDCs provide the best time measurements in the GLUEX detector, the
1607 timing of the accelerator RF signal is also digitized using these TDCs.

1608 *8.4. Calibration and monitoring*

1609 The combined ST and TOF systems are used to determine the flight times
1610 of particles, the ST providing a precise start time in combination with the
1611 accelerator RF, and the TOF providing the stop time. Both systems may also
1612 be used to provide information on particle energy loss. Therefore, the signals
1613 in ST and TOF must be calibrated to determine corrections for the effects of
1614 time-walk, light propagation time offsets, and light attenuation. The procedures
1615 are slightly different for the two detectors because of the different geometries,
1616 intrinsic resolutions, and the advantages of the TOF system having two adjacent
1617 perpendicular planes.

⁵⁷CAEN, <https://www.caen.it/>

1618 For the time-walk correction for each paddle of the ST, the detector signal is
 1619 sent to both an FADC and a TDC. The time from the FADC, being independent
 1620 of pulse amplitude, is the reference. The amplitude dependence of the difference
 1621 between TDC and FDC times is used to measure the time walk; the resulting
 1622 curve is fit to an empirical function for use in the correction. The propagation
 1623 time is measured as a function of the hit position in a paddle as determined
 1624 by well-reconstructed charged particle tracks. The propagation velocity is measured
 1625 in three regions of the counter (“straight,” “bend,” and “nose”) and is not
 1626 assumed to be a single value for all hits. The light attenuation is also measured
 1627 at several positions along the counter using charged particle tracks. The energy-
 1628 per-unit pathlength in the paddle as a function of distance from the SiPM is
 1629 fit to a modified exponential, with different parameters allowed for the straight
 1630 section and the nose section, with continuity enforced at the section boundary.

1631 The calibration procedures for the TOF system take advantage of the two
 1632 planes of narrow paddles oriented orthogonal to each other, which permits cal-
 1633 ibration of the full TOF detector independently of any other external detector
 1634 information. The overlap region of two full-length paddles from the two planes
 1635 defines a 6×6 cm² area for most paddles, with a few 3×3 cm² areas close to
 1636 the beam hole. The separation between the two detector planes is minimal as
 1637 they are mounted adjacent to each other, separated only by wrapping material.
 1638 While the time-difference (TD) between the two ends of a paddle is related to
 1639 the hit position along the paddle, the mean-time (MT) is related to the flight
 1640 time of a particle from the vertex to the paddle. Therefore, the MT for two
 1641 overlapping paddles must be the same when hit by the same particle passing
 1642 through both paddles, while the hit positions in the horizontal and vertical di-
 1643 mensions are defined by the TD of the two paddles. This relationship results
 1644 in an internally consistent calibration of all paddles with respect to every other
 1645 paddle. Prior to finding timing offsets for calibration, all times are corrected
 1646 for the amplitude-dependent walk. The relation between time at threshold and
 1647 signal amplitude is parameterized and used to correct for time slewing.

1648 After all full-length paddles have been calibrated, they can be used them-
 1649 selves as references to calibrate the remaining eight short paddles that only
 1650 have single-ended readout. Again we use the fact that any overlap region of two
 1651 paddles from different planes has the same particle flight time from the vertex.
 1652 This coincidence produces peaks in the time difference distributions that can be
 1653 used to determine the timing offsets of these single-ended readout paddles.

1654 To test the calibration, we take tracks that are incident on a paddle in one
 1655 plane and compute the time difference between the MT of that paddle and
 1656 the MT of every other full-length paddle in the other plane. The resulting
 1657 distribution of these differences is shown in Fig. 26. Assuming that all paddles
 1658 have the same timing resolution, we can compute the average time resolution
 1659 to be $\sigma = 105$ ps = $\frac{148}{\sqrt{2}}$ ps, assuming a Gaussian distribution.

1660 8.5. Performance

1661 The purpose of the ST is to select the electron beam bunch that generated
 1662 the tagged photon which induced a reaction in the target. The corresponding

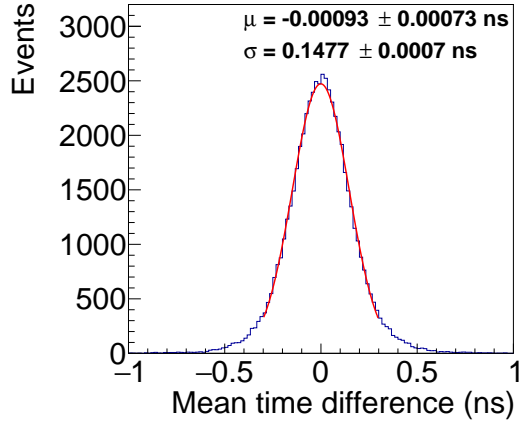


Figure 26: Mean time difference between one TOF long paddle of one plane with all other long paddles of the other plane. (Color online)

1663 time derived from a signal from the CEBAF accelerator, which is synchronized
 1664 with the RF time structure of the machine, is used to determine the event start
 1665 time. Therefore, the ST resolution does not contribute to the resolution of the
 1666 flight time as long as the resolution is sufficient to pick out the correct beam
 1667 bunch with high probability.

1668 The ST timing performance can be determined by comparing the event time
 1669 at the target measured by the start counter and the accelerator RF time. The
 1670 start counter time must be corrected for the flight path of the charged particle
 1671 emerging from the event, and all instrumental corrections mentioned in the
 1672 previous section must be applied. Fig. 27 shows the distribution of this time
 1673 difference. The average time resolution is about $\sigma=234$ ps, where the resolution
 1674 varies depending on the position of the hit along the counter.

1675 The ST is also used to identify particles using dE/dx . Fig. 28 shows dE/dx
 1676 versus momentum, p , for charged particles tracked to the Start Counter. Protons
 1677 can be separated from pions up to $p = 0.9$ GeV/ c .

1678 The performance of the TOF detector for particle identification (PID) was
 1679 investigated by considering the relative number of particle types within the event
 1680 sample. Events with at least three fully-reconstructed positively-charged tracks
 1681 were selected, with at least one of these tracks intersecting the TOF detector.
 1682 More pions are expected than protons, and more protons than kaons. Looking
 1683 at the distribution of velocity, β , of these tracks as a function of momentum,
 1684 the bands from protons, kaons and pions are identified (see Fig. 29).

1685 The distributions of β at two specific track momenta, 2 GeV/ c and 4 GeV/ c
 1686 (see Fig. 30), are illustrative of the PID capability of the TOF detector. At
 1687 $p = 2$ GeV/ c , the TOF detector provides about a 4σ separation between the
 1688 pion/positron peak and the kaon peak, sufficient to identify tracks as kaons

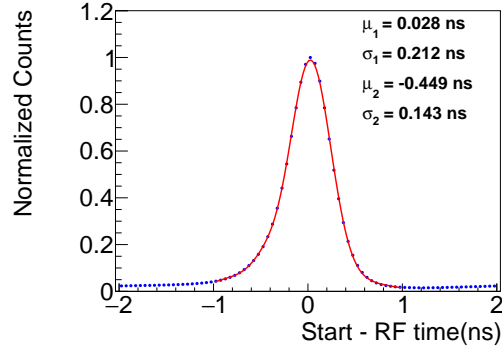


Figure 27: Time difference distribution between the vertex time computed from the start counter and the accelerator RF. The time from the RF does not contribute significantly to the width of the distribution. The fit function is a double Gaussian plus a third-degree polynomial.

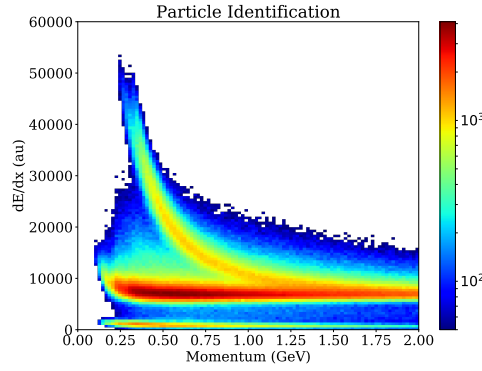


Figure 28: dE/dx vs. p for the Start Counter. The curved band corresponds to protons while the horizontal band corresponds to electrons, pions, and kaons. Pion/proton separation is achievable for tracks with $p < 0.9$ GeV/ c .

1689 with $\beta = 0.97$, or lower, with very high certainty. However, at $\beta = 0.98$, the
 1690 probability of the track being a kaon is less than 50%, due to the abundance
 1691 of pions that is an order of magnitude larger than kaons. The protons, on the
 1692 other hand, are very well separated from the other particle types and can be
 1693 identified with high confidence over the full range in β . At a track momentum
 1694 of 4 GeV/ c , PID becomes much more difficult and represents the limit at which
 1695 the time-of-flight measurement can identify protons with high confidence. The
 1696 separation between the large peak containing pions, kaons and positrons from
 1697 the proton peak is about 4σ , while the relative abundance in this case is about
 1698 a factor of 4. As a consequence, a 4 GeV/ c momentum track with $\beta = 0.975$
 1699 is most likely a proton, with a small probability of being a pion. At $\beta = 0.98$,

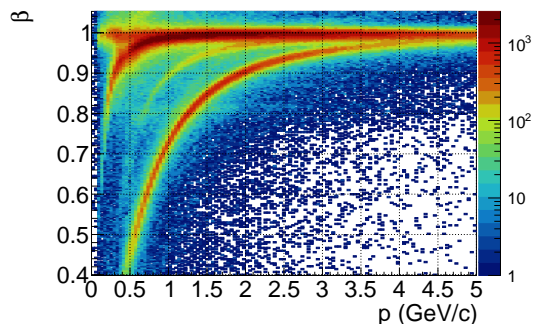


Figure 29: β of positive tracks versus track momentum, showing bands for e^+ , π^+ , K^+ and p . The color coding of the third dimension is in logarithmic scale. (Color online)

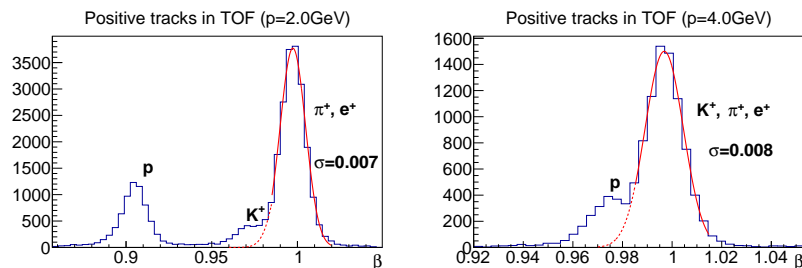


Figure 30: β of positive tracks with 2 GeV/c momentum (left) and with 4 GeV/c (right).

1700 such a track has a similar probability for being a proton or a pion.

1701 9. Trigger

1702 The goal of the GLUEX trigger is to accept most high-energy hadronic inter-
 1703 actions while reducing the background rate induced by electromagnetic and
 1704 low-energy hadronic interactions to the level acceptable by the data acquisition
 1705 system (DAQ). The main trigger algorithm is based on measurements of energy
 1706 depositions in the FCAL and BCAL as described in Ref. [76, 77]. Supplemen-
 1707 tary triggers can also use hits from scintillator detectors, such as the PS, tagging
 1708 detectors, ST, TOF, and TAC.

1709 9.1. Architecture

1710 The GLUEX trigger system[78] is implemented on dedicated programmable
 1711 pipelined electronics modules, designed at JLab using Field-Programmable Gate
 1712 Arrays (FPGAs). The GLUEX trigger and readout electronics are hosted in VXS
 1713 (ANSI/VITA 41.0) crates. VXS is an extension of the VME/VME64x architec-
 1714 ture, which uses high-speed backplane lines to transmit trigger information.

1715 A layout of the trigger system is presented in Fig. 31. Data from the FCAL
 1716 and BCAL are sent to FADC modules [75], situated in 12 and 8 VXS crates,
 1717 respectively, and are digitized at the sampling rate of 250 MHz. The digitized
 1718 amplitudes are used for the trigger and are also stored in the FPGA-based
 1719 pipeline for subsequent readout via VME. Digitized amplitudes are summed for
 1720 all 16 FADC250 channels in each 4 ns sampling interval and are transmitted to
 1721 the crate trigger processor (CTP) module, which sums up amplitudes from all
 1722 FADC boards in the crate. The sub-system processor (SSP) modules located
 1723 in the global trigger crate receive amplitudes from all crates and compute the
 1724 total energy deposited in the FCAL and BCAL. The global trigger processor
 1725 (GTP) module collects data from the SSPs and makes a trigger decision based
 1726 on the encoded trigger equations. The core of the trigger system is the trigger
 1727 supervisor (TS) module, which receives the trigger information from the GTP
 1728 and distributes triggers to the electronics modules in all readout crates in order
 1729 to initiate the data readout. The GLUEX system has 55 VXS crates in total (26
 1730 with FADC250s, 14 with FADC125s, 14 with F1 TDCs, and 1 CAEN TDC). The
 1731 TS also provides a synchronization of all crates and provides a 250 MHz clock
 1732 signal. The triggers and clock are distributed through the trigger distribution
 1733 (TD) module in the trigger distribution crate. The signals are received by
 1734 the trigger interface (TI) module and signal distribution (SD) module in each
 1735 crate. The GLUEX trigger system provides a fixed latency. The longest trigger
 1736 distribution time of about $3.3 \mu\text{s}$ is due to the distance of the tagger hall from
 1737 Hall D. The smallest rewritable readout buffer, where hits from the detector are
 1738 stored, corresponds to about $3.7 \mu\text{s}$ for the F1 TDC module. The trigger jitter
 1739 does not exceed 4 ns.

1740 9.2. Trigger types

1741 The GLUEX experiment uses two main trigger types: the pair spectrome-
 1742 ter trigger, and the physics trigger based on energy depositions in the BCAL
 1743 and FCAL. The pair spectrometer trigger is used to measure the flux of beam
 1744 photons. This trigger requires a time coincidence of hits in the two arms of the
 1745 PS detector, described in Section 2.10. The physics triggers are generated when
 1746 the FCAL and BCAL energies satisfy the following conditions:

- 1747 1. $2 \cdot E_{\text{FCAL}} + E_{\text{BCAL}} > 1 \text{ GeV}$, $E_{\text{FCAL}} > 0 \text{ GeV}$, and
- 1748
- 1749 2. $E_{\text{BCAL}} > 1.2 \text{ GeV}$.

1750 The first condition defines the main trigger that uses the fact that most events
 1751 produce forward-going energy. The second trigger type is used to accept events
 1752 with large transverse energy released in the BCAL, such as decays of J/ψ
 1753 mesons.

1754 Several other trigger types were implemented for efficiency studies and de-
 1755 tector calibration. Efficiency of the main production trigger was studied using
 1756 a trigger based on the coincidence of hits from the ST and TAGH, detectors not
 1757 used in the main production trigger. A combination of the PS and TAC triggers
 1758 was used for the acceptance calibration of the PS, described in Section 2.10.1.

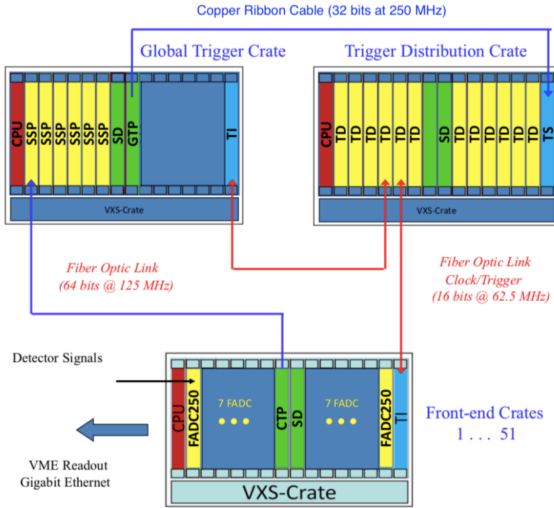


Figure 31: Schematic view of the Level-1 trigger system of the GLUEX experiment. The electronics boards are described in the text.

1759 Ancillary minimum-bias random trigger and calorimeter LED triggers were col-
 1760 lected concurrently with data taking.

1761 9.3. Performance

1762 The rate of the main physics triggers as a function of the PS trigger rate is
 1763 shown in Fig. 32. The typical rate of the PS trigger in spring 2018 was about
 1764 3 kHz, which corresponds to a photon beam flux of $2.5 \cdot 10^7 \gamma/\text{sec}$ in the coherent
 1765 peak range. The total trigger rate was about 40 kHz. The rates of the random
 1766 trigger and each of the LED calorimeter triggers were set to 100 Hz and 10 Hz,
 1767 respectively. The electronics and DAQ were running with a livetime close to
 1768 100%, collecting data at a rate of 600 MB per second. The trigger system can
 1769 operate at significantly higher rates, considered for the next phase of the GlueX
 1770 experiment. The combined dead time of the trigger and DAQ systems at the
 1771 trigger rate of 80 kHz was measured to be about 10%. The largest contribution
 1772 to the dead time comes from the hit processing time of readout electronics
 1773 modules.

1774 10. Data acquisition

1775 The GLUEX data acquisition software uses the CEBAF Online Data Ac-
 1776 quisition (CODA) framework. CODA is a software toolkit of applications and
 1777 libraries that allows customized data acquisition systems based on distributed
 1778 commercial networks. A detailed description of CODA software and hardware
 1779 can be found in Ref. [79].

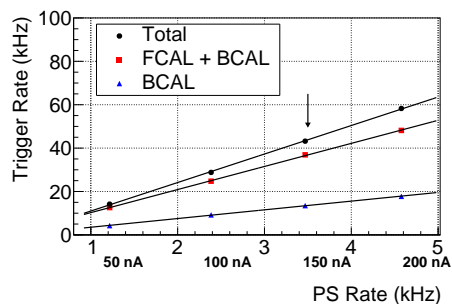


Figure 32: Rates of the main production triggers as a function of the PS rate: FCAL and BCAL trigger (boxes), BCAL trigger (triangles), the total trigger rate (circles). The vertical arrow indicates the run conditions during the spring of 2018 with a diamond radiator, 5 mm collimator and 75 μm Be converter.

1780 The maximum readout capability of the electronics in the VME/VXS crate is
 1781 200 MB/s per crate and the number of crates producing data is about 55. The
 1782 data from the electronic modules are read via the VME back-plane (2eSST,
 1783 parallel bus) by the crate readout controller (ROC), which is a single-board
 1784 computer running Linux. The GLUEX network layout and data flow are shown
 1785 in Fig. 33. Typical data rates from a single ROC are in the range of 20–70 MB/s,
 1786 depending on the detector type and trigger rate. The ROC transfers data over
 1787 1 Gbit Ethernet links to Data Concentrators (DC) using buffers containing event
 1788 fragments from 40 triggers at a time. Data Concentrators are programs that
 1789 build partial events received from 10-12 crates and run on a dedicated computer
 1790 node. The DC output traffic of 200-600 MB/s is routed to the Event Builder
 1791 (EB) to build complete events. The Event Recorder (ER), which is typically
 1792 running on the same node as an Event Builder, writes data to local data storage.
 1793 GLUEX has been collecting data at a rate of 500–900 MB/s, which allows the
 1794 ER to write out to a single output stream. The system is expandable to handle
 1795 higher luminosity where rates rise to 1.5–2.5 GB/s. In this case, the ER must
 1796 write multi-stream data to several files in parallel. All DAQ computer nodes
 1797 are connected to both a 40 Gb Ethernet switch and a 56 Gb Infiniband switch.
 1798 The Ethernet network is used exclusively for DAQ purposes: receiving data
 1799 from detectors, building events, and writing data to disk, while the Infiniband
 1800 network is used to transfer events for online data quality monitoring. This allows
 1801 decoupling DAQ and monitoring network traffic. The livetime of the DAQ is
 1802 in the range of 92–100%. The deadtime arises from readout electronics and
 1803 depends on the trigger rate. The DAQ software does not cause dead time during
 1804 an experimental run, but software-related dead time appears while stopping and
 1805 starting the run, which takes between 2-8 minutes.

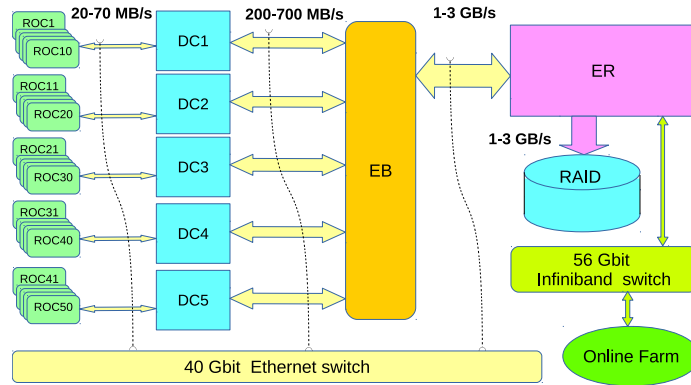


Figure 33: Schematic DAQ configuration for GLUEX. The high-speed DAQ connections between the ROCs and the ER are contained within an isolated network. The logical data paths are indicated by arrows, although physically they are routed through the 40 Gbit ethernet switch. The online monitoring system uses its own separate 56 Infiniband switch.

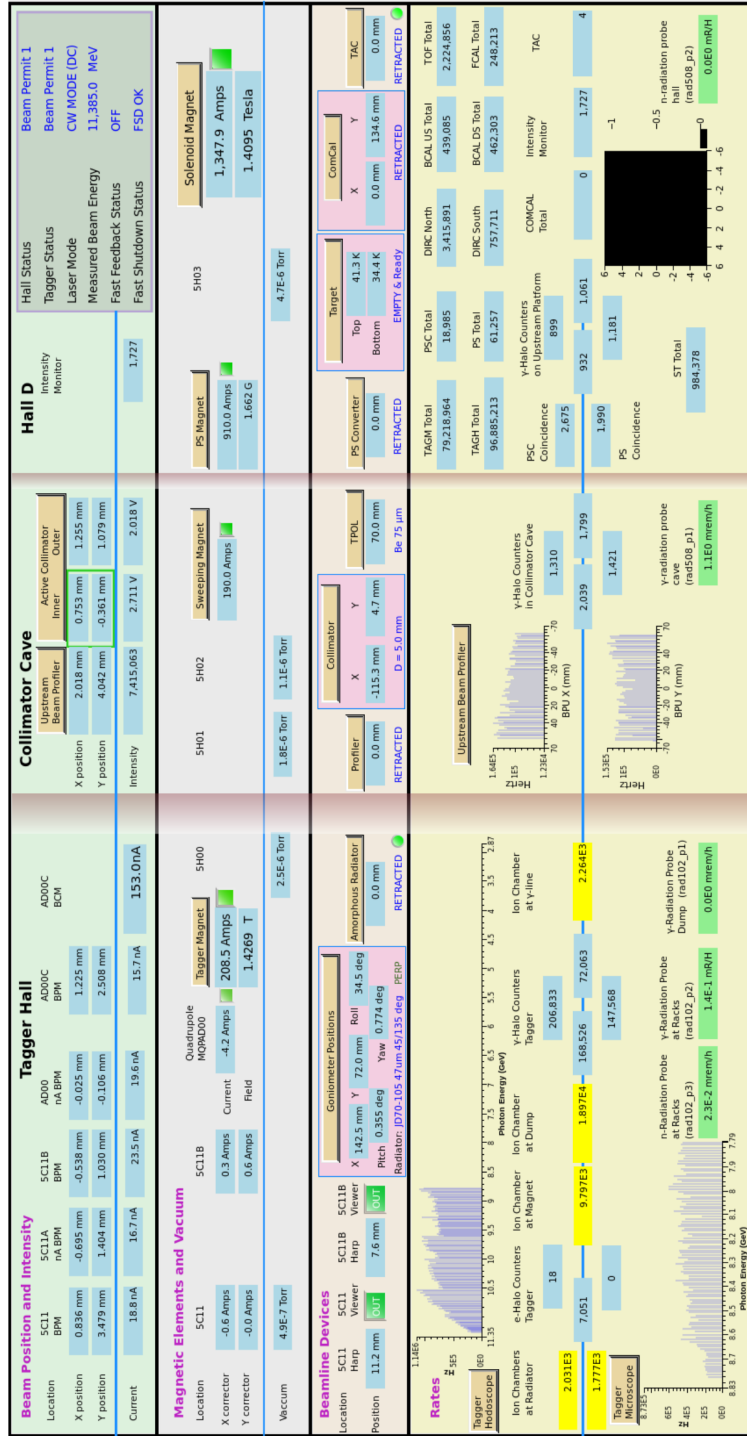


Figure 34: Top-level graphical interface for the beamline. This screen provides information on beam currents and rates, radiators, magnet status, target condition, background levels, etc.

1806 11. Slow controls

1807 GLUEX must monitor and control tens of thousands of different variables
1808 that define the state of the experimental hardware. The values need to be
1809 acquired, displayed, archived, and used as inputs to control loops continually
1810 with a high degree of reliability. For GLUEX, approximately 90,000 variables
1811 are archived, and many more are monitored.

1812 11.1. Architecture

1813 The GLUEX slow control system consists of three layers. The first layer
1814 consists of the remote units such as high voltage or low voltage power chas-
1815 sis, magnet power supplies, temperature controller, LabView applications, and
1816 PLC-based applications, which directly interact with the hardware and contain
1817 almost the all the control loops. The second layer is the Supervisory Control
1818 and Data Acquisition (SCADA) layer, which is implemented via approximately
1819 140 EPICS Input/Output Controllers (IOCs). This layer provides the inter-
1820 face between low level applications and higher level applications via the EPICS
1821 ChannelAccess protocol. The highest level, referred as the Experiment Control
1822 System (ECS), contains applications such as Human-Machine Interfaces, the
1823 alarm system, and data archiving system. This structure allows for relatively
1824 simple and seamless addition and integration of new components into the overall
1825 controls system.

1826 11.2. Remote Units

1827 GLUEX uses a variety of commercial units to provide control over the hard-
1828 ware used in the experiment. For instance, most detector high voltages are
1829 provided by the CAEN SYx527 voltage mainframe,⁵⁸ while the low and bias
1830 voltages are provided by boards residing in a Wiener MPOD chassis⁵⁹. These
1831 two power supply types provide most voltages for detector elements with the
1832 exception of the Tagger Microscope and the Forward Calorimeter. Here custom
1833 systems were developed that provide voltage regulation and interact with the
1834 EPICS-based layer through higher level interfaces using custom protocols. See
1835 Sections 2.4.2 and 7.2 for more details.

1836 Various beam line devices need to be moved during beam operations. Step-
1837 per motors are used to move motorized stages via Newport XPS universal
1838 multi-axis motion controllers⁶⁰ that allow for execution of complex trajec-
1839 tories involving multiple axes. All stage referencing, motion profile computations,
1840 and encoder-based closed-loop control occurs within the controller chassis after
1841 the basic parameters, such as positions and velocities, are provided by the user
1842 via a TCP/IP-based interface to EPICS.

⁵⁸<https://www.caen.it/subfamilies/mainframes/>

⁵⁹<http://www.wiener-d.com/sc/power-supplies/mpod-lvhv/mpod-crate.html>

⁶⁰<https://www.newport.com/c/xps-universal-multi-axis-motion-controller>.

1843 Custom controls were often developed for each complex installation, such
1844 as a superconducting magnet that requires large numbers of input and out-
1845 put channels and sophisticated logic. For these cases, we used Allen-Bradley
1846 CompactLogix and ControlLogix PLC systems⁶¹. These systems are designed
1847 for industrial operations, allow modular design, provide high reliability, and re-
1848 quire minimal maintenance. All controls loops are programmed within the PLC
1849 application, and are interfaced with EPICS through a TCP/IP-EtherNet/IP-
1850 proprietary protocol to allow access by higher level applications to process vari-
1851 ables delivered by the PLCs.

1852 The cryogenic target and the superconducting solenoid employ National In-
1853 struments LabView applications. The target controls use both custom-made
1854 and vendor-supplied hardware that include built-in remotely-accessible control
1855 systems and an NI CompactRIO⁶² chassis. This chassis communicates with the
1856 hardware and serves variables using an internal ChannelAccess server and an
1857 EPICS IOC running on the CompactRIO controller, as described in Sec. 4. A
1858 National Instruments PXI high-performance system⁶³ is used to collect data
1859 from different sensors of the solenoid as described in Sec. 3.

1860 *11.3. Supervisory Control and Data Acquisition layer*

1861 The SCADA layer is the middle layer that distributes the process variables
1862 allowing the higher level –and sometimes lower level– applications to use various
1863 process variables of the Hall-D control system. This layer is based on EPICS
1864 and uses the ChannelAccess protocol to publish the values of the variables over
1865 Ethernet. Efficient exchange of the information between the experiment and ac-
1866 celerator operations is achieved because the accelerator controls also use EPICS.
1867 Several dozen software IOC processes, running on host computers of the exper-
1868 iment control process, collect data from different components of the lowest layer.
1869 Each IOC is configured to communicate using the protocol appropriate for the
1870 remote units with which data exchange is needed. For instance, the IOC con-
1871 trolling the voltage for the FDC detector needs to be able to communicate with
1872 the Wiener MPOD and CAEN SYx527 voltage chassis. The middle layer is
1873 primarily used to distribute data between different applications. This layer also
1874 contains some EPICS-based applications running on IOCs that provide differ-
1875 ent control loops and software interlocks. For instance, the low-voltage power
1876 supplies for the FDC detector (see Sec. 5.2) are shut off if the temperature or
1877 the flow of the coolant in the chiller falls outside of required limits.

1878 *11.4. Experiment Control System*

1879 The highest level of controls contains applications that archive data, display
1880 data in interactive GUIs and as stripcharts, alarm and notify shift personnel

⁶¹<https://ab.rockwellautomation.com>.

⁶²<https://www.ni.com/en-us/shop/compactrio.html>

⁶³<https://www.ni.com/en-us/shop/pxi.html>

1881 and experts when problems occur, and interface with the CODA-based data ac-
1882 quisition system (Sec. 10). An example of such a GUI is the beamline overview
1883 screen, shown in Fig. 34. Many of the buttons of the GUI are active and allow
1884 access to other GUIs. Display management and the alarm system for GLUEx
1885 controls are based on Controls System Studio (CSS),⁶⁴ which is an Eclipse-
1886 based toolkit for operating large systems. CSS is well suited for systems that
1887 use EPICS as an integral component. Although CSS provides an archiving
1888 engine and stripcharting tools, the MYA archiver,[80] provided by the JLab ac-
1889 celerator software group, was employed with its tools for displaying the archived
1890 data as a time-series. Display management for GLUEx controls is within the
1891 CSS BOY [81] environment, which allows system experts to build sophisticated
1892 control screens using standard widgets. The alarm system is based on the CSS
1893 BEAST[82] alarm handler software, which alerts shift personnel of problems
1894 with the detector, and notifies a system expert if the problems are not resolved
1895 by shift personnel.

1896 12. Online computing system

1897 This section describes the GLUEx software and computing systems used for
1898 data monitoring and for transport to the tape system for permanent storage.

1899 12.1. Monitoring

1900 The Online Monitoring system consists of multiple stages that provide im-
1901 mediate monitoring of the data, as well as near-term monitoring (a few hours
1902 after acquisition). Immediate monitoring is based on the *RootSpy* system[83]
1903 written for use in GLUEx, though its design is not experiment specific. Fig-
1904 ure 35 shows a diagram of the processes involved in the RootSpy system and
1905 how those processes are coupled to the DAQ system. The Event Transfer (ET)
1906 process is part of the CODA DAQ system [84] and is used to extract a copy
1907 of a portion of the datastream without interfering with data acquisition. The
1908 monitoring system uses a secondary ET to minimize connections to the RAID
1909 server running the Event Recorder process.

1910 The monitoring system is run on a small computer farm⁶⁵, with each com-
1911 puter processing a small part of the data stream. In total, about 10% of the
1912 data is processed for the low level occupancy plots while roughly 2% is fully
1913 reconstructed for higher level analysis. The CODA ET software system is used
1914 to distribute the data among the farm computers. Each farm node generates
1915 histograms, which *RootSpy* gathers and combines before display to shift workers
1916 in a GUI. Plots are displayed via a set of ROOT [85] macros, each responsible

⁶⁴<http://controlsystemstudio.org/>

⁶⁵The online monitoring farm consists of eight 2012 era Intel x86_64 computers with 16 cores+16 hyper-threads (ht) plus six 2016 era Intel x86_64 computers with 36 cores + 36ht. The monitoring farm uses 40 Gbps (QDR) and 56 Gbps(FDR) IB for the primary interconnect. Note that the DAQ system uses a separate 40 Gbps ethernet network that is independent of the farm.

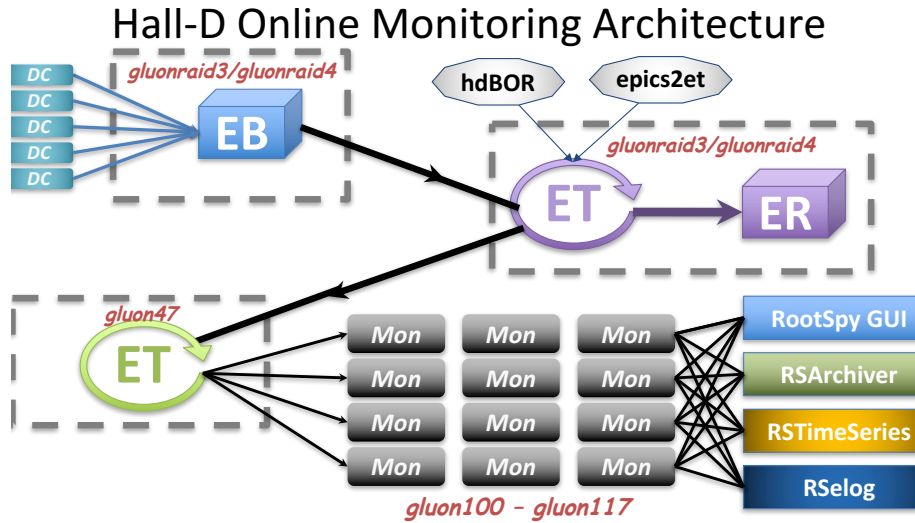


Figure 35: Processes distributed across several computers in the online monitoring system. DC, EB, and ER are the Data Concentrator, Event Builder, and Event Recorder processes, respectively, in the CODA DAQ system.

1917 for drawing a single page. Most macros divide the page into multiple sections
 1918 so that multiple plots can be displayed on a single page. Figure 36 shows an
 1919 example of a high-level monitoring plot, where four invariant-mass distributions
 1920 are shown with fits. Values extracted from the fits are printed on the plots for
 1921 easy quantitative comparison to a reference plot.

1922 There are several client programs that summarize the information available
 1923 in the histograms produced by *RootSpy* and generate output that make it easy to
 1924 assess the uniformity and quality of the data. One of these is the *RSTimeSeries*
 1925 program, which periodically inserts data into an InfluxDB time series database.
 1926 The database provides a web-accessible strip chart of detector hit rates and
 1927 reconstructed quantities (e.g. number of ρ 's per 1k triggers). Another is the
 1928 *RSArchiver* program that gathers summed histograms to be displayed in the
 1929 Plot Browser⁶⁶ website. Plot Browser provides easy comparison of plots between
 1930 different runs and between different analysis passes. Jobs are automatically
 1931 submitted to the JLab farm for full reconstruction of the first five files (100GB)
 1932 of each run. The results are displayed in Plot Browser and may be compared
 1933 directly with the online analysis of the same run.

1934 12.2. Data transport and storage

1935 GLUEX Phase I generated production data at rates up to 650MB/s. The
 1936 data were temporarily stored on large RAID-6 disk arrays, and then copied to

⁶⁶https://halldweb.jlab.org/data_monitoring/Plot_Browser.html.

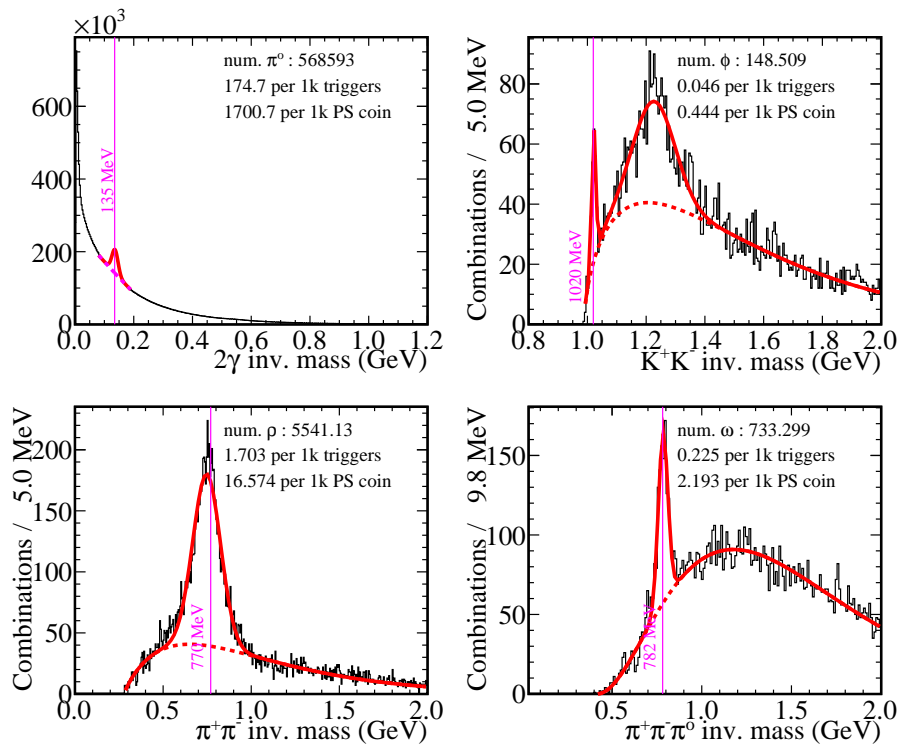


Figure 36: Invariant mass distributions showing π^0 , ω , ρ , and ϕ particles. These plots were generated online in about 1hr 40min by looking at roughly 2% of the data stream.

	2016	2017	2018
actual (raw data only)	0.624	0.914	3.107
model (raw data only)		0.863	3.172
actual (production data)	0.55	1.256	1.206

Table 4: GLUEX data volumes by year. All values are in petabytes (PB). Most years include two run periods. The line marked “model” gives calculated rates from the GLUEX Computing Model[86] based on the detector luminosity. “Raw data only” represents data generated by the DAQ system (not including the backup copy). “Production” represents all derived data including reconstructed values and ROOT trees.

1937 an LT0 tape system in the JLab Computer Center for long term storage. Two
1938 RAID servers, each with four partitions, were used for staging the data. The
1939 partition being written was rotated between runs to minimize head thrashing
1940 on disks by only reading partitions not currently being written. Partitions were
1941 kept at approximately 80% capacity and older files were deleted to maintain
1942 this level, allowing the monitoring farm easy access to files when the beam was
1943 down. A copy of the first three files ($\sim 1.5\%$) of each run was also kept on the
1944 online computers for direct access to samples from each run.

1945 The data volumes stored to tape are shown in Table 4 in units of petabytes
1946 (PB). Entries marked “actual” are values taken from the tape storage system.
1947 The line marked “model” comes from the GLUEX computing model[86].

1948 13. Event reconstruction

1949 GLUEX uses the computer center batch farm at JLab to perform data moni-
1950 toring, event reconstruction, and physics analyses. For data monitoring, de-
1951 tector hit occupancies, calibration and reconstruction quality, and experimental
1952 yields and resolutions, are analyzed for several physics channels. A subset of the
1953 data is monitored automatically as it is saved to tape. Every few weeks, moni-
1954 toring processes are launched on a subset of the data to study improvements from
1955 ongoing calibrations and reconstruction software improvements. The histograms
1956 produced by these monitoring jobs are displayed on a website and ROOT files
1957 are available for download, enabling the collaborators to easily study the quality
1958 of the data.

1959 Every few months, a major reconstruction launch over all of the data is
1960 performed, linking hits in the various detector systems to reconstruct particles
1961 in physics events. Monitoring plots from these launches are also published to
1962 the web. Finally, regular analysis launches over the reconstructed data are
1963 performed for the reactions requested by users on a web form. The results of
1964 these launches are saved in reaction-specific ROOT TTrees for further analysis.

1965 For all launches, the reconstruction is run in a multi-threaded mode to make
1966 efficient use of the available computing resources. Fig.37 shows the multi-
1967 threaded scaling from our monitoring launches. The program performs near
1968 the theoretical limit for jobs that use a number of threads that is less than or
1969 equal to the number of physical cores on the processor. By using hyperthreads,

1970 a smaller but still significant gain is achieved. All file outputs are written to a
1971 write-through cache system, which is ultimately backed up to tape.

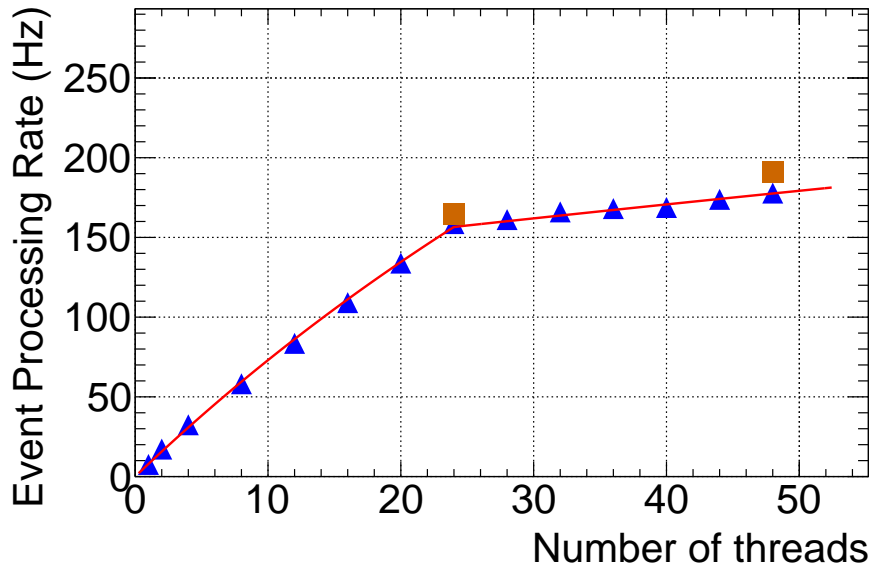


Figure 37: The scaling of program performance as a function of the number of processing threads. The computer used for this test consisted of 24 full cores (Intel x86.64) plus 24 hyperthreads. The orange squares are from running multiple processes, each with 12 threads.

1972 GLUEX Phase I has recorded 1400 separate physics-quality runs, with a
1973 total data footprint of about 3 petabytes. Data were saved in 19-GB files, with
1974 all runs consisting of multiple files (typically 100 or more per run). Fig. 38
1975 shows an overview of the different production steps for GLUEX data, which are
1976 described in more detail in the following subsections.

1977 13.1. Calibration

1978 During the acquisition of data, a unique run number is assigned to a period
1979 of data corresponding to less than about 2 hours of clock time, which may result
1980 in writing a couple hundred files. It is assumed that the detector changes very
1981 little during this period and therefore there will be no changes in the calibration
1982 constants. Two types of calibration procedures are used, depending on the
1983 complexity of the calibration procedures. Simple, well-understood calibrations
1984 such as timing alignment between individual channels and subdetectors or drift
1985 chamber gain and time-to-distance calibrations, can be performed with one file
1986 of data per run. These procedures are executed either in the online environment
1987 or on the batch farm, and can be repeated as needed following any improvements
1988 in reconstruction algorithms or other calibrations.

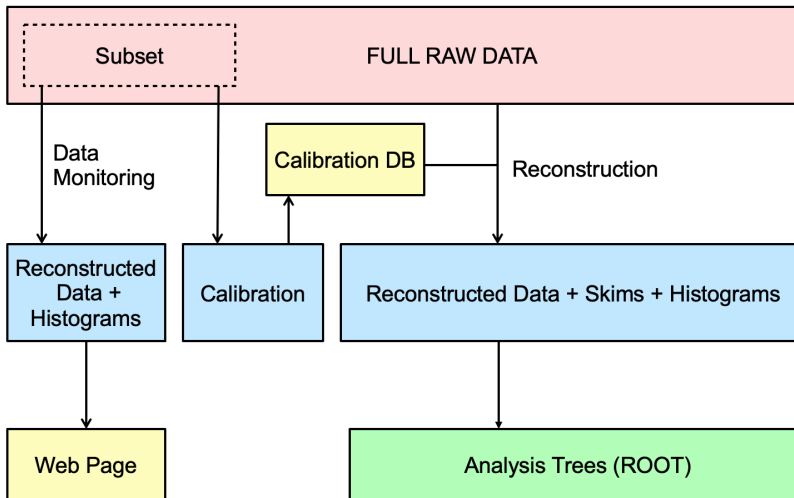


Figure 38: Production flowchart for GLUEX data, illustrating analysis steps.

1989 More complicated calibration procedures, such as calorimeter gain calibration
 1990 tion, require more data and are often iterative procedures, requiring several
 1991 passes through the data. The raw data are processed upon arrival on the batch
 1992 farm, resulting in histograms or in selected event data files in EVIO [87] or
 1993 ROOT-tree format. Many of these outputs require that charged particle tracks
 1994 are reconstructed. However, the computationally intensive nature of track re-
 1995 construction makes it a challenge to fully reconstruct all raw data immediately.
 1996 Therefore, the full suite of calibration procedures is only applied to 10 - 20% of
 1997 the data. Processing of the remaining data is mostly focused on separating out,
 1998 or “skimming,” events collected by calibration triggers.

1999 13.2. Monitoring

2000 In Fig. 38 the “FULL RAW DATA” box represents experimental data that
 2001 have been backed up to tape. The box labeled “subset” represents the first five
 2002 files of each run, which are run through offline monitoring processes. These
 2003 monitoring jobs are first processed during the run to check the quality of the
 2004 data, but are also processed after major changes to calibrations or software to
 2005 validate those changes. The resulting Reconstructed Events Storage (REST)
 2006 files and ROOT histogram files are used for checking the detector and recon-
 2007 struction performance.

2008 13.3. Reconstruction

2009 When the data have been sufficiently well calibrated, a full (production) pass
 2010 of the reconstructed software on the physics quality data is performed. In the
 2011 current total GLUEX data set, about 1400 runs were deemed “physics quality.”
 2012 The remaining runs were short runs related to engineering and commissioning

2013 tests of the experiment. The 1400 physics quality runs include the majority of
2014 the data recorded during the running period, representing about 3 petabytes.
2015 All these files were reconstructed using computing resources at several sites,
2016 equivalent to more than 20 million core-hours combined. This produced more
2017 than 500 terabytes of REST data files. The large reduction in size from collected
2018 event data to physics data files (about a factor of six) permits faster and more
2019 efficient physics analyses of the data.

2020 During the REST production, a series of detector studies were performed
2021 that required access to raw data and that would not be possible on the recon-
2022 structed data alone. Many improvements to software and detector calibration
2023 resulted from these studies. Similar studies can be made with simulated data
2024 to match and assess the detector acceptance.

2025 *13.4. Offsite reconstruction*

2026 Production processing of GLUEX data uses offsite high-performance com-
2027 puting resources in addition to the onsite computing farm at JLab, specifically,
2028 the National Energy Research Supercomputing Center (NERSC) and the Pitts-
2029 burgh Supercomputing Center (PSC). For NERSC, the total allocation used for
2030 the academic year 2018-2019 was 53M NERSC units, which was used to process
2031 70.5k jobs. This is equivalent to approximately 9M core-hours on a Intel x86_64
2032 processor. The jobs were run on NERSC's Cori II system, which is comprised of
2033 KNL (Knight's Landing) processors. The PSC allocation was awarded through
2034 the XSEDE⁶⁷ allocation system in the last quarter of calendar year 2019 for 5.9
2035 MSU. Only 0.85M SU were used in 2019 to run 7k jobs on the PSC Bridges
2036 system or about 10% of the number processed at NERSC. Figure 39 shows
2037 how the event processing rates scaled with the number of processing threads
2038 for both NERSC and PSC. Jobs run at both of those sites were assigned entire
2039 nodes so the number of processing threads used was equal to the total number
2040 of hardware threads.

2041 Container and distributed file system technologies were used for offsite pro-
2042 cessing. The software binaries as well as calibration constants, field maps, etc.
2043 were distributed using the CERN-VM-file system (CVMFS). The binaries were
2044 all built at JLab using a CentOS7 system. A very lightweight Docker con-
2045 tainer was made based on CentOS7 that had only a minimal number of system
2046 RPMs⁶⁸ installed. All other software, including third-party packages such as
2047 ROOT, were distributed via CVMFS. This meant changes to the container it-
2048 self were very rare (about once per year). The Docker container was pulled into
2049 NERSC's Shifter system without modification. The same container was used to
2050 create a Singularity container used at both PSC and on the Open Science Grid
2051 (OSG) for simulation jobs.

2052 Raw data were transferred from JLab to the remote sites using Globus⁶⁹,

⁶⁷<https://www.xsede.org>.

⁶⁸RedHat Package Management, https://access.redhat.com/documentation/en-us/red_hat_enterprise_linux/5/html/deployment_guide/ch-rpm

⁶⁹<https://opensciencegrid.org/technology/policy/globus-toolkit>.

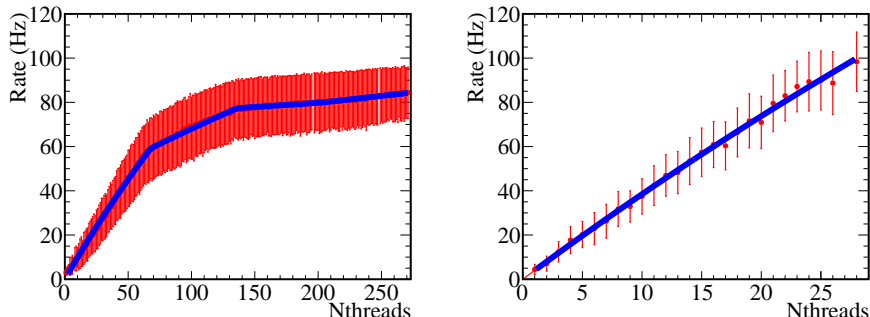


Figure 39: Event processing rate versus number of threads for reconstruction jobs on NERSC Cori II (left) and PSC Bridges (right). The slope changes in the NERSC plot are due to the KNL architecture, which had four hardware threads per core. For PSC Bridges, hyper-threading is disabled and the plot shows a single slope.

2053 which uses GridFTP. The Globus tasks were submitted and managed by the
 2054 SWIF2 workflow tool written by the JLab Scientific Computing group. SWIF2
 2055 was needed to manage the data retrieval from tape, for transfer to the remote
 2056 site, for submission of remote jobs, and for transfer of processed data back to
 2057 JLab. Disk space limitations at both JLab and the remote sites meant only a
 2058 portion of the data set could be on disk at any one time. Thus, SWIF2 had to
 2059 manage the jobs through all stages of data transfer and job submission.

2060 13.5. Analysis

2061 The full set of reconstructed (REST) data is too large to be easily handled by
 2062 individual analyzers. For that reason, a system was developed to analyze data
 2063 at JLab and extract reaction-specific ROOT trees. This step is represented by
 2064 the right-hand green box at the bottom of Fig. 38.

2065 Users can specify individual reactions via a web interface. Periodically, the
 2066 submitted reactions are downloaded into a configuration file, which steers the
 2067 analysis launch. For each reaction, the GLUEX analysis library inside the JANA
 2068 framework creates possible particle combinations from the reconstructed particle
 2069 tracks and showers saved in the REST format. Common selection criteria
 2070 are applied for exclusivity and particle identification before performing a kinematic
 2071 fit, using vertex and four-momentum constraints. Displaced vertices and
 2072 inclusive reactions are also supported. Objects representing successful particle
 2073 combinations (e.g. $\pi^0 \rightarrow \gamma\gamma$) and other objects are managed in memory pools,
 2074 and can be reused by different channels to reduce the overall memory footprint
 2075 of the process. With this scheme, up to one hundred different reactions can be
 2076 combined into one analysis launch processing the reconstructed data.

2077 If the kinematic fit converged for one combination of tracks and showers, the
 2078 event is stored into a reaction-specific but generic ROOT tree, made accessible
 2079 to the whole collaboration. The size of the resulting ROOT trees for the full

2080 data set strongly depends on the selected reaction, but is usually small enough
2081 to be copied to the user's home institution for a more detailed analysis.

2082 **14. Monte Carlo simulation**

2083 The detailed simulation of events in the Hall-D beamline and GLUEX de-
2084 tector is performed with a GEANT-based software package. The package was
2085 originally developed within the GEANT3 framework [88] and then migrated
2086 to the GEANT4 framework [89, 90]. The simulation framework uses the same
2087 geometry definitions and magnetic field maps as used in reconstruction. The
2088 geometry includes the full photon beamline, starting at the radiator and ending
2089 at the photon beam dump. Both internal and external event generators are sup-
2090 ported by the framework. Internal sources include the coherent bremsstrahlung
2091 source and the single particle gun. Events read from any number of external
2092 generators are also supported. These input events specify one or more primary
2093 vertices to be simulated, which are randomized within the hydrogen target with
2094 timing that matches the RF structure of the beam.

2095 The Monte Carlo data flow is presented in Fig. 40. Events of interest are
2096 generated using either an internal or user-supplied event generator. The in-
2097 put event specification is fed to the Hall D GEANT simulation code, either
2098 *hdgeant* or *hdgeant4*, which tracks the particles through the experimental setup
2099 and records the signals they produce in the active elements of the detector.
2100 Behavior of the simulation is conditioned by a run number, which corresponds
2101 to a particular set of experimental conditions: beam polarization and intensity,
2102 beamline and detector geometry, magnetic field maps, etc. All this information
2103 is read by the simulation at run-time from the calibrations database, which
2104 functions as the single source for all time-dependent geometry, magnetic field,
2105 and calibration data relevant to the simulation.

2106 Events written by the simulation are processed by the detector response
2107 package *mcsmeas*. It applies corrections to the simulated hits to account for
2108 detector system inefficiencies and resolution, and overlays additional hits from
2109 uncorrelated background events. Loss of hits from detector channels, multi-hit
2110 truncation, and electronic deadtime are also applied at this step. Information
2111 needed for this processing comes from the databases for calibrations and run-
2112 conditions, and from files containing real backgrounds sampled using random
2113 triggers. Events emerging from the smearing step are deemed to be faithful
2114 representations of what the detector would have produced for the given run in
2115 response to the specified input. These Monte Carlo events are then processed
2116 with the same reconstruction software as used for the real events, and the output
2117 is saved to a REST file. These REST files are then made available for physics
2118 analysis.

2119 *14.1. Geometry specification*

2120 The geometry and material descriptions for the experiment are common
2121 across simulation and reconstruction, residing in a family of xml files that follow

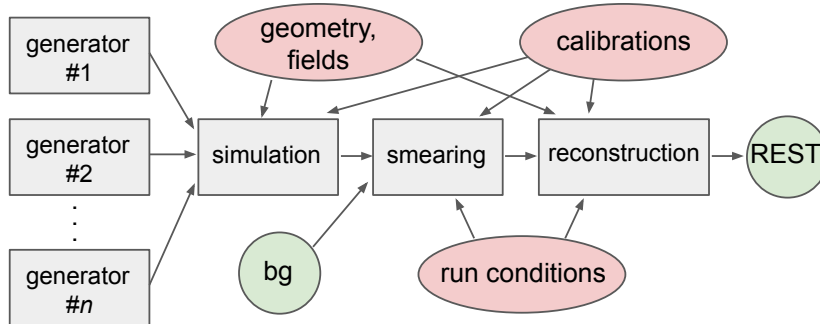


Figure 40: The Monte Carlo data flow from event generators through physics analysis REST files. The ovals represent databases containing tables indexed by run number, providing a common configuration for simulation, smearing, and reconstruction. Background events represented by the circle marked bg are real events collected using a random trigger, which are overlaid on the simulated events to account for pile-up in the Monte Carlo.

2122 a common schema called the Hall D Detector Specification, or *HDDS* [91, 92].
 2123 Run-specific variations of the geometry xml records are maintained in the cali-
 2124 bration database. The geometry and magnetic field map are also maintained in
 2125 the calibration database.

2126 The output events from the simulation are written as a data stream, which
 2127 may either be piped directly into the next step of the Monte Carlo pipeline
 2128 or saved to a file. Events are passed between all stages of the Monte Carlo
 2129 processing pipeline, shown in Fig. 40, using the common data format of the
 2130 Hall-D Data Model, HDDM [93]. HDDM is used for all intermediate input and
 2131 output event streams.

2132 14.2. Event generators

2133 Simulation starts with the generation of events, which can be specific parti-
 2134 cles or reactions, or simply unbiased background events. A common toolset has
 2135 been developed to minimize redundancy. These tools include standard methods
 2136 to generate the distributions of primary photon beam energies and polarization.
 2137 An output interface is used to produce files suitable as input to the GEANT
 2138 simulation.

2139 The photon beam energy distribution can be produced using a coherent
 2140 bremsstrahlung generator that accounts for the physical properties of the ra-
 2141 diator and the photon beamline. This generator allows the user to select the
 2142 orientation of the diamond radiator, and then calculates the linear polarization
 2143 for each photon. Photons can also be generated according to the spectrum mea-
 2144 sured in the pair spectrometer during any actual data run by interfacing to the
 2145 calibration data base. Here the user inputs the degree of linear polarization and
 2146 the orientation. Finally, the user can provide a histogram of the photon energy
 2147 spectrum and a second one of the degree of polarization to be used to generate
 2148 the photon beam.

2149 One of the first generators was used to simulate the total photoproduction
2150 cross section. It is currently used to study backgrounds to physics reactions
2151 as well as develop analysis tools for extracting signals. This event generator,
2152 called *bggen*, is based on Pythia [94], and includes additions that describe the
2153 low-energy photoproduction cross sections. Other generators are tied to specific
2154 reactions, where the generator needs to describe the underlying physics.

2155 14.3. HDGEANT

2156 Both GEANT3 and GEANT4 versions are available for simulation of the
2157 experiment. Both versions have been tuned to reproduce the behavior of the
2158 experiment, but there are some differences arising from how the two versions
2159 decide when to stop tracking particles. In general, the simulation mimics the
2160 running conditions found across a range of runs, typically a large part of a single
2161 run period. The output from GEANT contains both hit times and energies
2162 deposited in detector volumes.

2163 14.4. Detector response

2164 Converting time and energy deposits coming from GEANT into electronic
2165 detector responses that match the readout from the experiment is carried out
2166 by the detector response package *mcsmeas*. The output of this digitization is
2167 identical to the real data with the exception that the so-called *truth information*
2168 about the data is retained to allow detailed performance studies. In addition
2169 to the digitization, at this stage the run-dependent efficiency effects are applied
2170 to the data, including both missing electronic channels and reduced efficiency
2171 of other channels. Additional smearing of some signals is also applied here to
2172 better match the performance of the Monte Carlo to data.

2173 The *mcsmeas* package also folds measured backgrounds into the data stream.
2174 During regular data collection, random triggers are collected concurrently with
2175 data taking (see Section 9). These are separated from the actual data and used
2176 to provide experimental background signals in the Monte Carlo, with rates based
2177 on the actual beam fluxes in the experiment.

2178 14.5. Job submission

2179 A large number of experimental conditions need to be matched in simulated
2180 data. The *MCWrapper* tool was developed to streamline the input specifica-
2181 tions, implement consistency with corresponding data reconstruction, seamlessly
2182 access computer offsite resources, and produce Monte Carlo samples in propor-
2183 tion to the actual data taken. The goal is to model the differences between runs
2184 and provide a simulated data set, comparable to the real data. The primary
2185 system used for this phase is the Open Science Grid (OSG) in order to lever-
2186 age resources in addition to the local JLab computing farm. Many automated
2187 checks are made to avoid flawed submission, and all aspects of the requests and
2188 jobs are monitored during running. Once completed, *MCWrapper* checks for
2189 expected output files to be returned as if the jobs were run on the JLab farm. If
2190 expected files are not found the system will automatically submit a replacement

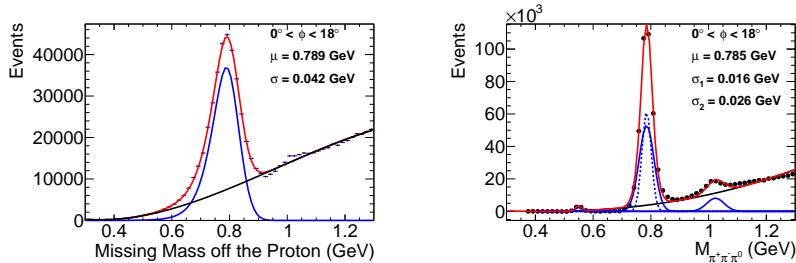


Figure 41: Reconstructed mass distributions for the reaction $\gamma p \rightarrow p\pi^0\pi^\pm(\pi^\mp)$ for a bin in ϕ . (Left) Distribution of the missing mass off the proton. (Right) Invariant mass distribution for the $\pi^+\pi^-\pi^0$ system. The blue curves show the resonant contributions, the black curve shows the polynomial backgrounds, and the red curve shows the sum. (Color online)

2191 job. Once the jobs are verified completed and all data from the request have
 2192 been properly moved, the user receives an automated email alerting them that
 2193 their request has been fulfilled and providing the location where the user can
 2194 access the event sample.

2195 Users are able to monitor and control their simulations via an online dash-
 2196 board. The *MCWrapper* dashboard gives information about active projects and
 2197 allows users (or administrators) to interact with their requests. Users may cancel,
 2198 suspend, or declare projects complete. Detailed information is presented
 2199 about the individual jobs, such as where the jobs are being run, basic usage
 2200 statistics, and current status. This information gives individuals a near real-time
 2201 look into the production of their Monte Carlo samples.

2202 15. Detector performance

2203 The capability of the GLUEX detector in reconstructing charged and neutral
 2204 particles and assembling them into fully reconstructed events has been studied
 2205 in data and simulation using several photoproduction reactions. The results of
 2206 these studies are summarized in this section.

2207 15.1. Charged-particle reconstruction efficiency

2208 The track reconstruction efficiency was estimated by analyzing $\gamma p \rightarrow p\omega$,
 2209 $\omega \rightarrow \pi^+\pi^-\pi^0$ events, where the proton, the π^0 , and one of the charged pi-
 2210 ons were used to predict the three-momentum of the other charged pion. Two
 2211 methods were used to calculate this efficiency, $\varepsilon = N_{found}/(N_{found} + N_{missing})$.
 2212 Events for which no track was reconstructed in the predicted region of phase
 2213 space contributed to $N_{missing}$, while events where the expected track was recon-
 2214 structed contributed to N_{found} . For the first method, the ω yields for N_{found}
 2215 and $N_{missing}$ were estimated from the missing mass off the proton; for the sec-
 2216 ond method, the invariant mass of the $\pi^+\pi^-\pi^0$ system was used to find N_{found} .
 2217 This analysis was performed for individual bins of track momentum, θ , and ϕ .

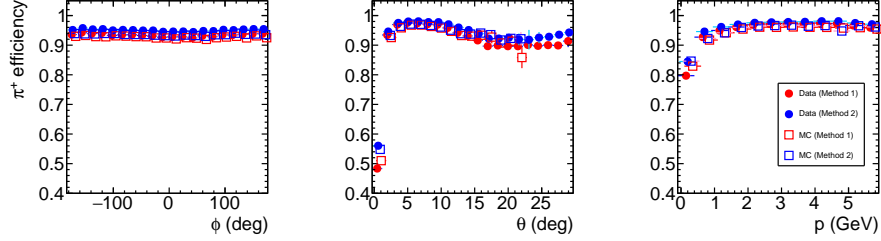


Figure 42: Tracking efficiency for π^+ tracks, determined by data and simulation using two methods. (Color online)

2218 Examples of mass histograms for a typical bin in ϕ are shown in Fig. 41. The
 2219 exercise was repeated for a sample of ω Monte Carlo events. A comparison of
 2220 the efficiency for pion reconstruction derived from the two methods for both
 2221 Monte Carlo and experimental data is shown in Fig. 42. The efficiencies for
 2222 Monte Carlo and experimental data agree to within 5%.

2223 While this reaction only allows the determination of track reconstruction
 2224 efficiencies for $\theta < 30^\circ$, this covers the majority of charged particles produced
 2225 in GLUEX due to its fixed-target geometry. Other reactions are being studied
 2226 to determine the efficiency at larger angles.

2227 15.2. Photon efficiency

2228 Photon-reconstruction efficiency has been studied using different methods for
 2229 the FCAL and BCAL. In the FCAL, absolute photon reconstruction efficien-
 2230 cies have been determined using the “tag-and-probe” method with a sample
 2231 of photons from the reaction $\gamma p \rightarrow \omega p$, $\omega \rightarrow \pi^+\pi^-\pi^0$, $\pi^0 \rightarrow \gamma(\gamma)$, where one
 2232 final photon is allowed but not required to be reconstructed. The yields with
 2233 and without the reconstructed photon are determined using two methods. In
 2234 the first method, the ω yield is determined from the missing-mass spectrum,
 2235 $M_X(\gamma p \rightarrow pX)$, selecting on whether only one or both reconstructed photons
 2236 are consistent with a final-state π^0 . In the second method, the count when both
 2237 photons are found is determined from the ω yield from the fully reconstructed
 2238 invariant mass $M(\pi^+\pi^-\gamma\gamma)$. If the photon is not reconstructed, the ω yield
 2239 is determined by a fit to the distribution of the missing mass off the proton.
 2240 Both methods yield consistent results, with a reconstruction efficiency generally
 2241 above 90%, and within 5% or less agree with the efficiencies determined from
 2242 simulation.

2243 A relative photon efficiency determination has been performed using $\pi^0 \rightarrow$
 2244 $\gamma\gamma$ decays, which spans the full angular range detected in GLUEX. A sample of
 2245 fully reconstructed $\gamma p \rightarrow \pi^+\pi^-\pi^0 p$ events were inspected, taking advantage of
 2246 the $\pi^0 \rightarrow \gamma\gamma$ decay isotropy in the center-of-mass frame. Thus, any anisotropy
 2247 indicates an inefficiency in the detector. Results from this analysis are illustrated

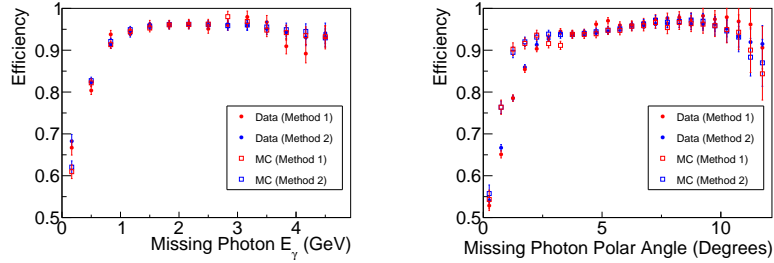


Figure 43: Photon reconstruction efficiency in FCAL determined from $\gamma p \rightarrow \omega p$, $\omega \rightarrow \pi^+\pi^-\pi^0$, $\pi^0 \rightarrow \gamma(\gamma)$ as a function of (left) photon energy and (right) photon polar angle. Good agreement between data and simulation is observed in the fiducial region $\theta = 2^\circ - 10.6^\circ$. (Color online)

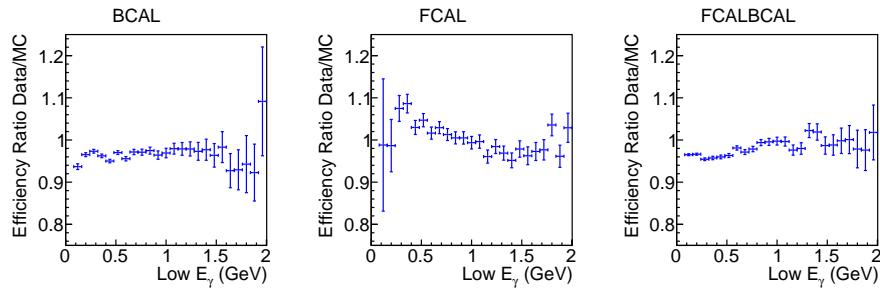


Figure 44: Ratios of relative photon reconstruction efficiency between data and simulation determined from $\pi^0 \rightarrow \gamma\gamma$ decays in $\gamma p \rightarrow \pi^+\pi^-\pi^0 p$ events. The efficiency ratios are shown for the cases where (left) both photons were measured in the BCAL, (middle) both photons were measured in the FCAL, and (right) one photon was measured in the BCAL and the other in the FCAL.

2248 in Fig. 44. Generally, this relative efficiency is above 90%, and agrees within
 2249 5% of that determined from simulation.

2250 The models for the simulated response of both calorimeters are being up-
 2251 dated, and the final agreement between photon efficiency determined in data
 2252 and simulation is expected to improve.

2253 Detailed studies of detector performance determined the standard fiducial
 2254 region for most analyses to be $\theta = 2^\circ - 10.6^\circ$ and $\theta > 11.3^\circ$. These requirements
 2255 avoid the region dominated by beam-related backgrounds at small θ and the
 2256 transition region between the BCAL and FCAL, where shower reconstruction
 2257 is difficult.

2258 15.3. Kinematic fitting

2259 Kinematic fitting is a powerful tool to improve the resolution of measured
 2260 data and to distinguish between different reactions. In GLUEX, this method
 2261 takes advantage of the fact that the initial state is very well known, with the

2262 target proton at rest, and the incident photon energy measured with very high
 2263 precision ($< 0.1\%$). This knowledge of the initial state gives substantial im-
 2264 provements in the kinematic quantities determined for exclusive reactions. The
 2265 most common kinematic fits that are performed are those that impose energy-
 2266 momentum conservation between the initial and final-state particles. Additional
 2267 optional constraints in these fits are for the four-momenta of the daughters of
 2268 an intermediate particle to add up to a fixed invariant mass, and for all the
 2269 particles to come from a common vertex (or multiple vertices, in the case of
 2270 reactions containing long-lived, decaying particles).

2271 To illustrate the performance of the kinematic fit, we use a sample of $\gamma p \rightarrow$
 2272 ηp , $\eta \rightarrow \pi^+ \pi^- \pi^0$ events selected using a combination of standard particle iden-
 2273 tification and simple kinematic selections. The use of the kinematic fit im-
 2274 proves the η -mass resolution from 2.6 MeV to 1.7 MeV, which is typical of
 2275 low-multiplicity meson production reactions. The quality of the kinematic fit is
 2276 determined using either the probability calculated from the χ^2 of the fit and the
 2277 number of degrees-of-freedom or the χ^2 of the fit itself. The distributions of the
 2278 kinematic fit χ^2 and probability are illustrated in Fig. 45 for both reconstructed
 2279 and simulated data. The agreement between the two distributions is good for
 2280 small χ^2 (large probability), and flat over most of the probability range, indicat-
 2281 ing good overall performance for most signal events. The disagreement between
 2282 the two distributions at larger χ^2 (probability < 0.2) is due to a combination of
 2283 background events and deficiencies in the modelling of poorly measured events
 2284 with large resolution.

2285 The performance of the reconstruction algorithms and kinematic fit can be
 2286 studied through investigating the “pull” distributions, where the pull of a vari-
 2287 able x is defined by comparing its measured values and uncertainties and those
 2288 resulting from the kinematic fit as

$$\text{pull}_x = \frac{x_{\text{fitted}} - x_{\text{measured}}}{\sqrt{\sigma_{x,\text{measured}}^2 - \sigma_{x,\text{fitted}}^2}}. \quad (1)$$

2289 If the parameters and covariances of reconstructed particles are Gaussian, are
 2290 measured accurately, and the fit is performing correctly, then these pull values
 2291 are expected to have a Gaussian distribution centered at zero with a width σ
 2292 of 1. If the pull distributions are not centered at zero, this is an indication that
 2293 there is a bias in the measurements or the fit. If σ varies from unity, this is an
 2294 indication that the covariance matrix elements are not correctly estimated.

2295 As an example, the pull distributions for the momentum components of the
 2296 π^- in reconstructed $\gamma p \rightarrow \eta p$, $\eta \rightarrow \pi^+ \pi^- \pi^0$ events are shown in Fig. 46.
 2297 Both real and simulated data have roughly Gaussian shapes with similar widths.
 2298 More insight into the stability of the results of the kinematic fit can be found
 2299 by studying the variation of the means and widths of the fit distributions as
 2300 a function of the fit probability. The results of such a study are summarized
 2301 in Fig. 47, where broad agreement between the results from real and simulated
 2302 data is seen. The means of the pull distributions are generally around zero,
 2303 except for p_x with a mean of roughly -0.1 , and the widths within about 20% of

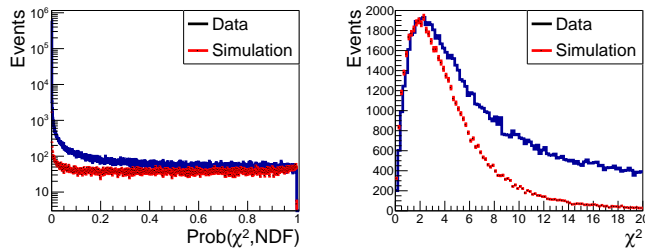


Figure 45: Distribution of kinematic fit (left) probability and (right) χ^2 for reconstructed $\gamma p \rightarrow \eta p$, $\eta \rightarrow \pi^+ \pi^- \pi^0$ events in data and simulation. Both distributions agree reasonably for well-measured events, and diverge due to additional background in data and differences in modeling poorly-measured events. (Color online)

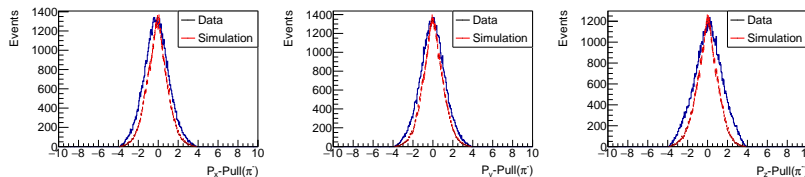


Figure 46: Pull distributions for momentum components of the π^- from reconstructed $\gamma p \rightarrow \eta p$, $\eta \rightarrow \pi^+ \pi^- \pi^0$ events in data and simulation for events with fit probability > 0.01 : (left) p_x , (center) p_y , (right) p_z . (Color online)

2304 unity. This level of performance and agreement between data and simulation is
 2305 acceptable for the initial analysis of data, where very loose cuts on the kinematic
 2306 fit χ^2 are performed, and steady improvement in the modeling of the covariance
 2307 matrices of reconstructed particles is expected to continue.

2308 15.4. Invariant-mass resolution

2309 The invariant-mass resolution for resonances depends on the momenta and
 2310 angles of their decay products. This resolution has been studied using several
 2311 different channels, which are illustrated in Figs. 48 and 50. A typical meson
 2312 production channel including both charged particles and photons, $\omega \rightarrow \pi^+ \pi^- \pi^0$
 2313 from $\gamma p \rightarrow \omega p$, is shown in the left panel of Fig. 48. The distribution shows
 2314 the strong peak due to ω meson production. Other structures are also seen,
 2315 such as peaks corresponding to the production of η and ϕ mesons. The ω peak
 2316 resolution obtained is 26.1 MeV when using only the reconstructed particle 4-
 2317 vectors, and improves to 16.4 MeV after a kinematic fit. The invariant-mass
 2318 distribution of $\pi^+ \pi^-$ from $\gamma p \rightarrow K_S K^+ \pi^- p$, $K_S \rightarrow \pi^+ \pi^-$ exhibits the peak
 2319 due to $K_S \rightarrow \pi^+ \pi^-$ decays (right panel of Fig. 48). The K_S peak resolution is
 2320 17.0 MeV using only the reconstructed charged particle 4-vectors, and improves
 2321 to 8.6 MeV after a kinematic fit imposing energy and momentum conservation.

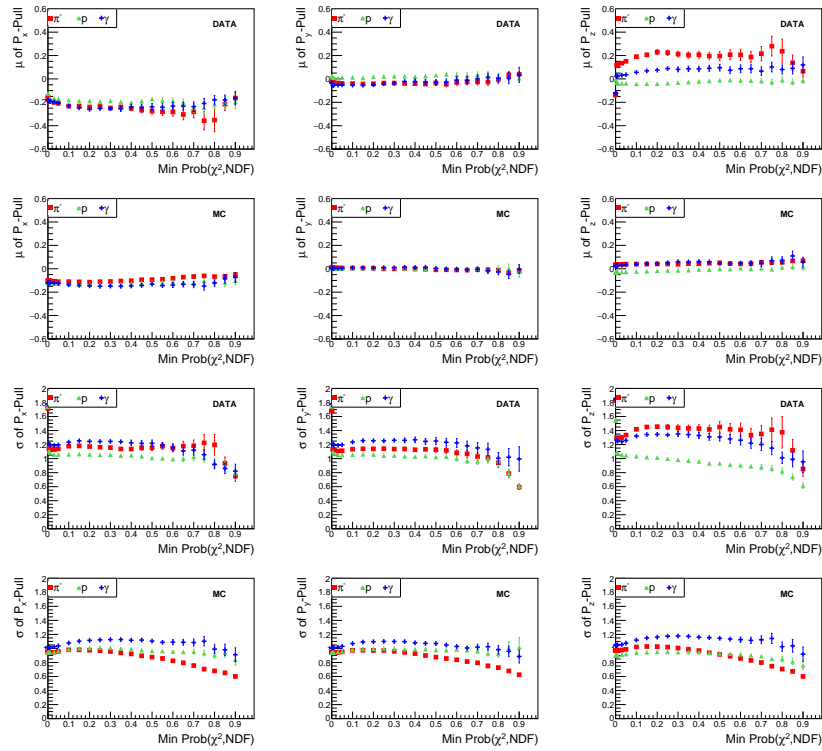


Figure 47: Pull means (top) and sigmas (bottom) for the momentum components of each particle as a function of the minimum probability required of the fit from reconstructed $\gamma p \rightarrow \eta p, \eta \rightarrow \pi^+ \pi^- \pi^0$ events. (Color online)

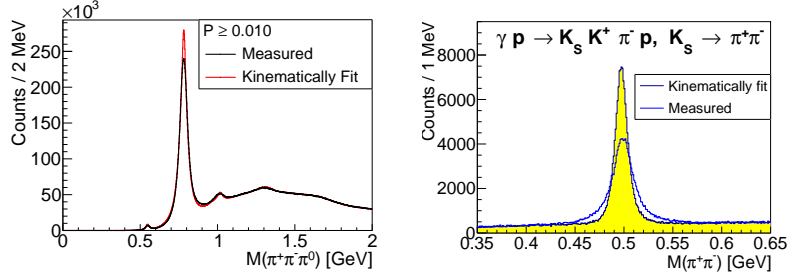


Figure 48: (Left) $\pi^+\pi^-\pi^0$ invariant-mass distribution from $\gamma p \rightarrow \pi^+\pi^-\pi^0 p$ (Right) $\pi^+\pi^-$ invariant mass distribution from $\gamma p \rightarrow K_S K^+ \pi^- p$, $K_S \rightarrow \pi^+\pi^-$. (Color online)

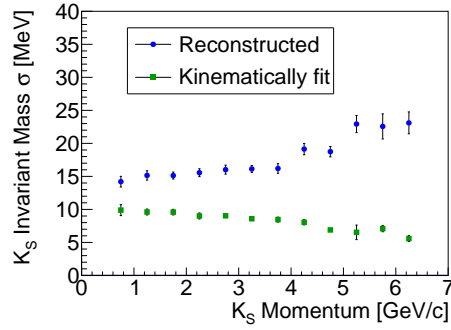


Figure 49: $K_S \rightarrow \pi^+\pi^-$ invariant mass resolution for the events shown in Fig. 48, as a function of K_S momentum, both before and after a kinetic fit, which constrains energy and momentum conservation. (Color online)

2322 The dependence of the $K_S \rightarrow \pi^+\pi^-$ invariant-mass resolution as a function of
 2323 K_S momentum is shown in Fig. 49, both before and after an energy/momentum-
 2324 constraint kinematic fit.

2325 The invariant mass of $\Lambda^0\pi^-$ from $\gamma p \rightarrow K^+K^+\pi^-\pi^-p$ is shown in the left
 2326 panel of Fig. 50, illustrating the peak due to $\Xi^- \rightarrow \pi^-\Lambda^0$, $\Lambda^0 \rightarrow p\pi^-$. The Ξ^-
 2327 peak resolution obtained is 7.3 MeV when using only the reconstructed charged
 2328 particle 4-vectors, and improves to 4.6 MeV after a kinematic fit imposing en-
 2329 ergy and momentum conservation and the additional constraint that the mass
 2330 of the $p\pi^-$ pairs must be that of the Λ^0 mass. The e^+e^- invariant mass distri-
 2331 bution from kinematically fit $\gamma p \rightarrow e^+e^-p$ events is shown in the right panel of
 2332 Fig. 50, illustrating the peak due to $J/\psi \rightarrow e^+e^-$. The resolution of the peak is
 2333 13.7 MeV.

2334 15.5. Particle identification

2335 Particle identification in GLUEX uses information from both energy loss in
 2336 different detector systems and time-of-flight measurements. This information

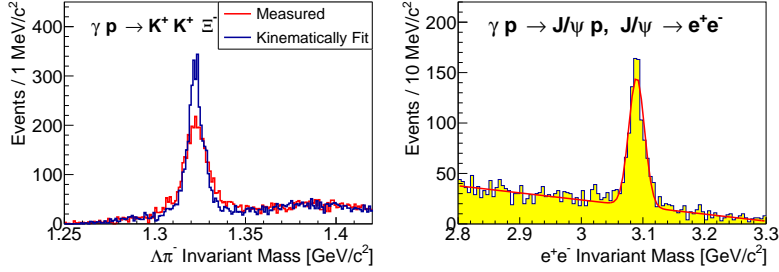


Figure 50: (Left) $\Lambda^0\pi^-$ invariant mass distribution from $\gamma p \rightarrow K^+K^+\pi^-\pi^-p$. (Right) e^+e^- invariant mass distribution from kinematically fit $\gamma p \rightarrow e^+e^-p$ events. (Color online)

2337 can be used for identification in several ways. The simplest method is to apply
 2338 selections directly on the relevant PID variables. To include detector resolution
 2339 information, one can create a χ^2 variable comparing a measured value to the
 2340 expected value for a particular hypothesis, that is

$$\chi^2(p) = \left(\frac{X(\text{measured}) - X(\text{expected})_p}{\sigma_X} \right)^2 \quad (2)$$

2341 where X is the given PID variable, p is the particle hypothesis, and σ_X is the
 2342 resolution of this variable. Multiple PID variables can be combined into one
 2343 probability, or a figure-of-merit. Standard, loose selections on time-of-flight and
 2344 energy loss are sufficient for initial physics analyses, while the performance of
 2345 more complicated selections is being actively studied.

2346 At sufficiently large θ , the energy loss for charged particles in the central
 2347 drift chamber dE/dx can be used. Fig. 51 illustrates these distributions for
 2348 positively charged particles, showing a clear separation of pions and protons
 2349 in the momentum range $\lesssim 1$ GeV. The dE/dx resolution is approximately 27%,
 2350 with the separation between the pion and proton bands dropping from about 8σ
 2351 at $p = 0.5$ GeV/ c to about 2σ at $p = 1.0$ GeV/ c , with both bands fully merged
 2352 by $p = 1.5$ GeV/ c .

2353 The primary means of particle identification is through time-of-flight mea-
 2354 surements, and information from several sources is combined to make the most
 2355 accurate determination. The RF reference signal from the accelerator is used to
 2356 define the time when each photon bunch enters the target. The reconstructed
 2357 final-state particles are used to determine which photon bunch most likely gener-
 2358 ated the detected reaction, with the primary determination coming from the
 2359 signals from the Start Counter associated with the charged particle tracks. The
 2360 photon bunch determination has a resolution of < 10 ps. Each charged par-
 2361 ticle is associated with additional timing information based on the hit in the
 2362 highest resolution detector (for example the BCAL or TOF). The flight time
 2363 to this measured hit t_{meas} relative to the time of the photon bunch that gener-
 2364 ated the event t_{RF} can be used to distinguish between particles of different
 2365 mass. Two common variables that are used are the velocity (β) determined

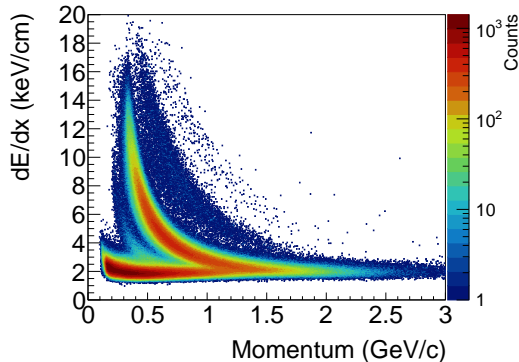


Figure 51: CDC energy loss (dE/dx) for positively charged particles that have at least 20 hits in the detector, as a function of measured particle momentum. The band corresponding to protons curves upwards, showing a larger energy loss than pions and other lighter particles at low momentum. The two bands show a clear separation for momenta $\gtrsim 1$ GeV. A faint kaon band can be seen between them.

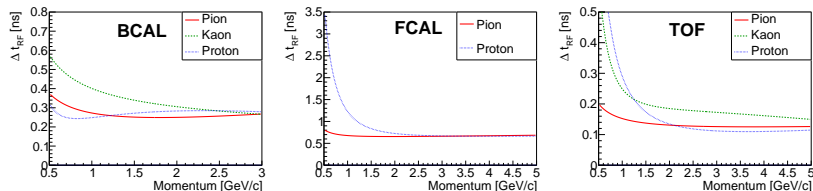


Figure 52: Resolution as a function of particle momentum for Δt_{RF} in various subdetectors: (left) BCAL, (center) FCAL, (right) TOF (Color online)

2366 using the measured time-of-flight and the momentum of the particle, and Δt_{RF} ,
 2367 the difference between the measured and RF times after they both have been
 2368 extrapolated back to the center of the target, assuming some particle-mass hy-
 2369 pothesis. An example of the separation between different particle types can be
 2370 seen in Fig. 29. The loose selections used for initial analyses of this data placed
 2371 on the Δt_{RF} distributions and the momentum dependence of the resolution of
 2372 this variable in different detectors are shown in Fig. 52. Requiring reconstructed
 2373 particles to have $\Delta t_{\text{RF}} \lesssim 1 - 2$ ns has been found to be sufficient for analyses
 2374 of high-yield channels which are the focus of initial analysis. The study of the
 2375 selections required for more demanding channels is ongoing.

2376 Electrons are identified using the ratio of their energy loss in the electromag-
 2377 netic calorimeters E to the momentum reconstructed in the drift chambers p .
 2378 This E/p ratio should be approximately unity for electrons and less for hadrons.
 2379 The overall distributions of this variable are illustrated in Fig. 53. Other vari-
 2380 ables, such as the shape of the showers generated by the charged particles in
 2381 the calorimeter, promise to provide additional information to separate electron

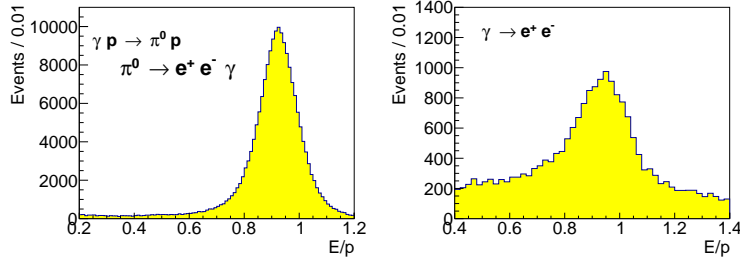


Figure 53: Electron identification in the calorimeters is performed using the E/p variable, the ratio of the energy loss in the electromagnetic calorimeters (E) to the momentum reconstructed in the drift chambers (p). Left) This distribution was obtained using e^\pm showers reconstructed in the FCAL from the reaction $\gamma p \rightarrow \pi^0 p$, $\pi^0 \rightarrow e^+ e^- \gamma$. Right) e^\pm showers reconstructed in the BCAL from photon conversions.

2382 and hadron showers.

2383 16. Summary and outlook

2384 We have presented the design, construction, and performance, of the beam-
 2385 line and detector of the GLUEX experiment in Hall D at Jefferson Lab during
 2386 its first phase of operation. The experiment operated routinely at an incident
 2387 photon flux of 2×10^7 photons/s in the coherent peak with an open trigger,
 2388 taking data at 40 kHz, and recording 600 MB/s to tape with live time >95%.
 2389 During this period the experiment accumulated 121.4 pb^{-1} in the coherent peak
 2390 and 319.4 pb^{-1} total for $E_\gamma > 8.1 \text{ GeV}$. Data were collected in two sets of or-
 2391 thogonal linear polarizations of the incident photons, with $\sim 23\%$ of the data in
 2392 each of the four orientations. The remaining $\sim 11\%$ was collected with unpolar-
 2393 ized photons. Approximately 270 billion triggers were accumulated during this
 2394 period, as shown in Fig. 54.

2395 The operational characteristics of the charged and neutral particle detectors,
 2396 trigger, DAQ, online and offline systems have been verified, and individual com-
 2397 ponents performed as designed. The detector is able to reconstruct exclusive
 2398 final states, reconstruction efficiencies have been determined, and Monte Carlo
 2399 simulations compare well with experimental data. The infrastructure is in place
 2400 to process our high volume of data both on the JLab computing farm as well
 2401 on other offsite facilities, providing the ability to process the data in a timely
 2402 fashion.

2403 Future running will include taking data at higher luminosity and with im-
 2404 proved particle identification capability. The GLUEX experiment has already
 2405 implemented the necessary infrastructure to allow the experiment to operate at
 2406 a flux of 5×10^7 photons/s in the coherent peak for the upcoming run periods

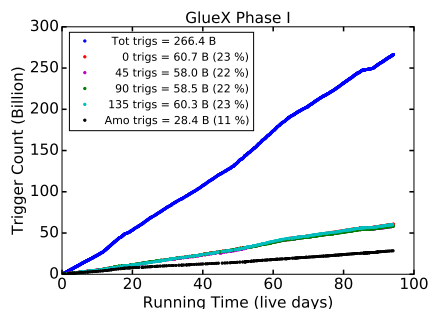


Figure 54: Plot of integrated number of triggers versus the number of live days in 2017 and 2018. The legend provides the number of triggers for the four diamond orientations relative to the horizontal (0, 45, 90, 135°) and the amorphous radiator. The trigger curves of the four diamond configurations fall on top of one another, as we attempted to match the amount of data taken for each configuration. (Color online)

2407 and has added a new DIRC detector⁷⁰ to extend particle identification of kaons
 2408 to higher momenta.

2409 17. Acknowledgments

2410 We gratefully acknowledge the outstanding efforts of technical support at
 2411 all the collaborating institutions and the support groups at Jefferson Lab that
 2412 completed the assembly, installation, and maintenance of the detector. We ac-
 2413 knowledge the contributions of D. Bennett, M. Lara, A. Subedi and P. Smith
 2414 to the construction and commissioning of the Forward Calorimeter. We thank
 2415 E.C. Aschenauer, G. Young and all members of the JLab 12 GeV Project for
 2416 guidance and direction during the design and construction phases of the project.
 2417 This work was supported in part by the U.S. Department of Energy, the U.S.
 2418 National Science Foundation, the Natural Sciences and Engineering Research
 2419 Council of Canada (NSERC), the German Research Foundation, Forschungszen-
 2420 trum Jülich GmbH, GSI Helmholtzzentrum für Schwerionenforschung GmbH,
 2421 the Russian Foundation for Basic Research, the UK Science and Technology
 2422 Facilities Council, the Chilean Comisión Nacional de Investigación Científica y
 2423 Tecnológica, the National Natural Science Foundation of China, and the China
 2424 Scholarship Council. This material is based upon work supported by the U.S.
 2425 Department of Energy, Office of Science, Office of Nuclear Physics under con-
 2426 tract DE-AC05-06OR23177.

⁷⁰Four “bar boxes” from the BaBar DIRC[95] detector have been installed and tested.

2427 **References**

- 2428 [1] V. Crede, C. A. Meyer, The Experimental Status of Glueballs, *Prog. Part.*
2429 *Nucl. Phys.* 63 (2009) 74–116. [arXiv:0812.0600](https://arxiv.org/abs/0812.0600), [doi:10.1016/j.ppnp.](https://doi.org/10.1016/j.ppnp.2009.03.001)
2430 [2009.03.001](https://doi.org/10.1016/j.ppnp.2009.03.001).
- 2431 [2] C. A. Meyer, Y. Van Haarlem, The Status of Exotic-quantum-number
2432 Mesons, *Phys. Rev. C* 82 (2010) 025208. [arXiv:1004.5516](https://arxiv.org/abs/1004.5516), [doi:10.1103/](https://doi.org/10.1103/PhysRevC.82.025208)
2433 [PhysRevC.82.025208](https://doi.org/10.1103/PhysRevC.82.025208).
- 2434 [3] C. A. Meyer, E. S. Swanson, Hybrid Mesons, *Prog. Part. Nucl. Phys.* 82
2435 (2015) 21–58. [doi:10.1016/j.ppnp.2015.03.001](https://doi.org/10.1016/j.ppnp.2015.03.001).
- 2436 [4] The GlueX Collaboration, The GlueX Experiment in Hall D, GlueX Project
2437 Overviews ([hyperlink](#)) (2010).
- 2438 [5] C. W. Leemann, D. R. Douglas, G. A. Krafft, The Continuous Electron
2439 Beam Accelerator Facility: CEBAF at the Jefferson Laboratory, *Ann.*
2440 *Rev. Nucl. Part. Sci.* 51 (2001) 413–450. [doi:10.1146/annurev.nucl.](https://doi.org/10.1146/annurev.nucl.51.101701.132327)
2441 [51.101701.132327](https://doi.org/10.1146/annurev.nucl.51.101701.132327).
- 2442 [6] H. Areti, et al., CEBAF at 12 GeV, in preparation for submission to *Phys.*
2443 *Rev. AB* (2020).
- 2444 [7] U. Timm, Coherent Bremsstrahlung of Electrons in Crystals, *Fortschritt*
2445 *der Physik* 17 (1969) 765–808. [doi:10.1002/prop.19690171202](https://doi.org/10.1002/prop.19690171202).
- 2446 [8] K. Livingston, The Stonehenge technique. A method for aligning co-
2447 herent bremsstrahlung radiators, *Nucl. Instrum. Meth. A* 603 (3)
2448 (2009) 205 – 213. Available from: [http://www.sciencedirect.com/](http://www.sciencedirect.com/science/article/pii/S0168900209003477)
2449 [science/article/pii/S0168900209003477](http://www.sciencedirect.com/science/article/pii/S0168900209003477), [doi:https://doi.org/10.](https://doi.org/10.1016/j.nima.2009.02.010)
2450 [1016/j.nima.2009.02.010](https://doi.org/10.1016/j.nima.2009.02.010).
- 2451 [9] C. Meyer, A review of asymmetry measurements in vec-
2452 tor meson photoproduction experiments, *Tech. Rep.* 3076,
2453 Carnegie Mellon University, [https://halldweb.jlab.org/doc-](https://halldweb.jlab.org/doc-private/DocDB/ShowDocument?docid=3076)
2454 [private/DocDB/ShowDocument?docid=3076](https://halldweb.jlab.org/doc-private/DocDB/ShowDocument?docid=3076) (August 2016).
- 2455 [10] H. Bilokon, et al., Coherent bremsstrahlung in crystals as a tool for
2456 producing high energy photon beams to be used in photoproduction
2457 experiments at CERN SPS, *Nucl. Instrum. Meth.* 204 (1983) 299–310.
2458 Available from: [https://www.sciencedirect.com/science/article/](https://www.sciencedirect.com/science/article/pii/0167508783900613)
2459 [pii/0167508783900613](https://www.sciencedirect.com/science/article/pii/0167508783900613), [doi:10.1016/0167-5087\(83\)90061-3](https://doi.org/10.1016/0167-5087(83)90061-3).
- 2460 [11] G. Yang, et al., Rocking curve imaging for diamond radiator crys-
2461 tal selection, *Diamond and Related Materials* 19 (7) (2010) 719 –
2462 722, proceedings of Diamond 2009, The 20th European Conference
2463 on Diamond, Diamond-Like Materials, Carbon Nanotubes and Ni-
2464 trides, Part 2. Available from: [http://www.sciencedirect.com/](http://www.sciencedirect.com/science/article/pii/S0925963510000063)
2465 [science/article/pii/S0925963510000063](http://www.sciencedirect.com/science/article/pii/S0925963510000063), [doi:https://doi.org/10.](https://doi.org/10.1016/j.diamond.2009.12.017)
2466 [1016/j.diamond.2009.12.017](https://doi.org/10.1016/j.diamond.2009.12.017).

- 2467 [12] G. Yang, et al., High resolution X-ray diffraction study of single crystal
2468 diamond radiators, *physica status solidi (a)* 209 (9) (2012) 1786–1791.
2469 Available from: <https://onlinelibrary.wiley.com/doi/abs/10.1002/pssa.201200017>, doi:10.1002/pssa.201200017.
2470
- 2471 [13] J. Borggreen, B. Elbek, L. P. Nielsen, A proposed spectro-
2472 graph for heavy particles, *Nuclear Instruments and Methods* 24
2473 (1963) 1 – 12. Available from: <http://www.sciencedirect.com/science/article/pii/0029554X63902763>, doi:[https://doi.org/10.1016/0029-554X\(63\)90276-3](https://doi.org/10.1016/0029-554X(63)90276-3).
2474
2475
- 2476 [14] D. Sober, et al., The bremsstrahlung tagged photon beam in Hall
2477 B at JLab, *Nucl. Instrum. and Meth. A* 440 (2) (2000) 263
2478 – 284. Available from: <http://www.sciencedirect.com/science/article/pii/S0168900299007846>, doi:[http://dx.doi.org/10.1016/S0168-9002\(99\)00784-6](http://dx.doi.org/10.1016/S0168-9002(99)00784-6).
2479
2480
- 2481 [15] G. L. Yang, A summary of the optics design for the
2482 GLUEX single dipole tagger spectrometer, Tech. Rep. GlueX-
2483 doc-1186, Glasgow University, [https://halldweb.jlab.org/doc-](https://halldweb.jlab.org/doc-public/DocDB/ShowDocument?docid=1186)
2484 [public/DocDB/ShowDocument?docid=1186](https://halldweb.jlab.org/doc-public/DocDB/ShowDocument?docid=1186) (January 2009).
- 2485 [16] A. Somov, Resolution studies of a dipole tagger mag-
2486 net: response to the magnet review referees, Tech. Rep.
2487 GlueX-doc-1368, Jefferson Lab, [https://halldweb.jlab.org/doc-](https://halldweb.jlab.org/doc-public/DocDB/ShowDocument?docid=1368)
2488 [public/DocDB/ShowDocument?docid=1368](https://halldweb.jlab.org/doc-public/DocDB/ShowDocument?docid=1368) (January 2010).
- 2489 [17] D. I. Sober, Analysis of the Hall D Tagger Dipole
2490 Magnet Field Maps, Tech. Rep. GlueX-doc-4271, The
2491 Catholic University of America, [https://halldweb.jlab.org/doc-](https://halldweb.jlab.org/doc-private/DocDB/ShowDocument?docid=4271)
2492 [private/DocDB/ShowDocument?docid=4271](https://halldweb.jlab.org/doc-private/DocDB/ShowDocument?docid=4271) (July 2015).
- 2493 [18] H. Fischer, et al., Implementation of the dead time free F1 TDC in the
2494 COMPASS detector readout, *Nucl. Instrum. Meth. A* 461 (2001) 507–510.
2495 [arXiv:hep-ex/0010065](https://arxiv.org/abs/hep-ex/0010065), doi:10.1016/S0168-9002(00)01285-7.
- 2496 [19] V. Popov, et al., Performance studies of Hamamatsu R9800 photomultiplier
2497 tube with a new active base designed for use in the Hall D Broadband
2498 tagger Hodoscope, in: 2014 IEEE Nuclear Science Symposium and Medical
2499 Imaging Conference (NSS/MIC), Seattle, WA, 2014, pp. 1–4. doi:10.
2500 1109/NSSMIC.2014.7431075.
- 2501 [20] J. Hubbell, S. Seltzer, Tables of X-Ray Mass Attenuation Coefficients and
2502 Mass Energy-Absorption Coefficients from 1 keV to 20 MeV for Elements
2503 Z=1 to 92 and 48 Additional Substances of Dosimetric Interest, Tech. rep.,
2504 Radiation Physics Division, Physical Measurement Laboratory, National
2505 Institute of Standards and Technology, NIST Standard Reference Database
2506 126 (hyperlink) (2009).

- 2507 [21] G. Miller, D. R. Walz, A Tungsten Pin Cushion Photon Beam Moni-
2508 tor, Nucl. Instrum. Meth. 117 (1974) 33. doi:10.1016/0029-554X(74)
2509 90380-2.
- 2510 [22] M. Dugger, et al., Design and construction of a high-energy photon
2511 polarimeter, Nucl. Instrum. Meth. A867 (2017) 115 – 127. Avail-
2512 able from: [http://www.sciencedirect.com/science/article/pii/
2513 S0168900217305715](http://www.sciencedirect.com/science/article/pii/S0168900217305715), doi:10.1016/j.nima.2017.05.026.
- 2514 [23] F. Barbosa, et al., Pair spectrometer hodoscope for Hall D at Jef-
2515 ferson Lab, Nucl. Instrum. Meth. A 795 (2015) 376 – 380. Avail-
2516 able from: [http://www.sciencedirect.com/science/article/pii/
2517 S0168900215007573](http://www.sciencedirect.com/science/article/pii/S0168900215007573), doi:https://doi.org/10.1016/j.nima.2015.06.
2518 012.
- 2519 [24] F. Barbosa, et al., Time characteristics of detectors based on silicon pho-
2520 tomultipliers for the GlueX experiment, Instrum. Exp. Tech. 60 (2017)
2521 322–329. doi:10.1134/S0020441217030022.
- 2522 [25] A. Somov, others., The silicon photomultipliers in the detector subsystems
2523 of the GlueX experiment, J. Phys. Conf. Ser. 798 (2017) 012223. doi:
2524 10.1088/1742-6596/798/1/012223.
- 2525 [26] I. A. Tolstukhin, et al., Recording of relativistic particles in thin scin-
2526 tillators, Instrum. Exp. Tech. 57 (6) (2014) 658–661. doi:10.1134/
2527 S0020441214060153.
- 2528 [27] A. Somov, et al., Commissioning of the Pair Spectrometer of the GlueX
2529 experiment, J. Phys. Conf. Ser. 798 (2017). doi:10.1088/1742-6596/798/
2530 1/012175.
- 2531 [28] A. Somov, et al., Performance of the pair spectrometer of the GlueX experi-
2532 ment, J. Phys. Conf. Ser. 675 (4) (2016) 042022. doi:10.1088/1742-6596/
2533 675/4/042022.
- 2534 [29] A. Somov, Pair Spectrometer acceptance determination (Spring 2019),
2535 Tech. rep., Jefferson Lab, Technical Report GlueX-doc-3924 (hyperlink)
2536 (Feb. 2019).
- 2537 [30] D. Sober, Calibration of the Tagged Photon Beam: Normalization Meth-
2538 ods, Shower Counter and Pair Spectrometer, Tech. rep., Catholic University
2539 of America, Technical Report CLAS-NOTE-92-014 (hyperlink) (1992).
- 2540 [31] A. Eppich, R. Sealock, Studies of a Lead Glass Total Absorption Counter,
2541 Tech. rep., Jefferson Lab, Technical Report CLAS-NOTE-93-011 (hyper-
2542 link) (1993).
- 2543 [32] E. Anciant, et al., Photon Flux Normalization for CLAS, Tech. rep., CEA-
2544 Saclay, Technical Report CLAS-NOTE-1999-002 (hyperlink) (1992).

- 2545 [33] J. S. Alcorn, H. Peterson, S. S. Lorant, SLAC two-meter diameter, 25-
2546 kilogauss, superconducting solenoid, UAMH BINN, in: Applied Supercon-
2547 ductivity Conference, Inst. of Electrical and Electronics Engineers, Inc.,
2548 New York; Stanford Univ., CA, 1972, p. 273.
- 2549 [34] D. Aston, et al., The LASS spectrometer, Tech. Rep. SLAC-298,
2550 SLAC, Stanford, CA, Technical report SLAC-R-298 (1987). Avail-
2551 able from: <https://www-public.slac.stanford.edu/scidoc/docMeta.aspx?slacPubNumber=slac-R-298>.
2552
- 2553 [35] J. Ballard, et al., Refurbishment and testing of the 1970's era LASS solenoid
2554 coils for Jlab's Hall D, AIP Conf. Proc. 1434 (2012) 861–868. doi:10.1063/
2555 1.4707001.
- 2556 [36] J. Ballard, et al., Commissioning and Testing the 1970's Era LASS Solenoid
2557 Magnet in JLab's Hall D, IEEE Trans. Appl. Supercond. 25 (3) (2015)
2558 4500805. doi:10.1109/TASC.2014.2385152.
- 2559 [37] N. Laverdure, et al., The Hall D solenoid helium refrigeration system at
2560 JLab, AIP Conf. Proc. 1573 (1) (2014) 329–336. doi:10.1063/1.4860719.
- 2561 [38] H. Hakobyan, et al., A double-target system for precision measurements of
2562 nuclear medium effects, Nucl. Instrum. Meth. A: 592 (3) (2008) 218 – 223.
2563 doi:<https://doi.org/10.1016/j.nima.2008.04.055>.
- 2564 [39] Y. V. Haarlem, et al., The GlueX Central Drift Chamber: Design and
2565 Performance, Nucl. Instrum. Meth. A622 (2010) 142–156. doi:10.1016/
2566 j.nima.2010.06.272.
- 2567 [40] N. S. Jarvis, et al., The Central Drift Chamber for GLUEX, Nucl. In-
2568 strument. Meth. A962 (2020) 163727. doi:<https://doi.org/10.1016/j.nima.2020.163727>.
- 2570 [41] J. A. Kadyk, Wire chamber aging, Nucl. Instrum. Meth. 300 (3) (1991) 436
2571 – 479. doi:10.1016/0168-9002(91)90381-Y.
- 2572 [42] J. Va'vra, Physics and chemistry of aging - early developments, Nucl. In-
2573 strument. Meth. A515 (2003) 1 – 14, proceedings of the International Work-
2574 shop on Aging Phenomena in Gaseous Detectors. doi:<https://doi.org/10.1016/j.nima.2003.08.124>.
2575
- 2576 [43] F. Barbosa, Electronics overview, Tech. rep., Jefferson Lab, Technical Re-
2577 port GlueX-doc-2515 (hyperlink) (Jun. 2014).
- 2578 [44] L. Pentchev, et al., Studies with cathode drift chambers for the GlueX
2579 experiment at Jefferson Lab, Nucl. Instrum. Meth. A845 (2017) 281–284.
2580 doi:10.1016/j.nima.2016.04.076.

- 2581 [45] G. Visser, High Density 125 MSPS Differential Input ADC Module Spec-
 2582 ifications for GlueX Drift Chamber Application (2008). Available
 2583 from: https://halldweb.jlab.org/DocDB/0008/000855/002/Drifts_
 2584 [ADC_Specification_Document.pdf](https://halldweb.jlab.org/DocDB/0008/000855/002/Drifts_ADC_Specification_Document.pdf).
- 2585 [46] G. Visser, et al., A 72 channel 125 MSPS analog-to-digital converter
 2586 module for drift chamber readout for the GlueX detector, in: IEEE Nu-
 2587 clear Science Symposium Medical Imaging Conference, 2010, pp. 777–781.
 2588 doi:10.1109/NSSMIC.2010.5873864.
- 2589 [47] F. Barbosa, et al., The Jefferson Lab High Resolution Time-to-Digital Con-
 2590 verter (TDC), Tech. rep., Jefferson Lab, Technical Report GlueX-doc-1021
 2591 (hyperlink) (Apr. 2008).
- 2592 [48] V. Blobel, Millipede II (2007). Available from: [https://www.desy.de/](https://www.desy.de/~kleinwrt/MP2/doc/html/index.html)
 2593 [~kleinwrt/MP2/doc/html/index.html](https://www.desy.de/~kleinwrt/MP2/doc/html/index.html).
- 2594 [49] M. Staib, Calibrations for charged particle tracking and the measurements
 2595 of ω photoproduction with the GlueX Detector, Ph.D. thesis, Carnegie
 2596 Mellon University, Department of Physics, Technical Report GlueX-doc-
 2597 3393 (hyperlink) (September 2017).
- 2598 [50] R. E. Kalman, A New Approach to Linear Filtering and Prediction Prob-
 2599 lems, ASME Journal of Basic Engineering 82 (1) (1960) 35–45. doi:
 2600 10.1115/1.3662552.
- 2601 [51] R. E. Kalman, R. S. Bucy, New Results in Linear Filtering and Prediction
 2602 Theory, ASME Journal of Basic Engineering 83 (1) (1961) 95–108. doi:
 2603 10.1115/1.3658902.
- 2604 [52] T. Beattie, et al., Construction and performance of the barrel electromag-
 2605 netic calorimeter for the GLUEX experiment, Nucl. Instrum. Meth. A896
 2606 (2018) 24 – 42. doi:10.1016/j.nima.2018.04.006.
- 2607 [53] E. Smith, Development of Silicon Photomultipliers and their Applications
 2608 to GlueX, Tech. rep., Jefferson Lab, AIP Proceedings 1753 – XI Latin
 2609 American Symposium on Nuclear Physics and Applications, Medellín,
 2610 Colombia. Technical Report GlueX-doc-2913 (hyperlink) (Dec. 2015).
- 2611 [54] F. Barbosa, et al., Silicon photomultiplier characterization for the GlueX
 2612 barrel calorimeter, Nucl. Instrum. Meth. A695 (2012) 100 – 104. doi:
 2613 10.1016/j.nima.2011.11.059.
- 2614 [55] Y. Qiang, et al., Radiation hardness tests of SiPMs for the JLab Hall D
 2615 Barrel calorimeter, Nucl. Instrum. Meth. A698 (2013) 234 – 241. doi:
 2616 10.1016/j.nima.2012.10.015.
- 2617 [56] O. Soto, et al., Characterization of novel Hamamatsu Multi Pixel Photon
 2618 Counter (MPPC) arrays for the GlueX experiment, Nucl. Instrum. Meth.
 2619 A732 (2013) 431–436. doi:10.1016/j.nima.2013.06.071.

- 2620 [57] O. Soto, et al., Novel Hamamatsu Multi-Pixel Photon Counter (MPPC) ar-
 2621 ray studies for the GlueX experiment: New results, Nucl. Instrum. Methods
 2622 A 739 (2014) 89–97. doi:10.1016/j.nima.2013.12.032.
- 2623 [58] T. Beattie, et al., Methodology for the Determination of the Photon Detec-
 2624 tion Efficiency of Large-Area Multi-Pixel Photon Counters, IEEE Trans-
 2625 actions on Nuclear Science 62 (2015) 1865–1872. doi:10.1109/TNS.2015.
 2626 2442262.
- 2627 [59] E. Smith, Development of Silicon Photomultipliers and their Applications
 2628 to GlueX Calorimetry, AIP Conference Proceedings 1753 (1) (2016) 010001.
 2629 doi:10.1063/1.4955340.
- 2630 [60] R. Crittenden, et al., A 3000 element lead-glass electromagnetic calorimeter,
 2631 Nucl. Instrum. Meth. A387 (3) (1997) 377 – 394. doi:10.1016/
 2632 S0168-9002(97)00101-0.
- 2633 [61] R. Jones, et al., Performance of the RadPhi detector and trigger in a high
 2634 rate tagged photon beam, Nucl. Instrum. Meth. A570 (3) (2007) 384 – 398.
 2635 doi:10.1016/j.nima.2006.09.039.
- 2636 [62] A. Brunner, et al., A Cockcroft-Walton base for the FEU84-3 photomul-
 2637 tiplier tube, Nucl. Instrum. Meth. A414 (1998) 466–476. doi:10.1016/
 2638 S0168-9002(98)00651-2.
- 2639 [63] Wikipedia contributors, CAN bus — Wikipedia, the free encyclopedia,
 2640 [Online; accessed 28-October-2019] (2019). Available from: [https://en.
 2641 wikipedia.org/w/index.php?title=CAN_bus&oldid=922757529](https://en.wikipedia.org/w/index.php?title=CAN_bus&oldid=922757529).
- 2642 [64] K. Moriya, et al., A measurement of the energy and timing resolution of
 2643 the GlueX Forward Calorimeter using an electron beam, Nucl. Instrum.
 2644 Meth. 726 (2013) 60 – 66. doi:10.1016/j.nima.2013.05.109.
- 2645 [65] F. Barbosa, et al., A VME64x, 16-Channel, Pipelined 250 MSPS Flash
 2646 ADC With Switched Serial (VXS) Extension, Tech. rep., Jefferson Lab,
 2647 Technical Report GlueX-doc-1022 (hyperlink) (Apr. 2007).
- 2648 [66] M. Dugger, et al., Hall D / GlueX Technical Construction Report, Chapter
 2649 3.10, Tech. rep., Jefferson Lab, Technical Report GlueX-doc-2511 (hyper-
 2650 link) (Jul. 2017).
- 2651 [67] J. V. Bennett, et al., Precision timing measurement of phototube pulses
 2652 using a flash analog-to-digital converter, Nucl. Instrum. Meth. A622 (2010)
 2653 225–230. doi:10.1016/j.nima.2010.06.216.
- 2654 [68] E. Anassontzis, et al., Relative gain monitoring of the GLUEX calorimeters,
 2655 Nucl. Instrum. Meth. A738 (2014) 41 – 49. doi:10.1016/j.nima.2013.
 2656 11.054.

- 2657 [69] B. D. Schaefer, et al., Radiation Damage of F8 Lead Glass with 20 MeV
2658 Electrons, Nucl. Instrum. Meth. B274 (2012) 111–114. doi:10.1016/j.
2659 nimb.2011.12.005.
- 2660 [70] R. T. Jones, et al., A bootstrap method for gain calibration and resolu-
2661 tion determination of a lead-glass calorimeter, Nucl. Instrum. Meth. A566
2662 (2006) 366–374. doi:10.1016/j.nima.2006.07.061.
- 2663 [71] H. A. Ghoul, et al., Measurement of the beam asymmetry Σ for π^0 and η
2664 photoproduction on the proton at $E_\gamma = 9$ GeV, Phys. Rev. C95 (4) (2017)
2665 042201(R). doi:10.1103/PhysRevC.95.042201.
- 2666 [72] S. Adhikari, et al., Beam Asymmetry Σ for the Photoproduction of η and
2667 η' Mesons at $E_\gamma = 8.8$ GeV, Phys. Rev. C100 (5) (2019) 052201(R). doi:
2668 10.1103/PhysRevC.100.052201.
- 2669 [73] A. Ali, et al., First Measurement of Near-Threshold J/ Exclusive Pho-
2670 toproduction off the Proton, Phys. Rev. Lett. 123 (7) (2019) 072001.
2671 doi:10.1103/PhysRevLett.123.072001.
- 2672 [74] E. Pooser, et al., The GlueX Start Counter Detector, Nucl. Instrum. Meth.
2673 A927 (2019) 330–342. doi:10.1016/j.nima.2019.02.029.
- 2674 [75] H. Dong, et al., Integrated tests of a high speed VXS switch card and 250
2675 MSPS flash ADCs, in: 2007 IEEE Nuclear Science Symposium Conference
2676 Record, Vol. 1, 2007, pp. 831–833. doi:10.1109/NSSMIC.2007.4436457.
- 2677 [76] A. Somov, Level-1 Trigger of the GlueX Experiment, Tech. rep., Jefferson
2678 Lab, Technical Report GlueX-doc-1137 (hyperlink) (Jul. 2008).
- 2679 [77] A. Somov, Update on the trigger simulation, Tech. rep., Jefferson Lab,
2680 Technical Report GlueX-doc-1272 (hyperlink) (Jul. 2009).
- 2681 [78] A. Somov, Development of level-1 triggers for experiments at Jefferson Lab,
2682 AIP Conf. Proc. 1560 (1) (2013) 700–702. doi:10.1063/1.4826876.
- 2683 [79] S. Boyarinov and others, The CLAS12 Data Acquisition System, Nucl. In-
2684 strum. Meth. In press (2020). doi:10.1016/j.nima.2020.163698.
- 2685 [80] C. Slominski, et al., A MySQL based EPICS archiver, Proceedings,
2686 ICALEPCS2009 (2010) 447–449 Available from: <http://accelconf.web.cern.ch/AccelConf/icalleps2009/papers/wep021.pdf>.
- 2687
- 2688 [81] X. Chen, K. Kasemir, BOY, a modern graphical operator interface edi-
2689 tor and runtime, Proceedings, ICALEPCS2011 (2011) 1404–1406 Available
2690 from: <http://accelconf.web.cern.ch/AccelConf/PAC2011/papers/weobn3.pdf>.
- 2691
- 2692 [82] K. Kasemir, et al., The Best Ever Alarm System Toolkit, Proceedings,
2693 ICALEPCS2009 (2010) 1062–1065 Available from: <http://accelconf.web.cern.ch/AccelConf/icaleps2009/papers/tua001.pdf>.
- 2694

- 2695 [83] D. Lawrence and others, RootSpy Data Quality Monitoring System. Avail-
2696 able from: <https://www.jlab.org/RootSpy/>.
- 2697 [84] JLab Data Acquisition Group, CODA, coda.jlab.org. Available from:
2698 <https://coda.jlab.org>.
- 2699 [85] R. Brun, F. Rademakers, ROOT: An object oriented data analy-
2700 sis framework, Nucl. Instrum. Meth. A389 (1997) 81–86, See also
2701 <http://root.cern.ch/>. doi:10.1016/S0168-9002(97)00048-X.
- 2702 [86] M. Ito, D. Lawrence, GlueX Computing Model for RunPeriod-2017-01,
2703 Tech. rep., Jefferson Lab, Technical Report GlueX-doc-3821 (hyperlink)
2704 (Jun. 2018).
- 2705 [87] JLab Data Acquisition Group, CODA Online Data Formats,
2706 <https://coda.jlab.org/drupal/system/files/eventbuilding.pdf>.
- 2707 [88] R. Brun, F. Bruyant, M. Maire, A. C. McPherson, P. Zancarini, GEANT3
2708 (1987).
- 2709 [89] S. Agostinelli, et al., GEANT4: A Simulation toolkit, Nucl. Instrum. Meth.
2710 A506 (2003) 250–303. doi:10.1016/S0168-9002(03)01368-8.
- 2711 [90] J. Allison, et al., Recent developments in Geant4, Nucl. Instrum. Meth.
2712 A835 (2016) 186–225. doi:10.1016/j.nima.2016.06.125.
- 2713 [91] R. Jones, HDDS Schema. Available from: [https://halldsvn.jlab.org/
2714 repos/trunk/hdds/HDDS-1_1.xsd](https://halldsvn.jlab.org/repos/trunk/hdds/HDDS-1_1.xsd).
- 2715 [92] R. Jones, Detector Models for GlueX Monte Carlo Simulation: the CD2
2716 Baseline, Tech. rep., University of Connecticut, Technical Report GlueX-
2717 doc-732 (hyperlink) (Jan. 2007).
- 2718 [93] R. Jones, HDDM – Hall D Data Model, Tech. rep., University of Connecti-
2719 cut, Technical Report GlueX-doc-65 (hyperlink) (Sep. 2003).
- 2720 [94] T. Sjostrand, S. Mrenna, P. Z. Skands, PYTHIA 6.4 Physics and Manual,
2721 JHEP 05 (2006) 026. doi:10.1088/1126-6708/2006/05/026.
- 2722 [95] B. Aubert, et al., The BaBar detector, Nucl. Instrum. Meth. A479 (2002)
2723 1–116. doi:10.1016/S0168-9002(01)02012-5.